UNIVERSITÄTSKLINIKUM HAMBURG-EPPENDORF

Institut für Experimentelle Pharmakologie und Toxikologie

Direktor: Prof. Dr. Thomas Eschenhagen

Disease modelling and molecular therapy of severe cardiomyopathy in hiPSC-derived cardiomyocytes carrying bi-allelic truncating *MYBPC3* mutations

Dissertation

zur Erlangung des Grades eines Doktors der Medizin
an der Medizinischen Fakultät der Universität Hamburg.

vorgelegt von:

Nele Annika Warnecke
aus Hamburg

Hamburg 2021

Angenommen von der
Medizinischen Fakultät der Universität Hamburg am: 22.12.2021

Veröffentlicht mit Genehmigung der
Medizinischen Fakultät der Universität Hamburg.

Prüfungsausschuss, der/die Vorsitzende: Prof. Dr. Monica Patten-Hamel

Prüfungsausschuss, zweite/r Gutachter/in: Prof. Dr. Lucie Carrier

Drittgutachter: Prof. Dr. Norbert Frey

Table of Contents

1 Introduction

Cardiovascular diseases are one of the main reasons for mortality in industrial countries. In 2017, 37% of deaths in Germany were due to failure of the cardiovascular system, which reflects the major cause of deaths and accounts for most of the costs in the German health system (Federal Statistical Office Germany, *https://www.destatis.de/DE/Home/_inhalt.html accessed August 2019*). To gain insights into the pathogenesis and pathophysiology of cardiac diseases in 1948 the Framingham Heart Study was started followed by many other studies (Mahmood et al., 2014). To date, ~70 years later, the mechanisms of the diseases are still not well understood and further investigations have to be performed in order to overcome this main actor of mortality in the Western civilisation.

1.1 Cardiomyopathies

Cardiomyopathies are cardiac diseases leading to heart failure at final stage, if not treated properly (Tardiff et al., 2015). The term “cardiomyopathies” mainly refers to the group of nonischemic cardiomyopathies, excluding the ischemic forms as a consequence of coronary artery disease. The group of nonischemic cardiomyopathies can be further divided into four subgroups classifying hypertrophic cardiomyopathy (HCM), dilated cardiomyopathy (DCM), restrictive cardiomyopathy (RCM) and arrhythmogenic right ventricular cardiomyopathy (ARVC). In children, most important cardiomyopathy phenotypes are DCM, HCM, RCM and left ventricular noncompaction (Braunwald, 2017), which display distinct morphologic charcateristics (Figure 1).

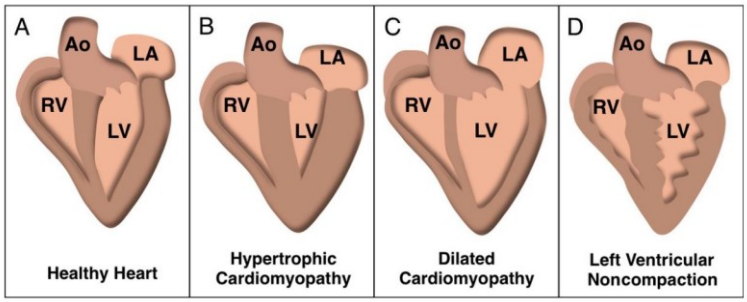

Figure 1: Morphologic characteristics of nonischemic cardiomyopathies
Depicted is a healthy heart (A) in contrast to hearts with hypertrophic (B) or dilated (C) cardiomyopathy as well as left ventricular noncompaction (D) with the typical structural characteristics. Ao: aorta; LA: left atrium; LV: left ventricle; RV: right ventricle. Figure adapted from Harvey and Leinwand (2011).

HCM is the most common cardiac monogenetic disease with an estimated prevalence of 1:200 in the population (Semsarian et al., 2015). It is inherited in an autosomal-dominant Mendelian trait (Richard et al., 2003). The disease presents with a typical clinical phenotype,

meaning thickening of the left ventricular wall, particularly the septum, nondilated left ventricle, diastolic dysfunction and sudden cardiac death among the young. Importantly, diagnosis of HCM excludes the presence of another cardiac or systemic disease leading to subsequent left ventricular hypertrophy, e.g. aortic stenosis or arterial hypertension (Burke et al., 2016; Maron, 2002). Today, most therapies of HCM are based on symptom relief and do not target the underlying mechanism (Tardiff et al., 2015).

DCM, RCM and ARVC are different with regards to the pathogenesis as well as the clinical phenotype. Especially DCM is known for its large heterogeneity of risk factors, meaning the onset of the diseases can only to a minor part be referred to genetic reasons and mostly referred to other causes, e.g. infection or alcohol abuse (Braunwald, 2017). Since the present work focuses on *MYBPC3* mutations typically causing HCM, the other cardiomyopathies are not further described in detail.

1.1.1 Cardiac myosin-binding protein C (cMyBP-C)

Over two-third of identified HCM-causing mutations are located in the *MYBPC3* gene and *MYH7*, whereas mutations in *TNNT2*, *TNNI3*, *TPM1*, *MYL2*, *MYL3* and *ACTC1* are found less frequently (Sabater-Molina et al., 2018). About 365 different mutations have been found in the *MYBPC3* gene, accounting for more than 40% of all HCM mutations and making it the most commonly affected gene (Carrier, 2020).

MYBPC3 is located on chromosome 11 and contains 35 exons, of which 34 exons are coding for the cardiac myosin-binding protein C (cMyBP-C) (Carrier et al., 1997). MyBP-C are a family of three related genes encoding fast-skeletal, slow-skeletal and cardiac isoforms. The cardiac isoform (150 kDa) is exclusively expressed in the heart (Schlossarek et al., 2011). It is a component of the thick filament and is located in the C-zones of the A-band in the sarcomere, forming typical doublets at both sites of the M-line (Figure 2).

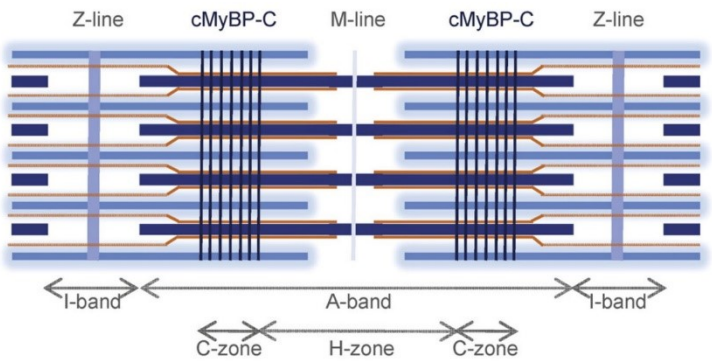

Figure 2: Sarcomeric localisation of cMyBP-C
cMyBP-C: dark blue; thin filament: light blue; thick filament: middle blue; titin: orange. Figure adapted from Carrier et al. (2015).

It is known that cMyBP-C plays a role in the structure and the function of the sarcomere (Carrier et al., 2015; Schlossarek et al., 2011). The structure of the protein consists of eight immunoglobulin-like and three fibronectin-like domains. Besides, the cardiac specific motif region contains important phosphorylation sites. cMyBP-C interacts with myosin and actin via different domains at the N-terminal domain, and with titin via the C-terminal domains (Schlossarek et al., 2011). Functionally, it regulates cross-bridge cycling due to its interaction with the thin and thick filaments, as known from mice. In the knock-out state, cross-bridge cycling is facilitated as the myosin heads are brought closer to actin. Hence, the function of cMyBP-C may be described as a brake in the cross-bridge formation process. The phosphorylation state of few Ser residues in the motif region plays a determinant role in directing cMyBP-C to interact with the other filaments and determines, which is predominantly favoured (Carrier et al., 2015). Phosphorylation occurs upon β-adrenergic stimulation by the cAMP-dependent protein kinase. Moreover, cMyBP-C is also reported to influence calcium (Ca^{2+}) handling, since higher sensitivity towards external Ca^{2+} was observed in the absence of cMyBP-C (Carrier et al., 2015; Schlossarek et al., 2011). These data suggest that cMyBP-C is crucial for the regulation of normal cardiac function and that it is serving towards protection of the heart, in particular when taking into account its role in disease development of HCM (Schlossarek et al., 2011).

In *MYBPC3*, the majority (>75%) of pathogenic mutations found in HCM patients are frameshift or nonsense mutations leading to a premature termination codon (PTC) in the respective mRNA (Carrier, 2020; Helms et al., 2014) and resulting in C-terminal truncated cMyBP-C lacking important interaction binding-sites (Behrens-Gawlik et al., 2014). In fact, truncated cMyBP-C were not detectable, neither in mice nor in human tissues (Carrier et al., 2015; Helms et al., 2014; Vignier et al., 2009). A mechanism explaining this finding is the well-described mechanism of the nonsense-mediated mRNA decay (NMD) (Vignier et al., 2009). This safety control mechanism degrades mRNA containing a PTC >50 nucleotides upstream of the last intron. Together with the ubiquitin–proteasome system (UPS) and the autophagy-lysosomal pathway (ALP) it protects the cell from poisoning mutant peptides (Schlossarek et al., 2011). As truncated cMyBP-C is not detected, the total amount of cMyBP-C is reduced. Therefore, haploinsuffiency is regarded as the main disease mechanism in heterozygotes as the healthy allele is not able to compensate the mutated allele (Marston et al., 2012; Prondzynski et al., 2017), although this assumption is challenged by others (Helms et al., 2014).

1.1.2 Severe cardiomyopathies

Severe forms of cardiomyopathy, also referred to as neonatal or pediatric cardiomyopathy, evolve soon after birth and are often inherited (Braunwald, 2017; Carrier et al., 2015). Especially bi-allelic truncating *MYBPC3* mutations - homozygous or compound heterozygous - are reported to develop in a severe phenotype and can cause death of infants within the first year of life (Ortiz et al., 2009; Wessels et al., 2015). The neonates reported in the study of Wessels et al. (2015) suffer from feeding problems, dyspnea, hypotension and failure to thrive. Moreover, characteristics of DCM, left ventricular non-compaction (LVNC) and structural abnormalities, like septal defects, were found in these infants and lead to rapid evolvement of systolic dysfunction and death (Braunwald, 2017; Kolokotronis et al., 2019; Wessels et al., 2015).

The relevance of double-truncating mutations becomes clear when looking at countries with high prevalence of founder mutations. Here, the likelihood of inheriting two mutations, one from each parent, is dramatically increased (Carrier et al., 2015). The presence of more than one disease causing mutation found in pediatric cardiomyopathy suggests a gene dosage effect in HCM that is associated with earlier disease-onset and deteriorated outcome (Maron et al., 2012).

Since treatment options in sarcomeric cardiomyopathies mainly address symptom's relief, but do not aim at curative outcome, novel therapies are needed to target the disease at its substance (Tardiff et al., 2015). To date, the only disease curing treatment for these infants remains heart transplantation.

1.2 Human-induced pluripotent stem cells (hiPSCs) and disease modelling in the cardiovascular field

Human-induced pluripotent stem cells (hiPSCs) have overwhelmed the field of disease modelling approaches in the past years. Since knowledge from animal experiments, mostly conducted in mice, cannot fully been applied to humans (Eschenhagen and Carrier, 2019) and work with human embryonic stem cells (hESCs) leads to ethical debates, the need for an additional *in vitro* disease model system came up. It is obvious that further knowledge is necessarily required before translating the findings in clinical trials (Merkle and Eggan, 2013). In 2006, Takahashi and Yamanaka published their work showing that murine somatic cells can be reprogrammed into self-renewing induced pluripotent stem cells (iPSCs) with the use of solely four transcription factors, Oct-4, Sox2, c-Myc, and KLF4 (Takahashi and

Yamanaka, 2006). One year later, they showed that this method can also be applied to adult human dermal fibroblasts (Takahashi et al., 2007). Moreover, they proved that these iPSCs were able to differentiate into cell types of all three germ layers. For this revolutionary discovery, Yamanaka didn't only earn the Nobel prize in Physiology and Medicine together with John Gurdon in 2012, but also the appreciation of a whole field of research groups starting to work with this technology. The advantages of this technique are obvious since ethical debates as well as rare accessibility to human tissue were circumvented with this approach. Besides, it offers the opportunity of hypothetically unlimited access to human cells (Hockemeyer and Jaenisch, 2016; Merkle and Eggan, 2013).

Since then, elaborated protocols have been published in order to efficiently generate hiPSCs (Park et al., 2008) and optimisation has been performed due to use of non-integrating Sendai virus for reprogramming (Fusaki et al., 2009) or episomal vectors (Yu et al., 2009) amongst others. Successfully generated hiPSCs can be used for various subsequent applications (Figure 3), e.g. drug testing platforms, transplantation approaches as well as *in vitro* disease modelling (Hockemeyer and Jaenisch, 2016).

Figure 3: The technology of human-induced pluripotent stem cells
Reprogramming of patient's fibroblasts leads to hiPSCs, which can subsequently be differentiated into desired cell types of all three germ layers. These differentiated cells can be used for further applications, e.g. disease modelling or transplantation therapies. Figure adapted from Hockemeyer and Jaenisch (2016).

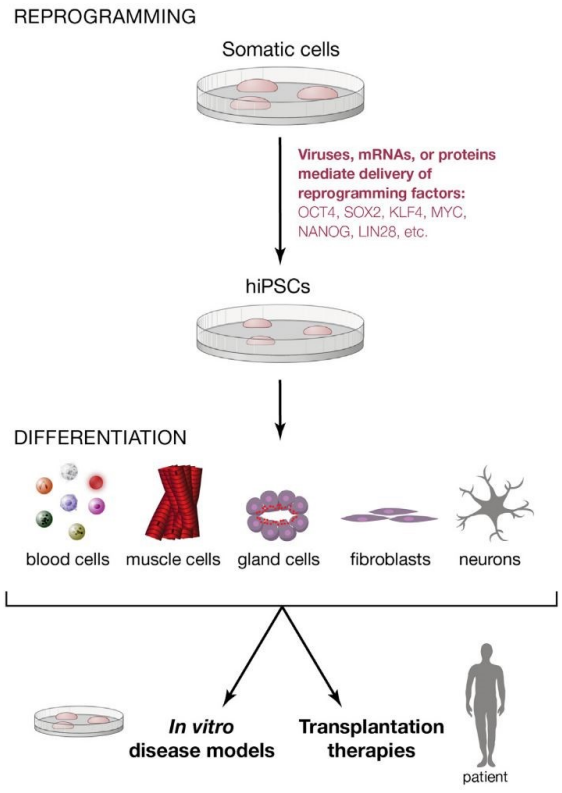

This technology also gained enormous interest in the cardiovascular research field (Brandao et al., 2017; Musunuru et al., 2018). To date, hiPSC-derived cardiomyocytes (hiPSC-CMs) are being validated to be used for cardiotoxicity studies (Khan et al., 2013), transplantation therapies after myocardial injury (Weinberger et al., 2016) and cardiovascular disease modelling. In terms of disease modelling, hiPSC-CMs have been successfully used to model genetic diseases such as long-QT syndrome (Lahti et al., 2012) and HCM (Prondzynski et al., 2017; Seeger et al., 2019), reflecting their typical characteristics. Moreover, Ma et al. (2018) were able to demonstrate the use of hiPSCs in combination with genome editing (CRISPR/Cas9) for precision medicine and risk

stratification evaluating the pathogenity of a variant of uncertain significance (VUS) in the *MYL3* gene.

Nonetheless, hiPSCs and hiPSC-derived cell types have some limitations. On the one hand, hiPSC cultivation is challenging since it requires several quality control measures in terms of pluripotency, screening for infection, e.g. mycoplasma, clearance of viral vectors used for reprogramming and genomic stability, e.g. karyotypic abnormalities (Musunuru et al., 2018). On the other hand, when successfully implemented in the lab, hiPSC differentiation into definite cell types like cardiomyocytes (CMs) may be challenging as well (cf. 1.4). This means that mixed cell populations could arise, which might impair comparability between cell lines and biological evidence, respectively (Eschenhagen et al., 2015). Furthermore, Kilpinen et al. (2017) emphasised on vast genetic and phenotypic variability they found in different hiPSC lines from healthy donors, which would limit their potential for research use. Additionally, one major limitation observed in CM culture derived from hiPSCs is their fetal-like phenotype, meaning that they are immature and show typical characteristics of embryonic cells in terms of gene expression patterns or morphological features (Bedada et al., 2016). This is not necessarily an issue, but it becomes if the disease has a late-onset. Several groups have therefore focused on methods how maturation can be driven in hiPSC-CMs. Long-term culture, cultivation in 3D tissue format, time point of tissue generation, co-culture with other cell types, electrical/mechanical stimulation or thyroid and glucocortical hormonal stimulation are only few factors improving maturation status (Devalla and Passier, 2018; Parikh et al., 2017; Ronaldson-Bouchard et al., 2018; Ruan et al., 2016; Ulmer et al., 2018).

Conclusively, hiPSCs offer a great opportunity to study monogenetic diseases such as HCM *in vitro*, especially due to the limited access to human diseased cardiac tissue, e.g. from HCM patients with outflow obstruction undergoing surgical myectomy. Here, hiPSCs provide a valuable tool to gain human cardiac cells with defined genetic background of the patient with the disease of interest (Eschenhagen et al., 2015). In terms of neonatal cardiomyopathy, access to cardiac tissue is even more limited and a disease model using hiPSC technology combined with genome editing opportunities (cf. 1.3) is required in order to study the disease phenotype *in vitro*.

1.3 Genome editing using the CRISPR/Cas9 system

Besides the generation of hiPSCs, another powerful tool has revolutionised science in the past decade, the clustered regularly interspaced short palindromic repeats (CRISPR)/Cas9 system. The story of the CRISPR/Cas9 system began, when it was discovered as a part of

the adaptive immune system in prokaryotes (Lander, 2016; Mojica et al., 2005). Whereas the function of these mysterious repeats was completely unknown, when Francisco Mojica first observed these in the genome of archaea (Lander, 2016; Mojica et al., 1995), knowledge has rapidly increased recently. Today it is known, that the CRISPR associated protein 9 (Cas9) is an endonuclease that is able to cleave DNA at specific target-sites guided by specific RNAs, the crRNA as well as the tracrRNA (Doudna and Charpentier, 2014). Doudna and Charpentier were able to show that the crRNA together with the tracrRNA can be combined to a single guide RNA (sgRNA) that has the potential to be used for genome editing (Jinek et al., 2012). This system facilitated genome editing to an enormous extent, especially in contrast to earlier developed techniques using zinc-finger nucleases (ZFNs) and transcription activator-like effector nucleases (TALENs), which were more laborious and included engineering of individual enzymes for each approach. One major advantage of CRISPR/Cas9 is that for each target sequence only the sgRNA has to be engineered, which makes it more simple and, in principle, possible to edit any locus in the genome (Sternberg and Doudna, 2015). In 2020, Doudna and Charpentier were honoured with the Nobel Prize in Chemistry for their discovery to use the CRISPR/Cas9 technology as a tool for genome editing.

The CRISPR/Cas system is classified into six different types according to the CRISPR protein that is used (Wright et al., 2016). Nowadays, the Cas9 nuclease extracted from *S. pyogenes* is mostly used (Figure 4). When guided by its RNA to a 20-nucleotide complementary target sequence in the DNA, the Cas9 enzyme recognises a 5'-NGG protospacer adjacent motif (PAM) that is located adjacent to the target sequence and induces a double-strand break (DSB) 3 bp upstream of the PAM (Ran et al., 2013).

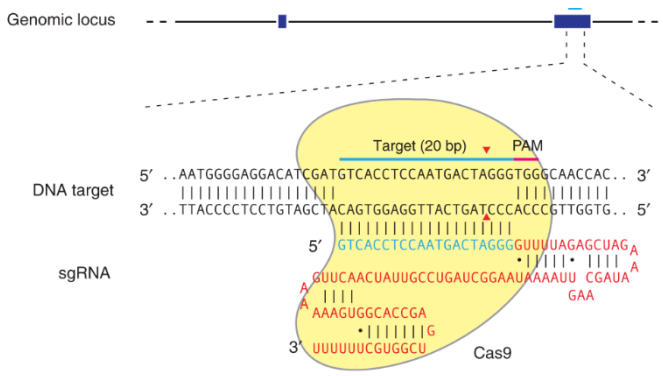

Figure 4: The CRISPR/Cas9 system in genome editing
Depicted are the Cas9 nuclease (yellow) together with its sgRNA (blue and red) at the 20 bp target sequence (blue) adjacent to its PAM (pink). The cleavage site is marked via red triangle. PAM: protospacer adjacent motif; sgRNA: single guide RNA. Figure adapted from Ran et al. (2013).

After DNA cleavage, the blunt-ended cutting site is usually repaired by intrinsic DNA repair mechanisms existing in the cell (Ran et al., 2013). There are mainly two pathways that occur

after DNA damage (Figure 5). One is the error-prone nonhomologous end joining (NHEJ) pathway that is preferentially used by the cell since it leads to rapid ligation of the two DNA fragments. In case of genome editing, it is especially used for knocking out a gene, because it leads to small insertions or deletions called indels that interrupt the reading frame and therefore lead to PTCs. The second is the homology-directed repair (HDR) pathway, which is more precise, but occurs to a much lower extent and is only active during S and G2 phase of the cell cycle. For directed genome editing, a specific template must be provided to the cell, either a repair template to create isogenic controls or a template carrying nucleotide exchange(s) in order to knock in specific mutations of interest. Single-stranded DNA oligonucleotides (ssODN) may serve as templates, either designed in sense or antisense direction, and may be symmetrically or asymmetrically homologous (Doudna and Charpentier, 2014; Ran et al., 2013; Sternberg and Doudna, 2015).

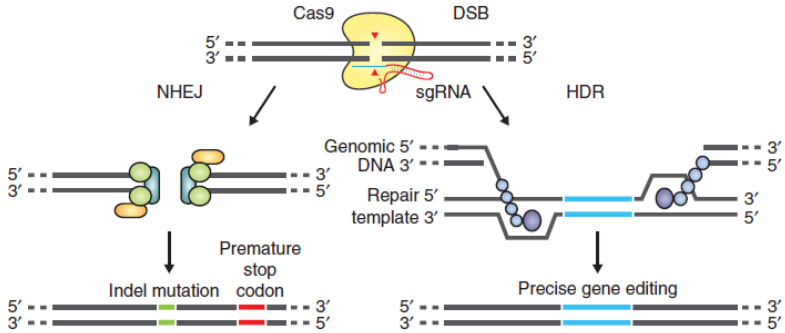

Figure 5: DNA repair mechanisms after Cas9 cleavage
Depicted are the error-prone NHEJ pathway as well as the high-fidelity HDR pathway for precise genome editing with the use of a provided template. DSB: double-strand break; HDR: homology-directed repair; NHEJ: nonhomologous end joining. Figure adapted from Ran et al. (2013).

Expression of Cas9 enzyme can be achieved by different methods, e.g. using lentivirus, plasmids, mRNA or via ribonucleoprotein (RNP) complex transfection (Sternberg and Doudna, 2015). More recently, the RNP-based approach rose more into the focus of researchers since it was shown to lead to higher editing efficiencies as well as reduced cell toxicity (Kim et al., 2014; Liang et al., 2015).

One major concern of the CRISPR/Cas9 technology is the occurrence of potential off-target effects that might occur in other highly homologous regions in the genome (Fu et al., 2013; Sternberg and Doudna, 2015; Zhang et al., 2015). Although the CRISPR/Cas9 toolbox has improved recently and several techniques aim to minimise off-target effects, this still remains one limitation when used for *in vivo* gene therapy purposes. Still, for *in vitro* genome editing, the use of RNP-based editing was reported to have several advantages over classical plasmid or viral Cas9 expression methods. Importantly, it was shown that off-target

activity was significantly reduced, which might be due to the fact that components were more transiently present in the cell (Jacobi et al., 2017; Kim et al., 2014; Liang et al., 2015).

In terms of HDR, Paquet et al. (2016) recently showed how introduction of zygosity is driven in relationship between distance from the DSB to the target site and how template design can be directed towards higher editing accuracy. For sgRNA design, several platforms may be used in order to *in silico* predict on-target specificity as well as off-target binding sites, e.g. from the Zhang Lab (MIT) or commercially from IDT®.

CRISPR/Cas9 gene editing became also attractive to the field of stem cells. When combined with the hiPSC technology, the CRISPR/Cas9 method provides the opportunity to implement disease modelling *in vitro* in a human context that circumvents the use of animal experiments as well as the limited access to human tissue. Furthermore, it opens the possibilitiy to engineer isogenic controls for specific disease-causing mutations and study its influence on disease phenotype under equal genetic backgrounds and therefore increases reliability of the observations (Hockemeyer and Jaenisch, 2016).

1.4 Cardiac differentiation of hiPSCs

In order to investigate a cardiac phenotype in the *in vitro* model, the hiPSCs have to be differentiated into CMs. Hence, several protocols have been developed in the last years (Eschenhagen et al., 2015; Rajala et al., 2011). The major strategies of cardiac differentiation *in vitro* is to mimic embryonic heart development *in utero* by using transcription factors and pathways known from cardiogenesis. First, undifferentiated stem cells are driven towards the mesodermal germ layer (Figure 6), where especially the wingless/INT proteins (WNT), the fibroblast growth factors (FGFs) and the transforming growth factor-β (TGF-β) superfamily with the bone morphogenetic protein 4 (BMP4), Nodal and activin A play a major role (Spater et al., 2014). Then, sequential activation and inhibition of the WNT signalling pathway is crucial for further specification to cardiac progenitors and finally CMs (Lian et al., 2012; Minami et al., 2012; Spater et al., 2014). Since its tight regulation *in vivo*, the exact tuning of directed cardiac differentiation and intervention on the signalling pathways *in vitro* is still not fully optimised and remains subject to further improvements of future differentiation protocols.

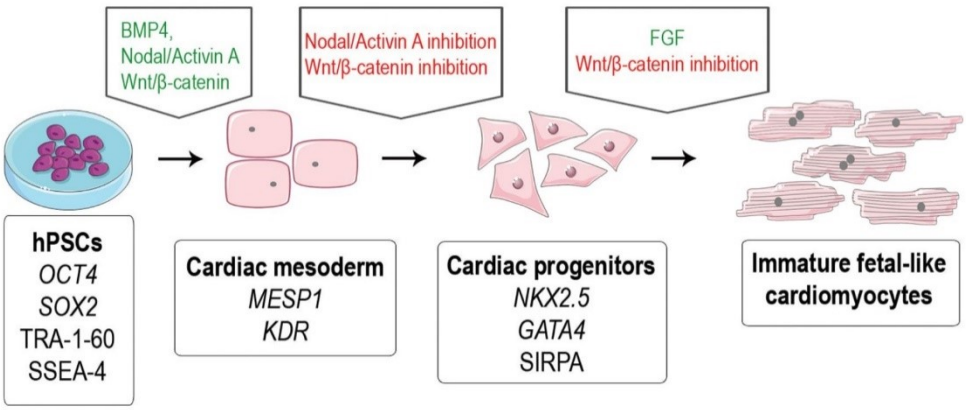

Figure 6: Cardiac differentiation of hiPSCs
Depicted are the different stages of cardiac mesoderm, cardiac progenitors and CMs with their respective typical transcription factors (cursive) or cell surface markers (normal text). Activation (green) or inhibition (red) of certain signalling pathways are involved in the differentiation process. Figure adapted from Ojala and Aalto-Setälä (2016), available from https://www.intechopen.com/books/pluripotent-stem-cells-from-the-bench-to-the-clinic/modeling-hypertrophic-cardiomyopathy-with-human-induced-pluripotent-stem-cells, accessed August 2019.

Today, researchers mainly use two different methods of cardiac differentiation, either aggregation-based in suspension culture (Breckwoldt et al., 2017; Burridge and Zambidis, 2013) or monolayer cultures with adherent cells (Mosqueira et al., 2018; Zhang et al., 2012). Both methods were shown to be efficient in generating CMs.

One advantage of the suspension culture method is the higher quantitative CM output seen in this approach (Breckwoldt et al., 2017; Eschenhagen et al., 2015). In the standardised protocol developed by Breckwoldt et al. (2017), cardiac differentiation with embryoid body (EB) formation in spinner flasks is performed within 14 days in large scale. Subsequently, CMs are directly used for the generation of engineered heart tissues (EHTs; cf. 1.5). On the other hand, monolayer protocols are reported to have higher efficiencies in CM percentages (Musunuru et al., 2018). The principle of the “Matrix Sandwich Method” outlining the important role of extracellular matrix was shown to lead to CM purity of over 98% (Zhang et al., 2012). Still, cell lines are displaying distinct differentiation efficiencies and the optimal protocol must be individually determined for each cell line (Batalov and Feinberg, 2015; Eschenhagen et al., 2015; Kattman et al., 2011).

Nevertheless, differentiation efficiencies have been improved substantially over the last years. Moreover, several purification methods (Rajala et al., 2011) have been implemented in order to gain higher CM outputs such as fluorescence-activated cell sorting of labelled CMs (Hattori et al., 2010). Today, even the specific differentiation of hiPSCs into CM subtypes is possible (Cyganek et al., 2018; Devalla and Passier, 2018) allowing for instance modelling of the human atrium with clinical respect to atrial fibrillation (Lemme et al., 2018). Conclusively, the opportunities to differentiate hiPSCs into CMs *in vitro* have tremendously

increased and have enabled its usage for further applications such as disease modelling (cf. 1.2).

1.5 Human engineered heart tissues (EHTs)

In general, the idea of tissue engineering is no novelty. It arose from the belief that a higher sophisticated model would reflect the organ of interest in a more realistic way. In the cardiovascular field, Eschenhagen et al. (1997) reported about a “new heart muscle model system”, which provides a novel method of culturing cardiomyocytes *in vitro*. In this method, embryonic chick CMs were cultured in a collagen-based matrix and showed coherent beating in a three-dimensional setting, which could subsequently be measured in terms of isometric contractile force. Since then, this method has been further improved and evaluated for different applications. For instance, Zimmermann et al. (2002) suggested that EHTs derived from neonatal rat cardiac cells might provide a tool for cardiac repair, when grafts are transplanted on diseased myocardium. In addition, it could serve as a new drug screening platform (Eder et al., 2016; Hansen et al., 2010). Furthermore, EHTs were also proposed for its use for disease modelling. Especially neonatal rat and mouse cardiac cells were used for generation of EHTs, at last. While rat EHTs were easier to generate and to handle compared to murine EHTs, the last were especially interesting in case of disease modelling since they could be generated from mouse cardiac cells carrying specific genetic modification (Stohr et al., 2013). Since the advent of hESC/hiPSC technologies, EHTs have also been generated from human CMs after cardiac differentiation of stem cells (Breckwoldt et al., 2017; Schaaf et al., 2011). Breckwoldt et al. (2017) showed that EHTs can be generated from hiPSCs in a standardised manner that opens the possibility to be used for subsequent downstream applications. Here, EHTs are generated in 24-well plates in a fibrin-based matrix in strip format as shown in Figure 7.

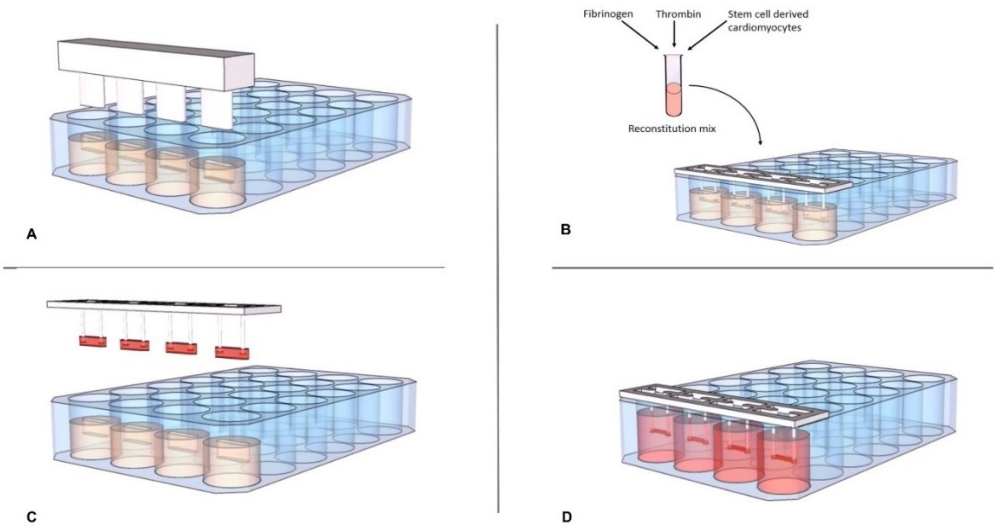

Figure 7: Generation of EHTs in 24-well plates
Depicted is the procedure of EHT generation. Casting molds are prepared with the use of Teflon spacers in agarose (A). The EHT mastermix, which is composed of different components like fibrinogen, thrombin and hiPSC-CMs, is filled into the casting molds (B). After solidification, EHTs are transferred into a media-containing 24-well plate and cultivated (C and D). Figure adapted from "Engineerd heart tissue Hamburg" accessed August 2019 (https://www.youtube.com/watch?v=UA8QJ9qTg-M).

Beside the optimisation of the protocols to generate EHTs, the measurement systems have been improved as well. Hansen et al. (2010) established a method to automatically measure EHTs in a video-optical measurement system that allows for high-throughput measuring of tissues and analyses several contractile parameters, e.g. force, frequency, contraction time ($T1_{20\%}$) and relaxation time ($T2_{20\%}$) as visualised in Figure 8.

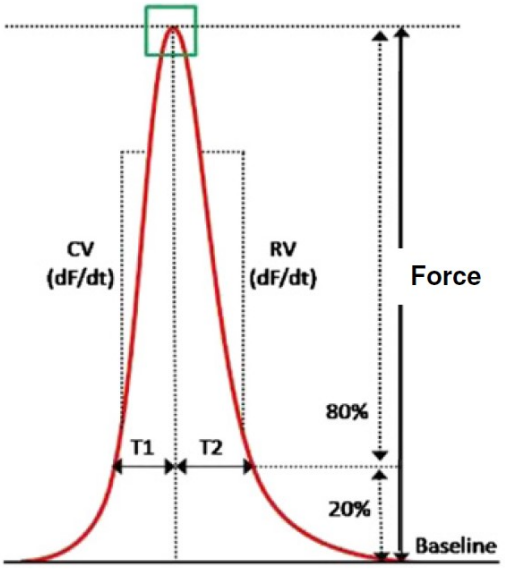

Figure 8: Schematic depiction of analysed contraction peaks in a video-optical measurement system
Depicted are the parameters force, contraction time ($T1_{20\%}$), relaxation time ($T2_{20\%}$), contraction velocity (CV) and relaxation velocity (RV). Figure adapted from Eder et al. (2016).

In respect of morphology, immunofluorescence images of CMs in EHTs showed improved alignment in longitudinal orientation and regular sarcomeric organisation as opposed to 2D cultures (Mannhardt et al., 2016; Schaaf et al., 2011). Moreover, measurements in EHTs are reported to recapitulate basic physiologic mechanisms in the human heart such as Ca^{2+} handling (Stoehr et al., 2014), drug response (Mannhardt et al., 2016; Mannhardt et al., 2017) and electrophysiologic properties (Uzun et al., 2016) with some limitations described. Especially in terms of maturation, culture in EHT format improves metabolic and

electrophysiologic aspects in the CMs when compared to monolayer cultures (Ulmer et al., 2018; Uzun et al., 2016). Furthermore, EHTs are capable of pacemaking, which showed improved morphologic and functional characteristics (Hirt et al., 2014).

In particular, EHTs derived from hiPSC-CMs display all advantages of the hiPSC technology and, in combination with genome editing, they are a highly elaborated method for *in vitro* human disease modelling without usage of animal-derived cells.

1.6 Gene therapy

In principle the idea of gene therapy is to heal the underlying genetic defect of a disease so that full-length functional protein can be translated in the cell. Therefore, gene therapy is a promising option to cure genetic diseases such as Duchenne muscular dystrophy (DMD) or HCM. Since current therapies for monogenetic diseases mostly aim at symptomatic relief but do not target the disease itself, gene therapy could overcome this issue. In the past, different approaches of gene therapy such as genome editing with CRISPR/Cas9, exon skipping, allele-specific silencing, spliceosome-mediated RNA *trans*-splicing and gene replacement have been tested in a wide range of settings like animal or hiPSC-based models. These strategies display differences in efficiency and show individual advantages and disadvantages as reviewed previously (Ohiri and McNally, 2018; Prondzynski et al., 2019b).

The CRISPR/Cas9 tool would allow direct targeting of the mutation in the genome and, together with a template, repair the diseased allele via HDR (cf. 1.3). A group around Leonela Amoasii was able to restore cardiac dystrophin levels up to 90% in a mouse model of DMD (Amoasii et al., 2017). One year later, they even published a study transferring their approach to a dog model of DMD with comparable cardiac dystrophin levels (Amoasii et al., 2018). Another study, published by Ma et al. (2017), claimed the ability to correct a pathogenic heterozygous mutation in human embryos. This study led to ethical debates and controversial discussions. In many countries such as Germany experimental interventions into human germline are forbidden by law. Ethical committees argue that other possibilities like preimplantation genetic diagnosis (PGD) followed by *in vitro* fertilisation (IVF) allow prevention of germline transmission without direct manipulation in the germline. Moreover, other researchers in the field have doubted the reliability and validity of the results reported in the study (Egli et al., 2018). Recently, the Chinese He Jiankui and colleagues have reported the manipulation of the *CCR5* gene in human twins in order to provide resistance against HIV transmission. This statement immediately arose concerns from several other researchers who demanded for stricter regulations and rules for the use of these techniques

in human embryos (Wang et al., 2019; Zhang et al., 2019). They claim that genome editing is still not fully improved and the dimensions and risks of potential off-targets or side-effects are still too high. Hence, CRISPR/Cas9 is currently no option for human gene therapy *in vivo*, but remains important for advancing research using animal experiments or for *in vitro* experiments.

Another approach providing full-length protein is known as gene replacement therapy (Figure 9). Here, gene therapy is conducted via injection of adeno-associated virus (AAV) harbouring the wild-type cDNA, which is subsequently transcribed and translated into full-length protein. The advantage of AAVs is that they are barely pathogenic themselves, cause only mild immune response, they are able to transduce differentiated cells and do not integrate into the genome (Galli et al., 2018; Prondzynski et al., 2019b). Different serotypes of AAVs lead to distinct specificity of tissue that is preferentially transduced by the virus. A single injection of AAV9 was shown to be successful in a mouse model of neonatal cardiomyopathy due to a truncating *MYBPC3* mutation (Mearini et al., 2014). The injected AAV9 carrying the full-length *MYBPC3* cDNA under the control of the cardiac troponin T promoter increased mRNA and protein levels of cMyBP-C substantially. This led to prevention of the development of the disease phenotype (Mearini et al., 2014). These encouraging results were additionally confirmed in a model of HCM based on hiPSC-CMs (Prondzynski et al., 2017). One limitation of AAV approaches is that they are reported to be only able to carry DNA sequences of less than 5 kbp, which makes it difficult to use, if larger genes such as dystrophin or laminin should be replaced (Galli et al., 2018). In contrary, Mearini et al. (2014) have shown that packaging 5.4 kbp of the *MYBPC3* gene into AAV9 was successful.

Figure 9: Principle of gene replacement therapy
The vector is an AAV carrying the full-length cDNA, which will be transcribed and translated into a full-length protein and therefore replaces missing protein due to loss-of-function mutations. Figure adapted from Prondzynski et al. (2019b).

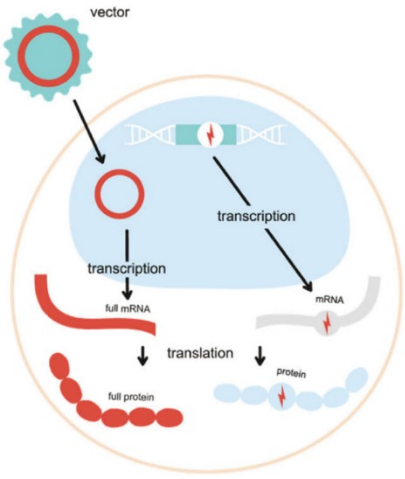

Other strategies of gene therapy such as exon skipping with the use of antisense oligonucleotides, allele-specific silencing or RNA *trans*-splicing were also tested in the past years (Behrens-Gawlik et al., 2014; Prondzynski et al., 2019b). Exon skipping and allele-specific silencing require different medicinal products for different mutations and are therefore less feasible than gene replacement therapy. The major issue of RNA *trans*-splicing is the very low efficiency, for instance in HCM models in mice and hiPSC-CMs (Mearini et al., 2013; Prondzynski et al., 2017).

In summary, several options for gene therapy exist so far. Improvements are especially necessary regarding tissue specificity, long-term expression and circumvention of immune reactions upon the gene therapy product (Galli et al., 2018; Ohiri and McNally, 2018; Prondzynski et al., 2019b). In case of HCM due to truncating *MYBPC3* mutations, gene replacement therapy is in the current focus since haploinsufficiency is often reported and this would be directly addressed by the exogenous cDNA providing the full-length protein. In the future, a combination of CRISPR/Cas9 packaged into the AAV might also be an option, although today this approach is still in its early days and not safe enough to be tested in clinical trials (Prondzynski et al., 2019b).

1.7 Aim of the study

The aim of the study was to create an *in vitro* disease model based on hiPSC-CMs in order to investigate severe cardiomyopathies carrying bi-allelic *MYBPC3* mutations in a simplified human context. Since earlier studies on cardiomyopathies are mainly based on mouse models, the use of hiPSC-CMs generated from an index patient would be a next step towards a better understanding of the disease and future treatment options for the affected neonates.

[1] The purpose of using the CRISPR/Cas9 genome editing technology was to genetically modify an existing heterozygous (c.2308G>A transition in exon 23 of *MYBPC3*) hiPSC line (CMS32) derived from a female patient with diagnosed HCM. This mutation is located on the last nucleotide of exon 23 and is therefore supposed to impair splicing (Helms et al., 2014). The goal of the CRISPR/Cas9 approach was then to create an isogenic control with equal genetic background and only differing for the absence of the mutation. Moreover, it was planned to introduce a pathogenic mutation (c.2827C>T in exon 27 of *MYBPC3*) known as a founder mutation in the Netherlands and which induces a PTC, in order to obtain a compound heterozygous hiPSC line (Carrier et al., 2015). The creation of the bi-allelic mutated cell line would therefore be the basis to model the severe state of the children born with double-truncating *MYBPC3* mutations. The project outline of the CRISPR/Cas9 approach is visualised in Figure 10.

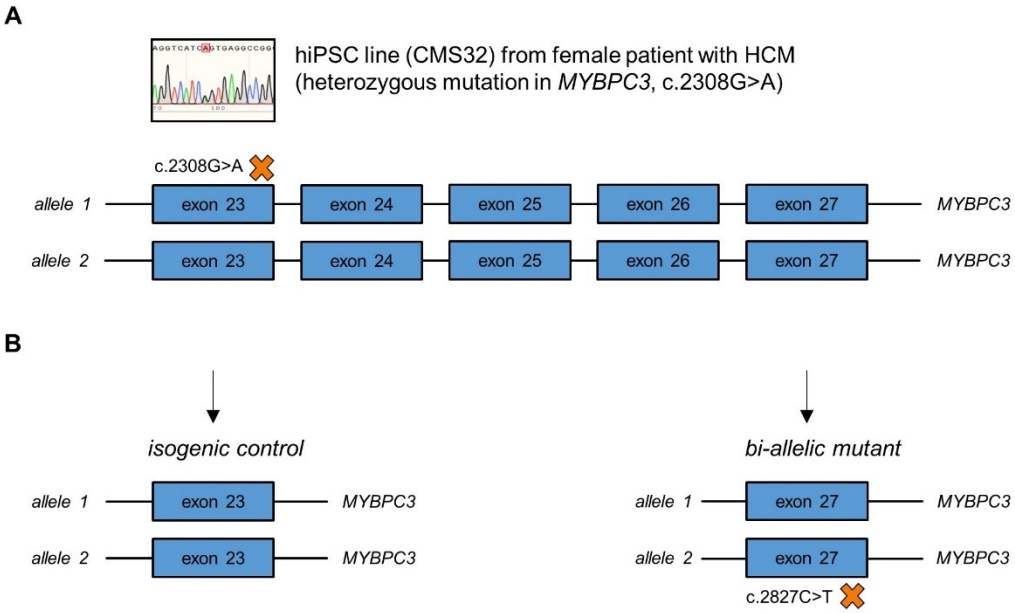

Figure 10: Project outline - CRISPR/Cas9
A *HiPSC line from a female HCM patient carrying a heterozygous MYBPC3 mutation (c.2308G>A).* ***B*** *Generation of an isogenic control for the patient's mutation and introduction of a second mutation (c.2827C>T) by CRISPR/Cas9 genome editing.*

[2] It was planned to evaluate the consequence of the patient's mutation since its location on the last nucleotide of exon 23 was expected to induce skipping of the respective exon at mRNA level (Helms et al., 2014). In order to verify this, the *MYBPC3* transcripts in the septal myectomy from the patient and in heterozygous hiPSC-CMs were to be analysed. In addition, inhibition of the NMD in hiPSC-CMs using drugs known from previous publications (Kosmidis et al., 2016; Vignier et al., 2009) to stabilise nonsense mRNA was planned.

[3] Phenotypic analysis of this *in vitro* disease model was the following goal after establishment of the hiPSC lines with CRISPR/Cas9 and differentiation into CMs. Phenotypic analysis was to be conducted in 2D culture as well as 3D EHTs in molecular (DNA, RNA and protein level) and functional aspects (contraction measurements in EHTs). The experimental workflow is visualised below (Figure 11).

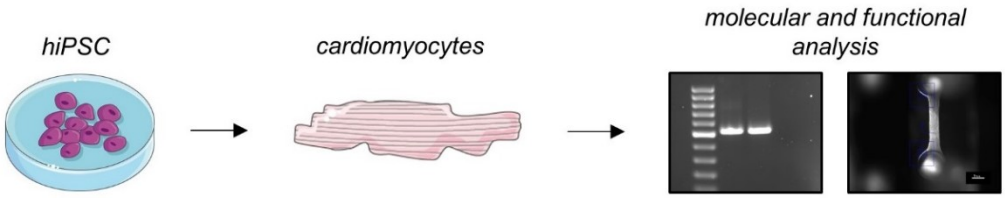

Figure 11: Project outline - Disease modelling
Cardiac differentiation from all three cell lines (CMS32, isogenic control, bi-allelic mutant) and phenotypic analysis in 2D and 3D culture. HiPSC and CM images from https://smart.servier.com/, accessed August 2019.

[4] Gene therapy with the gene replacement strategy by transduction of an AAV6 carrying the full-length wild-type cDNA of *MYBPC3* was planned in the diseased cell lines in order to test this as a possible treatment option for the affected patients with *MYBPC3* mutations.

2 Material and methods

A list of all used materials can be found in the supplement (cf. 10.3) if not listed explicitly below.

2.1 Generation and cultivation of human-induced pluripotent stem cells

2.1.1 Reprogramming of patient-derived fibroblast

A skin biopsy was taken from a female patient with HCM, who underwent surgical myectomy due to her progressed stage of disease in the University Medical Center Hamburg (UKE, Hamburg). The patient gave her written informed consent for research purposes and the study was approved by the ethical committee of the UKE, Hamburg. The following procedure of fibroblast culture and reprogramming by use of non-integrating Sendai virus into hiPSCs was kindly performed by the HEXT Stem Cell Core Facility (Dr. Sandra Laufer and Dr. Aya Shibamiya, UKE, Hamburg).

2.1.2 Culture of human-induced pluripotent stem cells

The hiPSCs were cultured in conditioned medium in 2D culture plates up to passage number 19 to make sure that any residual virus particles of reprogramming have been cleared. Then, cells were adapted stepwise to FTDA culture medium over one week. Furthermore, cells were checked for the absence of bacterial contamination and for a typical stem cell morphology. When hiPSCs were confluent with at least 80% density, they were passaged. Therefore, they were washed once in pre-warmed 1 x PBS, detached with 1 mL/well Accutase™ supplemented with 10 µM Y-27632 (reduction of apoptosis by ROCK inhibition) and incubated at 37 °C for 5-10 min. The detached cells were then collected in a 15-mL Falcon tube and the enzyme reaction was stopped with the same amount of media as Accutase™ solution used before. After a centrifugation step (200xg, 2 min), the supernatant was aspirated, cells were resuspended in culture medium and counted with the CASY Cell Counter & Analyzer (OLS®). According to further experiments, the cells were seeded at different densities (from 300,000 up to 600,000 per six-well) on Geltrex™ precoated 6-well plates (Geltrex™ 1:100 diluted in RPMI 1640 and incubated at least 40 min at 37 °C). Medium was changed daily with 2-3 mL/well FTDA.

2.1.3 Creation and characterisation of a master cell bank of human-induced pluripotent stem cells

The principle of a hiPSC master cell bank (MCB) is to create a big stock of stem cells at a low passage number, which are checked for certain quality markers and which can be used then to perform experiments with quality controlled cells. These quality markers include a good stem cell morphology as determined by eye-microscopy (e.g. cells with large nucleus and scant cytoplasm), the absence of any evident bacterial contamination and mycoplasma infection by polymerase chain reaction (PCR), a normal karyotype and a highly positive SSEA3 pluripotency marker (Breckwoldt et al., 2017). Therefore, hiPSCs were expanded in Geltrex™ precoated T75 culture flasks under hypoxic conditions (37 °C, 5% CO_2, 5% O_2). Upon 100% confluency, cells were detached with Accutase™ as described above (accordingly 5 mL/T75). Shortly before, 500 µL of the at least 24 hours unchanged medium was collected in a 1.5-mL Eppendorf tube for subsequent PCR to detect mycoplasma. The mycoplasma PCR was kindly performed by June Uebeler (IEPT) and included a positive and negative control. For freezing, aliquots with 1 million cells in 1 mL FCS supplemented with 10% DMSO were placed in Mr. Frosty Freezing Containers containing isopropanol and cooled at -80 °C over night. The next day, the cryovials were transferred to -150 °C freezers for long-term storage. Additionally, one million cells/cell line were collected for DNA extraction to determine the karyotype as well as pluripotency analysis. For DNA extraction, the cells were centrifuged in a 1.5-mL Eppendorf tube and the pellet was washed once in 1 x PBS. DNA extraction was performed using the DNeasy® Blood & Tissue Kit (Quiagen) according to the manufacturer's protocol. Resulting DNA concentrations were determined with the NanoDrop™ ND-1000 Spectrophotometer. Karyotype analysis was performed with the NanoString nCounter® Human Karyotype Panel Assay. The Panel includes 338 individual loci distributed on all 24 chromosomes. The amplification counts were normalised to karyotypic normal cell lines from the institute as determined by G-banding (gold standard). NanoString experiments were kindly performed by Elisabeth Krämer and Dr. Maksymilian Prondzynski and analysis was done by Dr. Giulia Mearini. For determination of pluripotency, one million cells were resuspended in FACS buffer (1 x PBS with 5% FCS). After a centrifugation step, half of the cells were stained with an antibody against SSEA3, which is a surface protein that is used as a marker for pluripotency (Kempf et al., 2015), and the other half was stained with an antibody with the respective isotype control. SSEA3-positive cells were counted with the FACSCanto II Flow Cytometer in the UKE FACS Core Facility (UKE, Hamburg). A threshold of at least 40% was set for pluripotency relying on previous experiments in the institute.

2.2 CRISPR/Cas9 mediated genome editing

2.2.1 Design of guide RNAs and templates for specific genome editing

The RNP-based CRISPR/Cas9 genome editing approach was planned using the Alt-R® CRISPR-Cas9 System provided by IDT®. The system consists of the crRNA (CRISPR RNA including the gRNA for specific targeting), the tracrRNA (transactivating crRNA) and the recombinant *S. pyogenes* Cas9 enzyme. The *S. pyogenes* Cas9 requires a 5'-NGG PAM at the target-site for efficient cleavage. Further information can be found at *https://www.idtdna.com*. Components of the RNP complex are depicted in Figure 12.

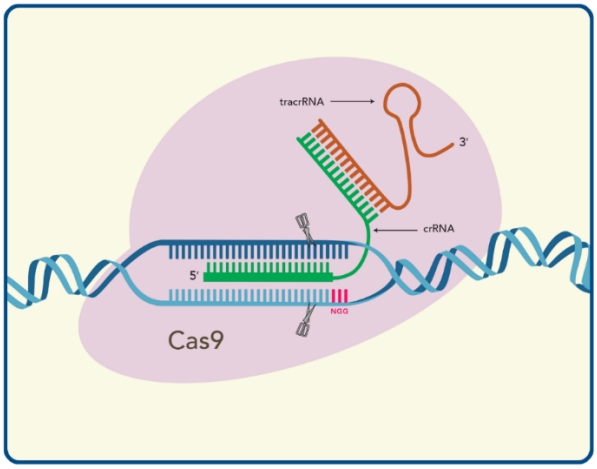

Figure 12: Components of the RNP clomplex (crRNA, tracrRNA and Cas9 nuclease; IDT®)
crRNA: CRISPR RNA; RNP: ribonucleoprotein; tracrRNA: transactivating crRNA. Figure from IDT®, https://eu.idtdna.com/pages/products/crispr-genome-editing/alt-r-crispr-cas9-system, accessed January 2019.

The guide RNAs (gRNA) were designed with the online CRISPR Design Tool *http://crispr.mit.edu/* provided by the Zhang Lab (MIT) as suggested in Ran et al. (2013). Two different gRNAs were needed to obtain an isogenic control for the patient's mutation in *MYBPC3* exon 23, referred to as CRISPR "Repair", as well as the introduction of a second *MYBPC3* mutation in exon 27, referred to as CRISPR "Mutation", which introduces a stop codon. The following two gRNAs (Table 1) were chosen due to a high on-target specificity, a close PAM to target site (Paquet et al., 2016) and minimal likelihood of off-target binding whenever possible.

Table 1: CRISPR gRNAs

CRISPR approach	**gRNAs (20 mer) (5' → 3') + *PAM***	**Quality score***	**Number of off-targets**
Repair	CACAGTCAAGGTCATCAGTG ***AGG***	49	299 (32 are in genes)
Mutation	CCATATTGTGTGCCCGCACT ***CGG***	90	75 (12 are in genes)

*The G>A nucleotide exchange of the index patient (c.2308G>A) is included in the gRNA sequence for the Repair approach and is depicted in red. gRNA: guide RNA; PAM: protospacer adjacent motif. * scored by inverse likelihood of off-target binding (100 set as maximum)*

The templates for directed genome editing via HDR were designed as 120-mer ssODNs in antisense direction with the repair/mutation around the middle of the 120-mer (Table 2). In both templates, silent or intronic mutations close to the target site were included. The sequences are as follows:

Table 2: CRISPR templates

CRISPR approach	**Antisense template (120 mer) (5' → 3')**
Repair	CGGATGGGCCCTCCTTGGGGCTGCCCCTCTGTGTTCTCCA GCTTGGACCCCGGCCGGACTCACCGATGACCTTGACTGTG AGGTTTACCTGGTCCTCGCCCACAGGGTTCTTCACTGTGA
Mutation	ACTGTCACCGGCTCCGTGGTGGTAACCGGGGCTCCAGGCC CTGCCATATTGTGTGCCCGCACTCAGAAAAGCAGCCGGGCC CCCGTGGGCAGGTCCTTCACCAGTATTGATGTGTGCTCT

Single nucleotide exchanges (silent or intronic) are indicated in green (last nucleotide of base triplet). Introduced point mutation in the mutation template is indicated in red, repaired point mutation in the repair template in blue.

2.2.2 Nucleofection and culture of nucleofected clones

One week before nucleofection, CMS32-hiPSCs from the MCB (passage 19) were thawed. HiPSC vials were thawed in a water bath at 37 °C and diluted (1:10 dilution) in FTDA medium supplemented with 10 µM Y-27632. After centrifugation (200 g for 2 min), the supernatant was aspirated and the cell pellet was resuspended in FTDA + Y medium. The cells were cultured as described above and passaged once. Seeding densities were 2 x 400,000 and 1 x 500,000 cells per well on 6-well plates. Medium was changed twice

(morning and evening) the day before nucleofection when the cells reached almost 100% confluency. The next day, the cells were checked under the microscope for normal stem cell morphology and growth behaviour. Before nucleofection, the tracrRNA (100 µM final concentration) and crRNAs were resuspended in appropriate volume of IDTE-Buffer as indicated in the IDT®delivery sheet (gRNA Repair: 100 µM; gRNA Mutation: 50 µM). The two different CRISPR approaches were handled separately. A 12-well plate was precoated with Matrigel® (1:60 in RPMI 1640 and incubated at least 40 min at 37 °C). Furthermore, Y-27632 was added to the medium two hours before start in the same concentration as for normal passaging (10 µM).

The next step was the initiation of the RNP complex formation. Experimental workflow and preparation of the delivery of the RNP complex is shown in Figure 13.

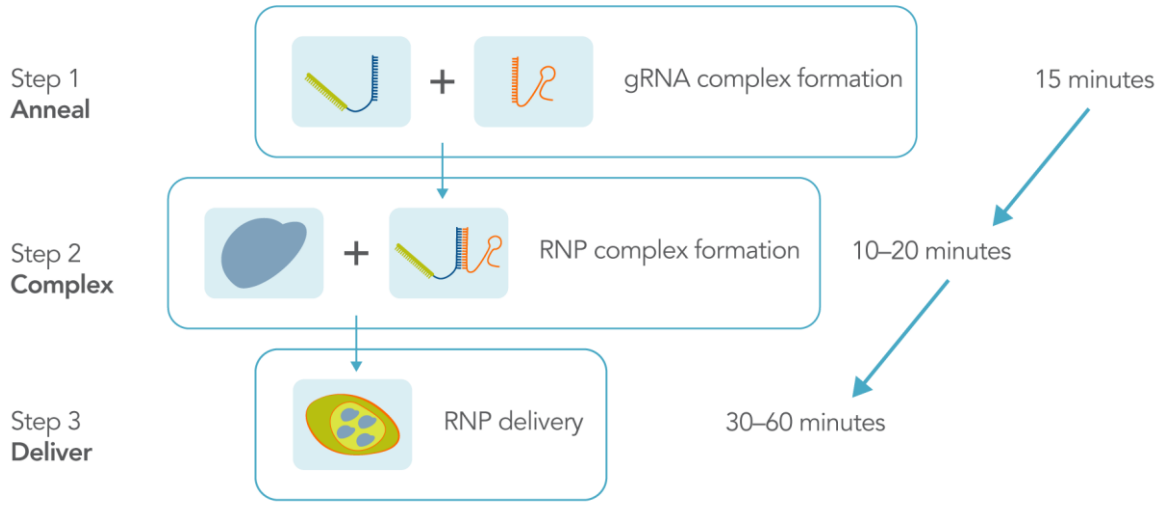

Figure 13: Delivery of the RNP complex
The indicated times may vary slightly. gRNA: guide RNA; RNP: ribonucleoprotein. Figure adapted from IDT®, https://eu.idtdna.com/pages/products/crispr-genome-editing/alt-r-crispr-cas9-system, accessed December 2019.

Five µL crRNA (10 µL in case of gRNA Mutation) and 5 µL tracrRNA (100 µM) were mixed, annealed for 5 min at 95 °C and cooled down to room temperature (RT). In the following step, 4 µL of the annealed RNP complex were mixed each with 4 µL Cas9 protein (10 µg/µL) and incubated for one hour at RT under protection from light. In the meantime, the Alt-R® Cas9 Electroporation Enhancer was resuspended to a final concentration of 100 µM in IDTE-Buffer, and the Matrigel® precoated wells of the 12-well plate were filled with 1 mL conditioned medium per well. Next, the cells were prepared for nucleofection. They were washed, detached and counted as described in 2.1.2. Then, 800,000 cells were resuspended in 100 µL Nucleofector solution (82 µL P3 solution + 18 µL P3 supplement) and 1 µL of the ssODN (CRISPR templates; 100 µM) of the corresponding approach as well as 1 µL of the Enhancer were added to the cell suspension. Finally, 4 µL of the RNP complex

were added and the final solution was transferred into a nucleofection cuvette. Nucleofection was performed with the 4D-Nucleofector™ System (Lonza) using the program CA137. Afterwards, the cells were seeded on a 12-well plate (one well each with 800,000 per CRISPR approach as well as one well with 500,000 as a non-transfected control). The next day, 1 mL fresh conditioned medium was added to each well. After approximately 48 hours, transduction efficiency was estimated under the fluorescence microscope as the tracrRNA included a red tag for visualisation (RFP channel) and cells were seeded at low density on Matrigel® precoated 6-well plates in conditioned medium supplemented with 10 µM Y-27632. Seeding densities were 100, 2 x 250, 2 x 500 and 1000 cells for each CRISPR approach. Remaining cells were frozen as a backup. Single cells were cultured for several days, growth of cell colonies was monitored and medium was changed daily (conditioned medium). Exceptions were the first day after seeding, where no medium was changed, and the second day after seeding, where only 1 mL medium was added to the wells.

After nine days of culture, the size of colonies was big enough for picking. Therefore, medium was changed with addition of 10 µM Y-27632 at least two hours before. Additionally, 48-well plates were prepared with Matrigel® (1:60 in RPMI 1640) and after more than 40 min wells were filled with conditioned medium (supplemented with 10 µM Y-27632). For picking of colonies, the EVOS microscope was placed under the hood and cell colonies were scraped and aspirated manually with a 100-µL tip, selecting only large, round shaped and dense colonies. Besides, only colonies, that grew solely and did not have contact to surrounding colonies, were picked. Passage number at this time point was 24. The day after picking, medium was dropped on the wells. The days after, normal medium change was conducted (conditioned medium, approximately 250 µL per well). Each clone was cultured for an appropriate number of days until the well was confluent. Then, cells were passaged 1:2 on 2 x 48-wells. Therefore, the wells were washed once in 1 x pre-warmed PBS and covered with EDTA. After ten minutes incubation at 37 °C, EDTA was aspirated and 500 µL conditioned medium (supplemented with 10 µM Y-27632) was dropped on the cells. Cells were collected with a 1000-µL tip. Equal amounts of medium cell suspension were distributed on the two prepared 48-wells. The cells were cultured again until confluency and the first days medium was only added dropwise to the wells to let the cells attach. Finally, one well was harvested as cell pellet and stored at -20 °C for DNA extraction and one well was frozen in 1 mL FCS with 10 % DMSO in a cryovial at - 150 °C.

2.2.3 Genotyping of clones

DNA was extracted from each cell pellet per clone with the use of the QIAcube® HT workstation (Qiagen) and the QIAamp® 96 DNA QIAcube® HT Kit (Qiagen) for automated DNA extraction of up to 96 samples per run. DNA extraction was performed according to the manufacturer's instructions provided in the Kit. DNA of clones that were harvested later was extracted manually with the DNeasy® Blood & Tissue Kit (Qiagen) according to the manufacturer's instructions. After DNA extraction, DNA content was measured with the NanoDrop™ ND-1000 Spectrophotometer. PCR amplification was performed with the use of the DreamTaq DNA Polymerase (Thermo Fisher Scientific) with the primers (Table 3) and in the conditions (Table 4 and Table 5) described below. Primers were designed using the Primer-BLAST designing tool provided by the National Center for Biotechnology Information (NCBI).

Table 3: Primers for genotyping CRISPR clones

CRISPR approach	**Primers (5' → 3')**	**Product size**
Repair	F: GGCCTCTGGGGTCTGACT R: AGGCGGCTCCCACTGTACT	1011 bp
Mutation	F: GCTGACAGAGCACACATCGA R: TTCTGGGCAGAGCATTCTGG	247 bp

F: forward; R: reverse.

Table 4: PCR mixture (DreamTaq)

Substance	**1x**
Nuclease free water	up to 50 µL
10x DreamTaq Green Buffer	5 µL
2 mM dNTPs	5 µL
Primer forward (10 µM)	0.4 µL
Primer reverse (10 µM)	0.4 µL
DreamTaq DNA Polymerase	0.25 µL
Genomic DNA	50 ng

Table 5: Touchdown PCR program (DreamTaq)

Step	Temperature [°C]	Time	Cycles
Initial denaturation	95	3 min	
Denaturation Annealing Elongation	95 *68 - 63 72	30 s 30 s 1 kbp/min	11x
Denaturation Annealing Elongation	95 63 - 58 72	30 s 30 s 1 kbp/min	24 – 30x
Final Elongation	72	7 min	
Hold	4	∞	

**-0.5 °C/cycle*

After PCR, the samples were loaded on an 1% or 1.5% agarose gel to check for specific amplification. For visualisation of PCR fragments, Midori Green Advance DNA Stain (Nippon Genetics Europe; 7 µL for a large 150 mL agarose gel and 5 µL for a small 70 mL agarose gel) was mixed into the agarose gel. After solidification of the gel, 20 µL or 15 µL of the DreamTaq unpurified PCR reaction were loaded on a large or a small agarose gel, respectively. The samples were directly loaded without use of loading dye since this was included in the green buffer of the DreamTaq DNA polymerase. As a DNA standard the Gene Ruler™ 100-bp or 1-kb DNA Ladder (Thermo Fisher Scientific) was used dependent on the product size. Four µL of this standard were loaded in the first lane. Agarose gels were run for at least 30 min up to 1 h according to product length and gel size (large gels: 5 min at 80 V and then 120 V; small gels: 5 min at 70 V and then 80 V). Bands were detected with the ChemiDoc™ Touch Imaging System from Bio-Rad. Successfully amplified products were then prepared for Sanger sequencing by Eurofins genomics. The sequencing conditions and required sample concentrations as well as the right sample volume can be found at *https://www.eurofinsgenomics.eu/en/custom-dna-sequencing/eurofins-services/tubeseq-service/*. Sequencing results were analysed using SnapGene®.

2.2.4 Off-target analysis

The online CRISPR Design Tool that was used for the design of the gRNAs also provided a list of potential genome wide off-target binding sites. The top 10 off-targets for both gRNAs were analysed. Off-target sequences are as shown in Table 6 and Table 7.

Table 6: Repair gRNA off-targets

Repair gRNA	Off-target sequence (5' → 3') + *PAM*	Number of mismatches
OT 1	CAGGCTCAAGGTCATCAGTG ***AGG***	3
OT 2	CACAGTCAATGTCAACAGTG ***TGG***	2
OT 3	TAAAGCCAAGGTCATCAGTG ***AAG***	3
OT 4	CATTGTCAAGGACATCAGTG ***GGG***	3
OT 5	GCCCTTCAAGGTCATCAGTG ***TGG***	4
OT 6	CACAGTCAAGGACATCAGGG ***CAG***	2
OT 7	CAGAGTCAAAGTCATCAGGG ***TAG***	3
OT 8	CAGAATGCAGGTCATCAGTG ***CAG***	4
OT 9	CACTGTAAAGGCCATCAGTG ***TGG***	3
OT 10	CTCTCTCATGGTCATCAGTG ***TAG***	4

Mismatches are indicated in red. gRNA: guide RNA.

Table 7: Mutation gRNA off-targets

Mutation gRNA	Off-target sequence (5' → 3') + *PAM*	Number of mismatches
OT 1	CCAAGTTGTGTGCCTGCACT ***CAG***	3
OT 2	CAATATTGTATGCCTGCACT ***AAG***	3
OT 3	GCTTATTTTGTGCCCGAACT ***TAG***	4
OT 4	ACAAATTTTGTGCCCGCATT ***GAG***	4
OT 5	CCACAGTGTGTGCCTGCACT ***CGG***	3
OT 6	CCTTATTGGCAGCCCGCACT ***CGG***	4
OT 7	CTATATTTTCTGCCAGCACT ***GGG***	4
OT 8	CCATTTTGTTCACCCGCACT ***TGG***	4
OT 9	CCTTAATGTCTGCCCGTACT ***TGG***	4
OT 10	CCCTGGTGTGTGCCCGCAAT ***GGG***	4

Mismatches are indicated in red. gRNA: guide RNA.

Primers for the amplification of the off-target regions were designed using Primer-BLAST (NCBI). Primers are shown in Table 8 and Table 9.

Table 8: Primers for Repair gRNA off-targets

Repair gRNA	Primers (5' → 3')	Product size
OT 1	F: CTGCCAAGAGGACCACAAGT R: AGTGGTTGTTGCTCTTCCCG	346 bp
OT 2	F: GTCAGGGTGGAGGAGACAGA	327 bp

	R: GCAACACCGGAAACTAGGAG	
OT 3	F: TCATGATGGGTGGAGGTTGG R: TCTGGAAGTTCCTTGAAGGGG	338 bp
OT 4	F: AGTTGGCCATGGCTGCTTAT R: GGGGTGAACGAGTGCTTCTT	481 bp
OT 5	F: GCATTTTGGGGTGTTAAAAGTGC R: TGAACTTGAGTGCAAGGCAGA	383 bp
OT 6	F: TGGTTAGCTCATGTGCCACT R: TGTGTGGAACAGCTGAGCAT	370 bp
OT 7	F: CCATCAGGACTGAGGGAAGC R: AAGGTGGGGTGGTCCTCTTA	458 bp
OT 8	F: ACTGGAGGCCTTGGGAAAAA R: TCCGAGGGACCAGATCACTG	511 bp
OT 9	F: GGGAGGATGGGGGAAAATAGC R: CAGCAGAAAGACTGCCTCGG	399 bp
OT 10	F: CAGTGGCCTCTAAATCGGGG R: CTGAGAGGCGGATAGAAGCC	402 bp

F: forward; gRNA: guide RNA; R: reverse.

Table 9: Primers for Mutation gRNA off-targets

Mutation gRNA	**Primers (5' → 3')**	**Product size**
OT 1	F: TTACTTGGCCGTGTAGCCTG R: CCATGGCTTCATGAGTAGGC	669 bp
OT 2	F: AGGGCTAAATCCATCAGCACC R: TGGTGTATCCTGGACCATGC	508 bp
OT 3	F: CATTTACAGGCGTACTTCGCA R: TCAGCATTTGTGAAAAGTGTCCC	162 bp
OT 4	F: GCTTCAAAGGGTACAGAGCTA R: AGAAGGCAGGAAAAGATGAGTG	562 bp
OT 5	F: GCTAAGGAGCCTGTGTGGTT R: TATCCCTACGGGAAGCCCAA	310 bp
OT 6	F: GAGGAGGAGGATGGCTCTGA R: TCGGGGAAGTCGCCTACA	416 bp
OT 7	F: TCCGAGTGAGCAAATCGCAT R: AGCAGGCCACTTTTCAGTGT	418 bp
OT 8	F: TGGTAACTTCCACTCGCTGT R: GGCATCAGGTATCAGGTGTGT	266 bp

OT 9	F: AAAGCAAAGCAGTGGGTCCT R: CCCCTCCCCTGCACATAGTA	430 bp
OT 10	F: CTGCCTCCTTCCTGACTTGG R: AGACTCTACAGGGGCTGAGG	405 bp

F: forward; gRNA: guide RNA; R: reverse.

Amplification by PCR was performed using the DreamTaq Green DNA Polymerase (Thermo Fisher) as described in 2.2.3. Touchdown conditions were adapted to the respective product sizes and annealing temperatures.

PCR products of the off-target regions were loaded on agarose gels as described in 2.2.3. Successfully amplified products were subsequently purified using the QIAquick® PCR Purification Kit (Qiagen) according to the manufacturer's instructions. Products were then prepared for sequencing by Eurofins genomics. Sequencing results were compared to wild-type sequences downloaded from NCBI using SnapGene®.

2.2.5 Cloning of PCR fragments

Successfully CRISPR-modified clones were subcloned to validate their genomic state. Therefore, a genotyping PCR was performed (cf. 2.2.3) but with the use of the PrimeSTAR® HS DNA Polymerase to create blunt-end PCR fragments needed for the cloning into the vector of the CloneJET PCR Cloning Kit (Thermo Fisher Scientific). PCR mixture as well as PCR program are listed below (Table 10 and Table 11). Annealing temperatures and elongation time were adapted to the length of the amplified fragment.

Table 10: PCR mixture (PrimeSTAR® HS DNA Polymerase)

Substance	1x
Nuclease free water	up to 50 µL
5x PrimeSTAR® Buffer	10 µL
2.5 mM dNTPs	4 µL
Primer Forward (10 µM)	0.5 µL
Primer Reverse (10 µM)	0.5 µL
DMSO	1 µL
PrimeSTAR® Polymerase	0.5 µL
Genomic DNA	50 ng

Table 11: Touchdown PCR program (PrimeSTAR® HS DNA Polymerase)

PCR step	Temperature [°C]	Time	Cycles
Denaturation	98	10 s	11x
Annealing	*68 – 63	30 s	
Elongation	72	1 kbp/min	
Denaturation	98	10 s	24 – 30 x
Annealing	63 -58	30 s	
Elongation	72	1 kbp/min	
Final Elongation	72	7 min	
Hold	4	∞	

**-0.5 °C/cycle*

Primers for subcloning were the same as for genotyping of the respective CRISPR approach (Table 3) but with a new forward primer for the Mutation CRISPR approach (Primer 5'→ 3': AGCAGTGCGAAATCAGCAAC; Product size: 734 bp). After visualisation of the PCR fragments on an agarose gel (PrimeSTAR® products were mixed with a 6x loading dye - Thermo Fisher Scientific - before loading) and purification with the QIAquick® PCR Purification Kit (Qiagen) as described before, they could directly be cloned into the vector according to the protocol of the kit (ligation). For the transformation TOP10 competent *E.coli* were thawed on ice and 3 µL of the ligation mixture were added to the bacteria. One negative control was included without ligation mixture. Bacterial tubes were mixed gently, incubated for 30 min on ice, then for 45 s at 42 °C (heat shock) and again 5 min on ice. Then, 200 µL of SOC medium was added to each tube and bacterial outgrowth was performed for 30 min to 1 h at 37 °C shaking gently at 200 rpm. Afterwards, bacteria were plated on agar plates containing 0.1 mg/mL ampicillin. The agar plates were incubated at 37 °C over night. The next day, single colonies were picked and incubated once more over night in 2 mL LB medium containing 0.1 mg/mL ampicillin. Control plates were checked for absence of colonies due to lack of ampicillin resistance. One day after, pellets from 1.5 mL of bacterial suspension were taken and plasmid isolation was performed with the NucleoSpin® Plasmid Kit from Macherey-Nagel according to their protocol. Plasmid concentrations were determined with the NanoDrop™ ND-1000 Spectrophotometer. Plasmids could directly be sent to Eurofins genomics for sequencing in the required concentrations together with the T7 F Primer (Primer 5'→ 3': TAATACGACTCACTATAGGG) and sequences were analysed with SnapGene®.

2.3 Generation of hiPSC-CMs from hiPSCs

2.3.1 Monolayer based protocol for cardiac differentiation

The monolayer based protocol used for cardiac differentiation in this work is adapted from two published protocols (Breckwoldt et al., 2017; Mosqueira et al., 2018). HiPSCs were thawed approximately one week before differentiation was started. Expansion was conducted for two to three passages depending on the CM number needed eventually. For seeding, 6-well plates were precoated with the Matrigel® containing high growth factor (1:60 in RPMI 1640) and incubated at least for one hour at 37 °C. Precoated plates could be stored at 4 °C and used within one week. Seeding on the Matrigel® plates was performed as described in 2.1.2. Seeding densities varied from 300,000 cells per well up to 500,000. Cells were cultured as usual in FTDA medium for up to four days until they reached confluency of 70-80%, the major critical step in the protocol. Therefore, confluency was evaluated frequently under the microscope. When optimal confluency was reached, 1.5 mL/well pre-warmed Cheese Stage 0 medium (cf. 10.3.1) was added to the cells and culture plates were transferred to normoxic conditions (37 °C, 5% CO_2, 21% O_2). After 12-16 h, the appearance of typical “Cheese” holes was evaluated under the microscope. Medium was renewed with 2 mL/well of Cheese Stage 1 medium. Mesoderm induction was initiated by BMP4 and activin A in Stage 0 and 1 medium. Next medium change was performed 48 hours after Stage 1 (2 mL/well of Cheese Stage 2.1 medium). At this point of time, a huge cell death was visible. The differentiation into the cardiac lineage was obtained by inhibition of WNT signalling pathway by adding XAV 939 and KY 02111 in Stage 2.1 and 2.2 medium. Again 48 h later, Cheese Stage 2.2 medium (2 ml/well) was added to the cells and once more 48 h later, the final Cheese feeding medium was added (3 ml/well). From this point of time on (seven days after Stage 0), medium was changed every two days with Cheese feeding medium (3 ml/well) and cells were checked for visual beating under the microscope.

2.3.2 Dissociation of hiPSC-derived cardiomyocytes (hiPSC-CMs)

The dissociation protocol of hiPSC-CMs was adapted from Breckwoldt et al. (2017). HiPSC-CMs were washed twice with pre-warmed HBSS minus Ca^{2+}/Mg^{2+} (2 ml/well) and dissociation was induced with 1 mL/well collagenase II solution (cf. 10.3.9). Incubation time varied between one and two hours. After hiPSC-CMs started to detach, they were collected in a 50-mL Falcon tube by triturating up to ten times up and down with a wide mouth 10-mL pipette. Wells were washed with the same amount of blocking buffer (RPMI 1640 plus

6 µL/mL DNase solution) and the enzyme reaction was stopped by adding the blocking buffer to the collagenase solution. HiPSC-CMs were centrifuged for 10 min at 100 g and afterwards resuspended in 5 - 20 mL warm RPMI 1640 according to the size of the cell pellet. If clumps remained after resuspending thoroughly, cells were filtered through a 100-µm cell strainer (Falcon). Cell number was determined making use of a Neubauer chamber. Subsequently, CMs were either prepared for freezing (cf. 2.3.3) or resuspended in EHT medium for further cultivation in monolayers (cf. 2.4.1) and EHT generation (cf. 2.5.1).

2.3.3 Freezing of cardiomyocytes

The CMs were separated into different 15-mL Falcon tubes according to the desired cell number per freezing aliquot and centrifuged (10 min, 100 g). The supernatant was aspirated and the cell pellet was resuspended in 1 mL freezing medium per cryovial (inactive FCS supplemented with 10% DMSO). Cell amount per cryovial varied from 1 million up to 20 million cells per vial. The vials were placed in Mr. Frosty Freezing Containers and stored at -80 °C over night. The next day, the cells were transferred into -150 °C for long-term storage.

2.3.4 Determination of cTnT-positive cells by flow cytometry

Efficiency of cardiac differentiation was determined by the percentage of cardiac troponin T (cTnT)-positive cells. After differentiation, two FACS tubes were prepared with 2 mL PBS and 200,000 cells were added each, one for cTnT-staining and one for the isotype control. After centrifugation (1200 rpm for 3 min), cells were fixed with 500 µL Histofix ® for 10 min on ice. After fixation, the cells were washed twice with PBS and then permeabilised with FACS permeabilisation buffer (PBS with 5% FCS, 0.05% sodium azide and 0.5% saponin) over night. The next day, the CMs were washed again and antibody staining was performed for at least 45 min up to over night. The cTnT-positive cells were counted with the FACSCanto II Flow Cytometer in the UKE FACS Core Facility (UKE, Hamburg). A threshold of over 60% of CMs was set as the minimum for generation of EHTs.

2.4 Monolayer based culture of hiPSC-CMs

2.4.1 Thawing and plating of cardiomyocytes

CM cryovials were thawed for 2 - 3 min in a water bath at 37 °C shaking gently by hand. Then, cell suspension was transferred to a 50-mL Falcon tube with a 1000-µL tip. The

cryovial was washed with 1 mL RPMI 1640 and added drop-wise to the cell suspension over 90 s whilst swirling slowly the Falcon tube. Afterwards, 1 mL RPMI was added in the same way over 30 – 60 s and 7 mL over 30 s. The Falcon tube was inverted carefully several times and hiPSC-CMs were centrifuged at 100 g for 10 min. After centrifugation, the supernatant was aspirated and cells were diluted in 5 - 20 mL RPMI 1640 or plating medium. Resuspension volume was adapted according to the amount of cells thawed at once. Then, the CMs were counted again manually in a Neubauer chamber, since cell count might be reduced after freezing and thawing procedure. For monolayer culture of hiPSC-CMs, 12-well or 96-well plates for immunofluorescence were precoated with Geltrex™ (1:100 diluted in RPMI 1640) and incubated at least one hour at 37 °C. Culture plates were prepared with EHT medium (1 mL/12-well; 200 µL/96-well). Seeding densities were 440,000 cells per well in 12-well plates and 2,500 or 5,000 per well in 96-well plates. EHT medium was changed every two until three days, but the day after plating medium was not changed in order to enable the cells to attach. HiPSC-CMs were cultured for one week and usually started beating a few days after thawing.

2.4.2 Inhibition of the nonsense-mediated mRNA decay in hiPSC-CMs

Treatment with drugs inhibiting the NMD (Kosmidis et al., 2016; Vignier et al., 2009) was performed one week after plating in 12-well plates. CMs were thawed and cultured as described in 2.4.1. Before treatment, cells were checked under the microscope for normal beating behaviour and absence of contamination. Incubation time and final drug concentration varied between the substances (Table 12). DMSO was set as the negative control since drugs were dissolved in this substance. Drugs were directly added to the medium of each well.

Table 12: NMD-inhibiting drugs, treatment concentration and incubation time

Substance	Final concentration	Incubation time
Puromycine	300, 600, 900 µg/mL	8 hours
Emetine	300, 600, 900 µg/mL	4 hours
Cycloheximide (CHX)	100 or 300 µg/mL	4 hours
DMSO	0.1%	4 hours

NMD: nonsense-mediated mRNA decay.

After treatment, cardiomyocytes were harvested as described in 2.4.4.

2.4.3 AAV6 transduction of hiPSC-CMs

Gene therapy experiments were performed in either freshly dissociated or thawed hiPSC-CMs using an AAV6 carrying the wild-type *MYBPC3* cDNA sequence under the control of a cardiac troponin T promoter and 5'-tagged with a FLAG sequence. The AAV was kindly produced by Dr. Ingke Braren from the Hext Vector Core Facility (UKE Hamburg). HiPSC-CMs were thawed (cf. 2.4.1). After counting in a Neubauer chamber, cells were centrifuged (100 g, 10 min) and resuspended in EHT medium (e.g. 200 µL per transduction). Cells were separated in two 1.5-mL Eppendorf tubes, one for virus transduction and one for the non-transduced control. As multiplicity of infection (MOI) a value of 10,000 was used as published in Prondzynski et al. (2017). The volume for AAV6 transduction was calculated depending on virus titer according to the formula:

Volume of virus (µL) = Cell number x multiplicity of infection (MOI) x 1,000 / virus titer (vg/mL)

The calculated volume of virus was added to the Eppendorf tube containing the cells for transduction. The tubes containing AAV or not (control) were inverted carefully and incubated at 37 °C for one hour, resuspending the cells every 10 min by inverting several times. After one hour of incubation, hiPSC-CMs were plated as usually on Geltrex™ precoated 12-well plates (440,000 cells per well) and cultured with 1 mL EHT medium per well or on 96-well plates (2500/5000 cells per well) with 200 µL EHT medium per well for immunofluorescence microscopy. After one week of cultivation, CMs were harvested as described in 2.4.4 or fixed for immunofluorescence as reported in 2.4.6.

2.4.4 RNA extraction, cDNA synthesis and PCR

RNA extraction

For RNA extraction, cells were washed once in pre-warmed PBS. Then, 500 µL TRIzol™ Reagent were added per well in 12-well plates (440,000 cells per well), cells were scraped with a cell scraper and resuspended by pipetting up and down. Afterwards, samples were immediately frozen at -80 °C or directly used for extraction of total RNA. RNA extraction was performed using the TRIzol™ Reagent (Life Technologies) according to the manufacturer's protocol. RNA content was determined with the use of the Qubit™ RNA HS Assay Kit (Invitrogen) and the Qubit® 3.0 Fluorometer. In case of high RNA concentrations the content was measured with the Qubit™ RNA BR Assay Kit (Invitrogen) or the

NanoDrop™ ND-1000 Spectrophotometer. Isolated RNA was stored at -80 °C or directly used for cDNA synthesis.

cDNA synthesis

For cDNA synthesis, 200 ng of isolated total RNA were used for transcription. cDNA synthesis was performed using the SuperScript™ III First-Strand Synthesis System for RT-PCR (Invitrogen) and oligo(dT) as described in the protocol of the kit. As control for genomic contamination, an additional reaction without reverse transcriptase (-RT) was run. cDNA was stored at -20 °C or directly used for PCR.

PCR

cDNA analysis was performed by PCR using either the DreamTaq DNA Polymerase with conditions described in Table 4 and Table 5, or the PrimeSTAR® HS DNA Poymerase with conditions described in Table 10 and Table 11. In the mix, 1 µL of cDNA (human tissue: 2 µl of 1:10 dilution) per sample were used. The amplification conditions were adapted to the primers (Table 13) and product length.

Table 13: Primers used on cDNA

Experiment	**Primers (5' → 3')**	**Product size**
Amplification of total *MYBPC3* expression (GT)	F: GCCAGTCTCAGCTTTTAGCAA (*MYBPC3,* exon 1) R: CAGGCCGTACTTGTTGCTG (*MYBPC3,* exon 2)	151 bp
Amplification of FLAG-*MYBPC3* expression	F: GGATTACAAGGATGACGACGA (FLAG) R: CAGGCCGTACTTGTTGCTG (*MYBPC3*, exon 2)	193 bp
GAPDH (housekeeping)	F: ATGTTCGTCATGGGTGTGAA (*GAPDH,* exon 5) R: TGAGTCCTTCCACGATACCA (*GAPDH,* exon 6)	136 bp
NMD-inhibition (PCR#1)	F: TGTCAGCCAAGCTCCACTTC (*MYBPC3,* exon 19) R: TCGATGTGTGCTCTGTCAGC (*MYBPC3,* exon 27)	912 bp
Human tissue; NMD-inhibition (PCR#2/3)	F: TGTCAGCCAAGCTCCACTTC (*MYBPC3,* exon 19) R: AGGCGGCTCCCACTGTACT (*MYBPC3,* exon 24)	512 bp

F: forward; GT: gene therapy; NMD: nonsense-mediated mRNA decay; R: reverse.

Subcloning

For subcloning of PCR fragments (NMD-inhibition experiment) into *E.coli*, a PrimeSTAR® PCR was performed as described in Table 10 and Table 11. One µL cDNA was used and PCR conditions were adapted to the primers of this experiment (primers of NMD-inhibition PCR#2/3; 45-sec elongation time; touchdown *65-60). The further cloning procedure, ligation, transformation etc. were the same as described in 2.2.5.

Sequencing

For sequence analysis, PCR fragments were detected on agarose gels (1-2%), purified and sent to Eurofins genomics for sequencing as described in 2.2.3, 2.2.4 and 2.2.5.

RNA analysis by NanoString

Extraction of RNA from human tissues and NanoString runs were kindly performed by Elisabeth Krämer and Dr. Maksymilian Prondzynski. Data were analysed by Dr. Giulia Mearini.

2.4.5 Western blot

For Western blot analysis, hiPSC-CMs were cultured as described in 2.4.1. After seven days, cells were washed once in pre-warmed PBS. Then, 500 µL Kranias buffer (30 mM Tris pH 8.8, 5 mM EDTA, 30 mM NaF, 3% SDS, 10% glycerol) were added per 12-well (440,000 cells per well) and cells were scraped and resuspended. Afterwards, samples were frozen at -20 °C or directly used for Western blot. To determine protein concentrations, the Qubit™ Protein Assay Kit (Invitrogen) and the Qubit® 3.0 Fluorometer were used according to the instructor's protocol. Separation of protein bands was performed by SDS-PAGE (sodium dodecyl sulfate polyacrylamide) gel electrophoresis. DTT was added 1:1,000 to the protein samples. Samples were mixed 1:6 with 6x Laemmli buffer (60 mM Tris-HCl pH 6.8, 600 mM DTT, 12% SDS, 0.06% bromophenol blue, 60% glycerol) to a final volume of 18 µL. For denaturation of proteins, the samples were boiled for 5 min at 95 °C in a heat block. For separation, a 10% polyacrylamide gel was prepared. Polyacrylamide gels contained an upper stacking gel (5.1% acrylamide/bis solution (29:1), 125 mM Tris-base pH 6.8, 0.1% SDS, 0.1% ammonium persulfate (APS), 0.1% tetramethylethylenediamine (TEMED), aqua dest. to 10 mL) and a separating gel (10% acrylamide/bis solution (29:1), 375 mM Tris-base pH 8.8, 0.1% SDS, 0.1% APS, 0.04% TEMED, aqua dest. to 10 mL). After polymerisation of both gels, they were placed in an electrophoresis chamber (Mini-Protean®3, Bio-Rad) containing 1x electrophoresis buffer (25 mM Tris-base, 192 mM Glycine, 0.1% SDS, aqua dest. until final volume). Samples

(18 µL/lane) were loaded with the marker Precision Plus Protein™ Dual Color Standard (Bio-Rad) (5 µL/lane). Gels were run at 80 V for 10 min and then at 150 V for at least 90 min. For protein transfer a blot set-up was prepared. Therefore, gels were placed on a nitrocellulose (NC) membrane in a blotting chamber containing blotting buffer (50 mM Tris base, 380 mM glycine, 0.1% SDS, 20% methanol, aqua dest. until final volume). Wet-electroblotting was performed for 70 min at 300 mA on ice. Correct transfer was verified by Ponceau S (Merck) staining. Bands were detected in the ChemiDoc™ Touch Imaging System (Bio-Rad) using the colorimetric set-up. After 3 x 5 min wash in 1x TBS-Tween 0.1% solution (100 mM Tris base pH 7.5, 150 mM NaCl, 0.1% Tween 20, aqua dest. until final volume) membrane was blocked in blocking buffer (5% milk powder in 1 x TBS-Tween 0.1%) for one hour at RT. After washing 3 x 5 min in 1x TBS-Tween 0.1% solution, primary antibody staining was performed over night at 4°C under gentle agitation. Primary antibodies (Table 14 and Table 15) were diluted in 1 x TBS-Tween 0.1%. The next day, membranes were washed 3 x 5 min in 1x TBS-Tween 0.1% solution and subsequently stained for the secondary antibodies in blocking buffer at RT for one hour under gentle agitation. Finally, membranes were washed again as described before. For detection, the Clarity™ ECL Western Substrate (Bio-Rad) was used according to the protocol of the kit. Bands were detected with the ChemiDoc™ Touch Imaging System (Bio-Rad) using the chemiluminescent set-up. Results were analysed and bands were quantified using the Image Lab software (Bio-Rad).

Table 14: Primary antibodies used for Western blots

Primary antibodies	**Dilution**	**Manufacturer**
Anti-cMyBP-C, F1 (mouse)	1:2,000	Santa Cruz
Anti-cTnT (mouse)	1:3,000	Abcam
Anti-FLAG (mouse)	1:5,000	Sigma

Table 15: Secondary antibodies used for Western blots

Secondary antibodies	**Dilution**	**Manufacturer**
Anti-mouse IgG	1:10,000	Dianova
Anti-mouse IgG	1:10,000	Sigma

2.4.6 Immunofluorescence

For immunofluorescence staining, CMs were plated on 96-well plates and cultured as described previously. After seven days, cells were washed once in 1 x PBS and fixed with

50 µl/96-well Histofix® for 20 min at 4 °C according to Prondzynski et al. (2017). After washing twice in 1 x PBS, primary antibodies were added (50 µl/96-well, listed in Table 16 and Table 17). Primary antibody staining was performed over night at 4 °C shaking gently. Antibodies were diluted in freshly made permeabilisation buffer containing 1 x PBS, 3% milk powder and 0.1% Triton™ X-100. The next day, secondary antibody staining was performed after washing twice in 1 x PBS and incubated under light protection for two hours at RT shaking gently (50 µl/96-well). Finally, Hoechst 33342 as nuclear staining was added to the wells (50 µl/96-well) and incubation time was prolonged for another 30 – 40 min. Eventually, wells were washed twice in 1 x PBS. Immunofluorescence plates were stored at 4 °C containing 200 µL fresh PBS per well in 96-well plates or used directly for subsequent confocal microscopy using the Zeiss LSM 800 microscope.

Table 16: Primary antibodies used for immunofluorescence staining

Primary antibodies	**Dilution**	**Manufacturer**
Anti-cMyBP-C, C5 domain (rabbit)	1:200	Kind gift from Andreas Unger
Anti-FLAG (rabbit)	1:800	Sigma
Anti-FLAG (mouse)	1:800	Sigma
Anti-α-actinin 2 (mouse)	1:800	Sigma
Hoechst 33342	1:2,000	Thermo Fisher Scientific

Table 17: Secondary antibodies used for immunofluorescence staining

Secondary antibodies	**Dilution**	**Manufacturer**
Anti-mouse IgG Alexa Fluor 488	1:800	Life Technologies
Anti-rabbit IgG Alexa Fluor 546	1:800	Life Technologies

For measurement of cell size of hiPSC-CMs, immunofluorescence images with single cells were used. Only cells that had defined sarcomeric structure were included into analysis. Measurements were performed with the Fiji software based on ImageJ. Cell sizes of >20,000 µm² were excluded assuming artefacts during fixation.

2.5 Engineered heart tissues

2.5.1 Generation of human EHTs

Three-dimensional EHTs were generated as previously described (Breckwoldt et al., 2017). HiPSC-CMs were thawed as described in 2.4.1. After thawing, cells were counted manually

in a Neubauer chamber. Volumes of *non cardiac myocyte medium* (NKM) for resuspension were calculated according to cell count and desired number of EHTs. One million hiPSC-CMs were used per EHT. The procedure of EHT generation is depicted in Figure 7. After resuspension of CMs in NKM, CMs were kept on ice until final use. In the meantime, molds in 2% agarose (2% in PBS) were casted in 24-well plates (1.5 mL/well) using specific Teflon spacers. Agarose was solid after approximately 20 min and spacers were carefully removed. Then, polydimethylsiloxane (PDMS) posts were placed into the agarose molds. Finally, the mastermix was prepared including calculated volumes of hiPSC-CMs in NKM solution, 2x DMEM, Matrigel®, Y-27632 and fibrinogen (pre-warmed by hand) according to Table 18. The mastermix was mixed thoroughly but gentle. Directly before casting, 100 µL of the mastermix were mixed with 3 µL thrombin (thrombin aliquots were prepared beforehand) and immediately added into each well. Creation of air bubbles was avoided whilst pipetting into the molds. Then, EHTs were incubated for 1.5 - 2 h at 37 °C and hyperoxia (7% CO_2, 40% O_2 and 98% humidity). Afterwards, each well was covered with 500 µL medium and placed again in the incubator for another 20 min. In the meantime, a new 24-well plate was prepared with fresh EHT medium (1.5 mL/well). After incubation time, the PDMS racks with casted EHTs were carefully removed from the molds and EHTs were transferred into the new medium plate. Casted EHTs were cultured under the mentioned conditions and media was changed in a schedule of every two to three days.

Table 18: Mastermix for generation of human EHTs

Mastermix	**1 EHT (including 10% extra)**
2x DMEM	6.13 µL
10% Matrigel®	11 µL
0.1% Y-27632	0.11 µL
Fibrinogen	2.78 µL
NKM with resuspended hiPSC-CMs	86.69 µL
Thrombin	3 µL

2.5.2 Functional analysis

Analysis of beating EHTs was performed in a video-optical measurement system (“Whitebox”) that was developed in the institute as previously described (Hansen et al., 2010; Mannhardt et al., 2017). Cracked EHTs and EHTs that did not follow the pacing - in case pacing electrodes were used - were excluded from the analysis.

Baseline measurement

Baseline measurements were performed two hours after medium change under spontaneous beating starting from day seven. The video-optical system was able to measure force (mN), frequency (bpm), contraction time ($T1_{20\%}$) and relaxation time ($T2_{20\%}$), automatically. Measurement times were 10 s per EHT and as force threshold a value of 0.02 mN was set. For detailed description of contraction measurements see also Mannhardt et al. (2017).

Calcium overnight

Calcium overnight measurements were performed under spontaneous beating in modified tyrode's solution (120 mM NaCl, 5.4 mM KCl, 1 mM $MgCl_2$, 3 mM $CaCl_2$, 0.4 mM NaH_2PO_4, 22.6 mM $NaHCO_3$, 5 mM glucose, 0.05 mM Na_2EDTA, and 25 mM HEPES) containing 2 mL/well in 24-well plates of 3 mM [Ca^{2+}]. EHTs were transferred into the tyrode plate and measurements were done over 16 h (usually over night) in which measurements were performed each hour for 50 s. The first measurement was excluded due to lack of incubation time to the high [Ca^{2+}]. In addition to the mentioned parameters, the RR scatter was used for analysis as an indicator for arrhythmic beating behaviour (parameter of irregularity between contraction peaks). The next day, EHTs were washed in old medium and then transferred to a freshly prepared plate containing normal EHT medium. EHTs were not used within the next two days in order to allow regeneration.

Calcium sensitivity

To evaluate forces in response to different external [Ca^{2+}], plates containing different [Ca^{2+}] (0 mM, 0.4 mM and 2 x 0.3 mM, 1.8 mM) in tyrode's solution were prepared (2 mL/well) at least one day before the experiment and incubated at 37 °C, 7% CO_2, 40% O_2 and 98% humidity. This experiment was performed under electrical pacing using carbon electrodes to implement more stable and equal conditions. Pacing electrodes were specifically adapted to the 24-well format of the EHTs as described in Hirt et al. (2014). Baseline was measured after 30 min incubation in tyrode solution with 1.8 mM [Ca^{2+}] under spontaneous beating (50 s) and under pacing at different frequencies (e.g. 1.0 Hz, 1.5 Hz, 2.0 Hz and 2.5 Hz) for 10 s. Afterwards, EHTs were incubated under pacing in 0.3 mM [Ca^{2+}] to adapt to low calcium conditions. Then, the experiment was started, measuring EHTs under pacing increasing the [Ca^{2+}] stepwise (0.3 mM, 0.4 mM, 0.5 mM, 0.6 mM, 0.7 mM, 0.8 mM, 0.9 mM, 1.0 mM, 1.2 mM, 1.4 mM, 1.8 mM, 2.4 mM, 3.3 mM, 5.0 mM and 10 mM). Calcium concentrations were increased pipetting the calculated amount of calcium from a calcium stock (20 or 200 mM $CaCl_2$ diluted in sterile water). Between each change in calcium concentration, EHTs were incubated for at least 15 min to adapt to the new conditions they

were exposed to. Pacing frequencies were individually determined per cell line making sure EHTs could follow the given pacing frequency and did neither contract slower nor faster than their spontaneous beating activity. Contraction parameters were compared within one pacing frequency and to its baseline in 1.8 mM [Ca^{2+}] tyrode. After the experiments, EHTs were washed in 1.8 mM [Ca^{2+}] tyrode and then transferred into a new medium plate. EHTs were not used within the next two days to allow regeneration. EC_{50} values were determined for further experiments and EHTs weren't used within the next two days.

Isoprenaline-carbachol experiment

For this experiment, three plates of tyrode's solution were prepared, one containing 1.8 mM [Ca^{2+}] and the others with concentrations of the calculated EC_{50} values (2 mL/well). Both drugs were freshly prepared and sterile filtered. The isoprenaline stock was 10 µM and carbachol 1 mM in tyrode's solution. Baseline was measured at 1.8 mM [Ca^{2+}] tyrode under pacing (10 s) and spontaneous beating (50 s) as described above. Then, EHTs were transferred to the first EC_{50}-plate for adaptation and incubated under pacing for at least 20 min. Afterwards, they were placed in the second EC_{50}-plate (incubation time at least 20 min) and isoprenaline was added to each well to a final concentration of 100 nM. Measurements were performed immediately with and without pacing. Finally, carbachol was added on top of each well (final concentration 10 µM). Measurements were done directly afterwards. After washing EHTs in 1.8 mM [Ca^{2+}] tyrode and transferring them to fresh EHT medium, they weren't used within the next two days.

Force-Frequency-Relationship

For the experiment analysing the relationship between force and frequency, tyrode plates were prepared as done for the isoprenaline-carbachol experiment and baseline measurements were performed as described. After washing in the first EC_{50}-plate, EHTs were exposed to different pacing frequencies in the second EC_{50}-plate. Pacing frequencies were 0.25 Hz, 0.5 Hz, 0.75 Hz, 1.0 Hz, 1.25 Hz, 1.5 Hz, 1.75 Hz, 2.0 Hz, 2.25 Hz, 2.5 Hz, 3.0 Hz, 3.5 Hz and 4.0 Hz until none of the EHTs was pacable anymore.

2.5.3 Harvesting of EHTs

After finishing all functional experiments, EHTs were washed in PBS, harvested carefully with a pair of tweezers in 2-mL Eppendorf tubes and snap frozen in liquid nitrogen. EHTs were stored at -80 °C.

3 Results

3.1 Molecular analysis of patient-specific mutation in *MYBPC3*

The location of the mutation of the index patient on the last nucleotide of exon 23 of *MYBPC3* suggests possible alteration of splicing (skipping of the exon) since the involved nucleotide is part of the highly conserved 5' splice donor site sequence. Consequently, skipping of the 160-bp-long exon 23 would lead to a disruption of the reading frame and would be considered as a frameshift mutation with a subsequent PTC. Hence, the mechanism of the mutation was investigated. Therefore, a PCR with primers around exon 23 was performed with cDNA obtained from the septal myectomy of the index patient and septum from a non-failing heart. PCR amplification products were run on agarose gel. Unexpectedly, solely a band of wild-type size (512 bp, Figure 14A) was revealed. No band of smaller size suggesting skipping was detected. The sequencing of this band exclusively revealed the wild-type G at the junction site of exon 23 and exon 24, indicating that the G>A transition of the index patient is not a missense variant, but leads to a truncating transcript that is degraded by the cell (Figure 14B). Interestingly, a slight band was visible above the wild-type band in the HCM sample, which was not present in the control sample.

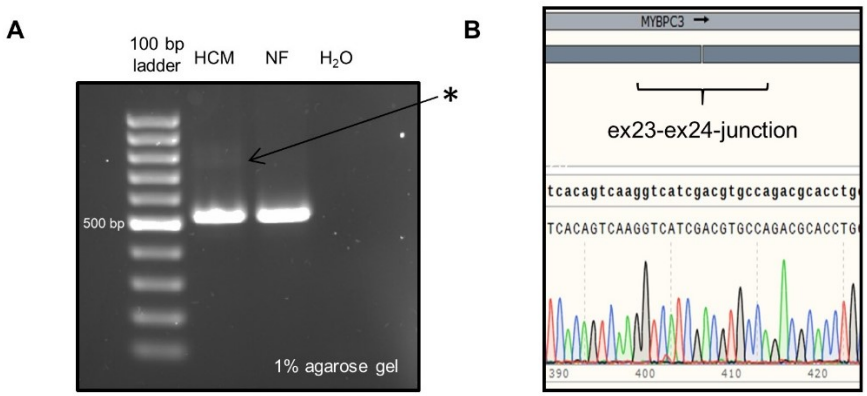

Figure 14: Analysis on patient-derived septal tissue
A *cDNA analysis by PCR in comparison to tissue from a non-failing heart. Fragment size of the wild-type is 512 bp. Note the slight band of bigger size in the HCM sample marked with a *.* ***B*** *Sequencing of cDNA of the myectomy sample solely revealed the expression of the wild-type allele indicating a degradation of the nonsense transcript(s). ex: exon; HCM: patient's tissue; NF: non-failing heart.*

RNA analysis with the NanoString technology showed reduced *MYBPC3* mRNA level (72.5%) compared to a pool of non-failing hearts (Figure 15), also suggesting degradation of the transcript from the mutant allele.

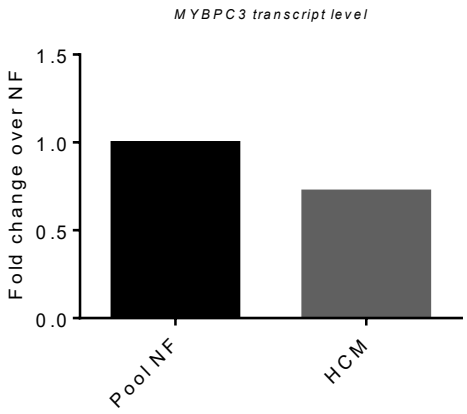

Figure 15: MYBPC3 expression analysis (NanoString)
Comparison of MYBPC3 transcript levels in the patient's myectomy sample (n=1) and non-failing hearts (n=9, pooled RNA). HCM: index patient's tissue; NF: non-failing heart.

Further efforts were invested in order to detect the mutant transcript and to clarify the mechanism by which the mutation leads to the degradation of its transcript. Therefore, the hiPSCs from the index patient (CMS32) were differentiated into CMs (cf. 3.4) to be able to treat the CMs *in vitro* with drugs known to inhibit the NMD as previously described (Kosmidis et al., 2016; Vignier et al., 2009). After cardiac differentiation, hiPSC-CMs were treated with puromycine and emetine after six days of culture in a monolayer (2D). Then, total RNA was extracted and reverse transcribed into cDNA, and two different amplification strategies, one long amplification strategy (PCR#1, Figure 16) and one short amplification strategy (PCR#2, Figure 17A-B), were performed.

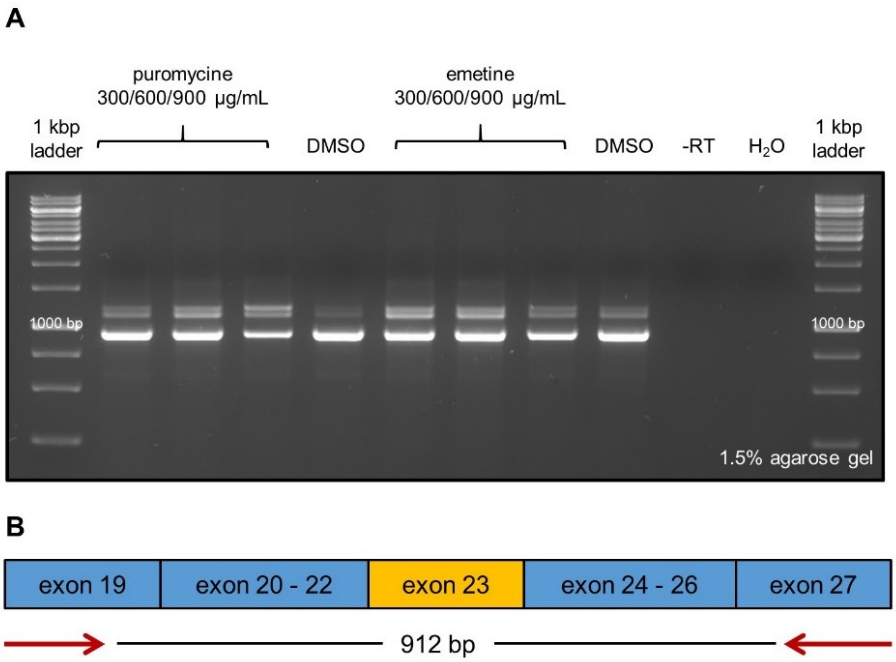

Figure 16: Inhibition of the nonsense-mediated mRNA decay (PCR#1)
A *cDNA analysis of hiPSC-CMs treated with puromycine (8 h) or emetine (4 h) in different concentrations after six days of culture (2D).* ***B*** *Long amplification strategy to detect the nonsense transcript(s). Wild-type fragment size is 912 bp. Primers are indicated in red. RT: reverse transcriptase.*

In PCR#2 the same primers as for analysis of septal myectomy were used. Treatment with DMSO was used as negative control since the NMD-inhibiting drugs were dissolved in DMSO and a sample without reverse transcriptase (-RT) served to exclude genomic contamination of the cDNA. After amplification and loading on agarose gel, the wild-type fragment (912 bp in PCR#1 and 512 bp in PCR#2) was detected in both amplification strategies as well as two additional bands larger in size, which were stabilised after treatment. These two upper bands were estimatedly 200 – 300 additional bp larger than the wild-type size and were less prominent in the DMSO sample. To validate that these additional bands were not due to the drug treatment itself, but were potentially the mutant transcripts, another PCR was performed (PCR#3, Supplement Figure 50). Therefore, NMD-treated CMS32-CMs were compared to NMD-treated CMs from another hiPSC line (CMS10), carrying a different *MYBPC3* mutation. In CMS10-CMs, the PCR did not show these additional bands but only the wild-type band hinting at specific amplification products for this mutation in CMS32-CMs.

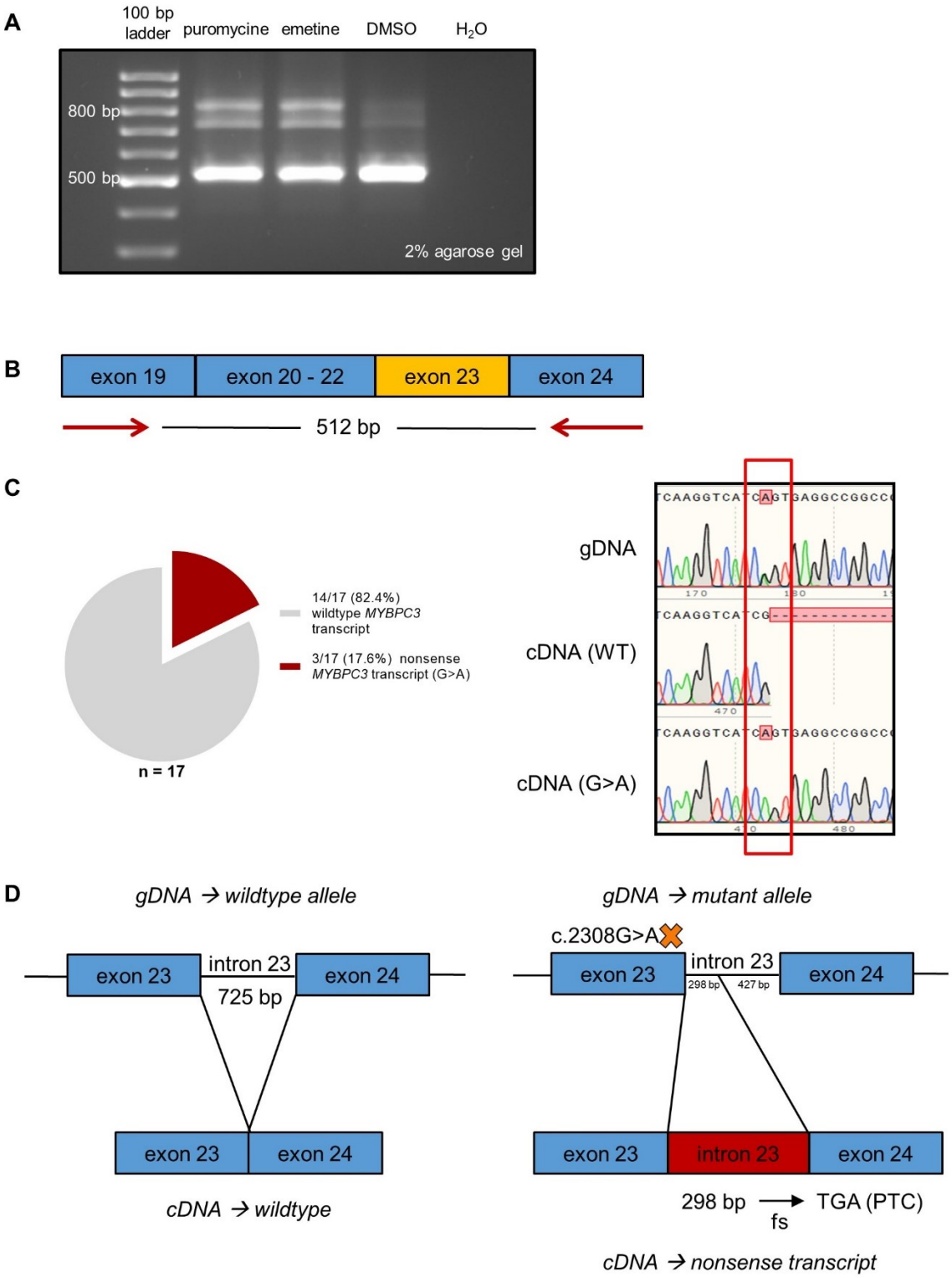

Figure 17: Inhibition of the nonsense-mediated mRNA decay (PCR#2)
A *cDNA analysis of hiPSC-CMs treated with puromycine (600 µg/mL, 8 h) or emetine (600 µg/mL, 4 h) after six days of culture (2D).* ***B*** *Short amplification strategy to detect the nonsense transcript(s). Wild-type fragment size is 512 bp. Primers' location is indicated in red.* ***C*** *Sequencing results after subcloning of amplified cDNA fragments into E.coli.* ***D*** *Schematic analysis of wild-type and nonsense transcripts after subcloning. The G>A transition leads to retention of 298 bp of intron 23 in the transcript. fs: frameshift; PTC: premature termination codon; WT: wild-type.*

In order to affirm the detection of the nonsense transcripts, the PCR fragments (PCR#2) were subcloned into *E.coli* after column purification and 17 clones were analysed.

Sequencing reaveled in 14/17 (82.4%) of the clones the wild-type *MYBPC3* transcript and in 3/17 (17.6%) of the clones the G>A transition indicating the mutant transcript (Figure 17C). Further analysis by aligning the sequences to the reference genomic sequence of *MYBPC3* (NC_000011.10, NCBI) showed correct splicing (expected junction exon23-exon24) of the wild-type transcript, but in the case of the 3 clones carrying the mutant transcript, the junction was disrupted by partial retention of intron 23 (298 bp out of 725 bp). Moreover, *in silico* analysis using the Open Reading Frame Finder (NCBI) showed a shift of the reading frame and a PTC in exon 24 after creation of 98 new amino acids on protein level (Asp770Serfs98X). Although the 298-bp retention only explains the upper of the two additional bands detected by PCR, sequencing of the lower did not properly work neither by gel extraction nor by increasing number of picked clones (data not shown).

3.2 Genome editing by CRISPR/Cas9

For the creation of a human cellular model for severe cardiomyopathy the CRISPR/Cas9 genome editing was used in order to obtain three hiPSC lines with the same genetic background as one was derived from the index patient and the others were genetically modified and exclusively different in the mutations of interest in *MYBPC3*.

In silico predicted binding of designed gRNAs and alignment of corresponding templates are shown in Figure 18 and Figure 19. In both templates, silent mutations close to the target site were included to prove use of the template when analysing genome editing efficiency. To prevent cleavage of the template one nucleotide in the PAM sequence of the repair template was changed, whereas this was not necessary for the mutant approach since the desired point mutation already altered the PAM sequence.

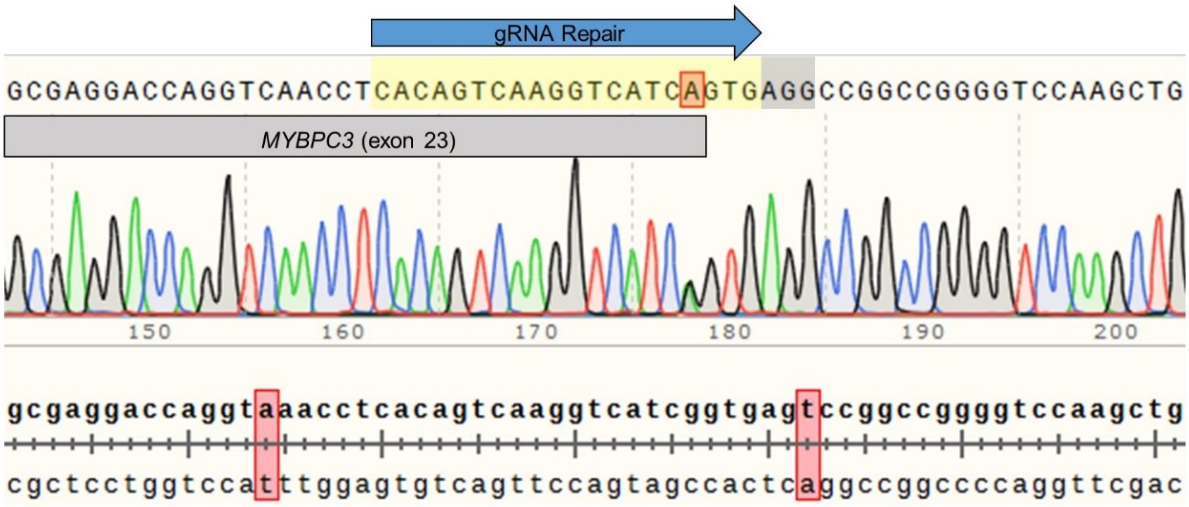

Figure 18: Locus of the patient's mutation in MYBPC3 (c.2308G>A) and strategy for creation of an isogenic control

Design of gRNA and the repair template with exchange of two nucleotides (one silent and one intronic) aligned to the target site. Predicted binding of the gRNA is highlighted in yellow. NGG PAM is highlighted in grey. Silent mutation is GTC (WT) → GTA (silent mutation) → Val762. gRNA: guide RNA; PAM: protospacer adjacent motif.

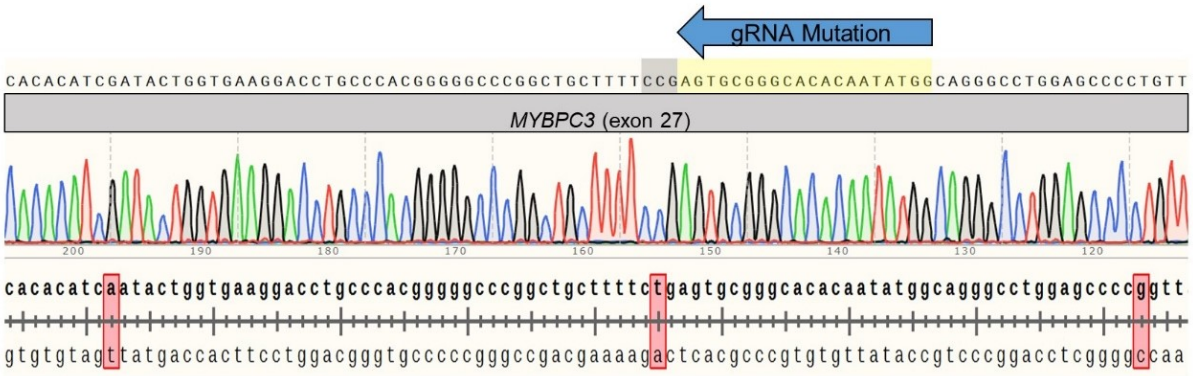

Figure 19: Locus of exon 27

Design of the gRNA and mutation template with the point mutation (c.2827C>T, middle red box) of interest together with two silent mutations aligned to the target site. Predicted binding of the gRNA is highlighted in yellow. NGG PAM is highlighted in grey (antisense direction of gRNA + PAM). Only the sequence of the top DNA strand is inscribed although gRNA binding will happen on the bottom strand. gRNA: guide RNA; PAM: protospacer adjacent motif.

After design of the two CRISPR approaches (cf. 2.2.1), CRISPR Repair for the isogenic control and CRISPR Mutation for the bi-allelic mutant (Figure 20A&B left), nucleofection was performed. Forty-eight hours after nucleofection, hiPSCs were checked under the fluorescence microscope (RFP channel) for efficient nucleoporation as this was recommended by IDT®. Despite a high background fluorescence, there were at least a couple of cells showing red fluorescence signal (Figure 20A&B middle). Nine days after single-cell seeding of nucleofected cells, several colonies were sufficient in size for picking. Representative pictures of these can be seen in Figure 20A&B (right), one example for each approach. 42 clones for the Repair approach were picked, whereas for the Mutation approach 120 clones were picked in total.

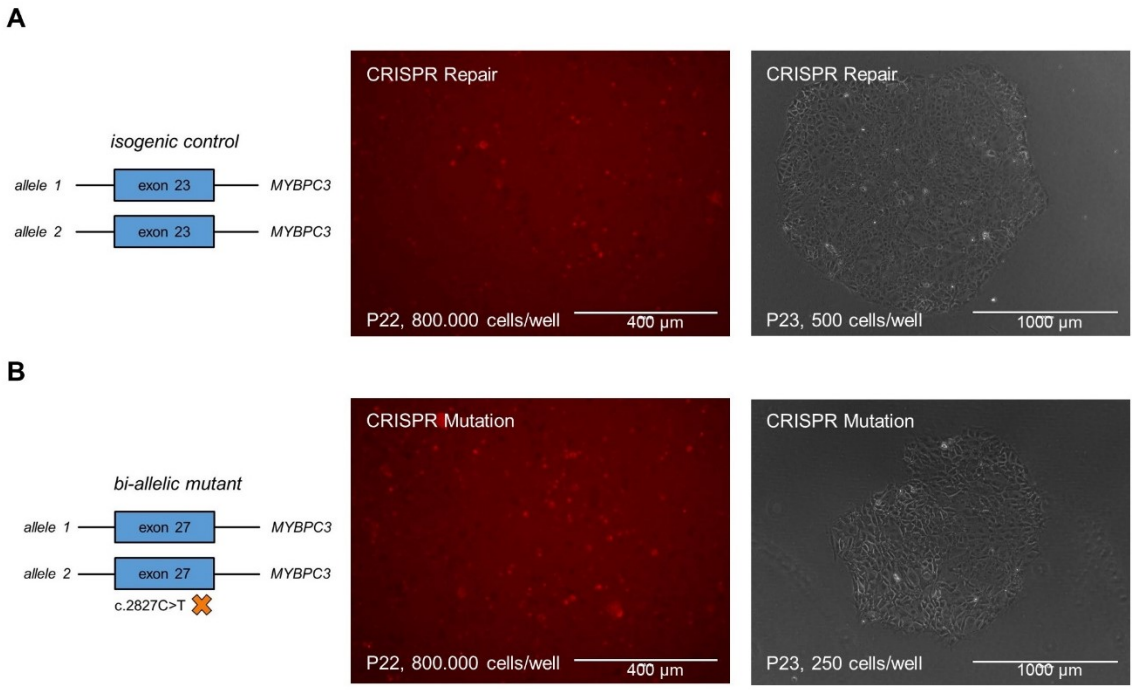

Figure 20: Representative pictures of CMS32-hiPSCs after nucleofection
A *Scheme of CRISPR Repair (left). Forty-eight hours after nucleofection: hiPSCs showed red fluorescent protein indicating successful delivery of RNP complex and Cas9 after electroporation (middle). Nine days after single-cell seeding: Colonies were sufficient in size for picking (right).* ***B*** *Scheme of CRISPR Mutation (left). Forty-eight hours after nucleofection: hiPSCs showed red fluorescent protein indicating successful delivery of RNP complex and Cas9 after electroporation (middle). Nine days after single-cell seeding: Colonies were sufficient in size for picking (right). P: Passage; RNP: ribonucleoprotein.*

3.2.1 Creation of an isogenic control hiPSC line

After culture and expansion of all picked clones, one 48-well was harvested as a back-up cryo in case of positive genotype and another 48-well was used for DNA extraction as described in 2.2.3. After PCR amplification, the amplicons were detected on an agarose gel. Figure 21A shows 18 representative clones for the CRISPR Repair approach.

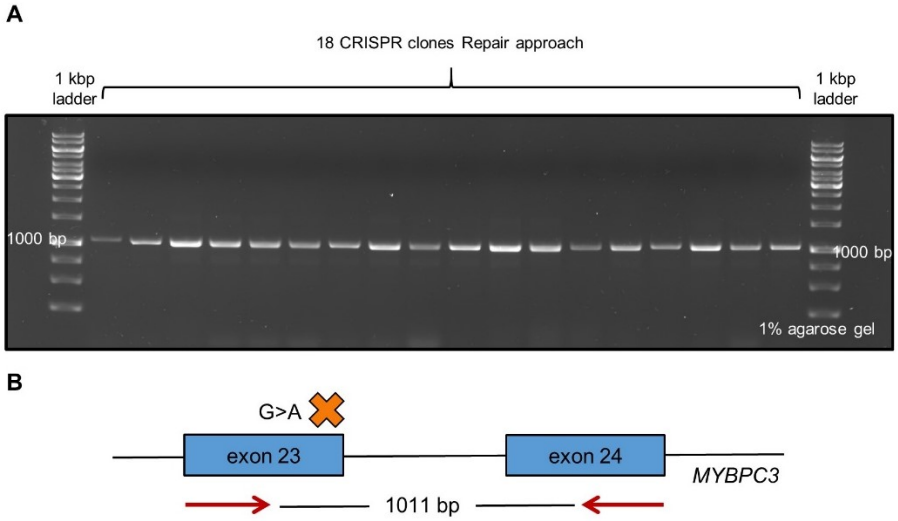

Figure 21: CRISPR Repair PCR
A *Amplification of CRISPR Repair analysis for 18 representative clones visualised by agarose gel electrophoresis. Fragment size is 1011 bp.* ***B*** *Schematic depiction of primers and amplification region. Primers are indicated in red. Forward primer in exon 23 is located >200 bp upstream of the locus of the mutation.*

Importantly, larger deletions or insertions within the amplification size would have been visible in this PCR. As no second band was visible for none of the clones and the amplification strategy spanned a large fragment (1011 bp), the occurrence of big indels seemed unlikely here (Figure 21B). However for one clone (Rep#36), the PCR did not show any band at all. This clone was excluded from further analysis. It remains unclear, whether the failed amplification was due to a technical problem or if a deletion occurred in this specific clone as samples weren't checked for *GAPDH*. Eventually, 41 out of 42 picked clones were subsequently sequenced.

Analysis of the 41 clones after sequencing revealed that Cas9 activity was high with a percentage of 90.2% (37/41) as calculated by the ratio of all clones edited either by HDR or by NHEJ compared to the total of 41 analysed clones (Figure 22A). The majority of clones (31/41=75.6%) was NHEJ-edited, as shown by the presence of indels after alignment to wild-type sequence. Only 4/41 clones (9.8%) still carried the heterozygous G>A transition in exon 23 and remained unedited. Fortunately, the amount of HDR-repaired clones was 6/41 (14.6%), which proved high fidelity of the gRNA chosen for this approach. Representative peaks are shown for clone Rep#12 and Rep#28 compared to CMS32 (Figure 22B). Mark as well that clone Rep#28 incorporated one of the two silent mutations of the repair template into its genome. For sequences of clones Rep#11 and Rep#20 see Supplement Figure 51.

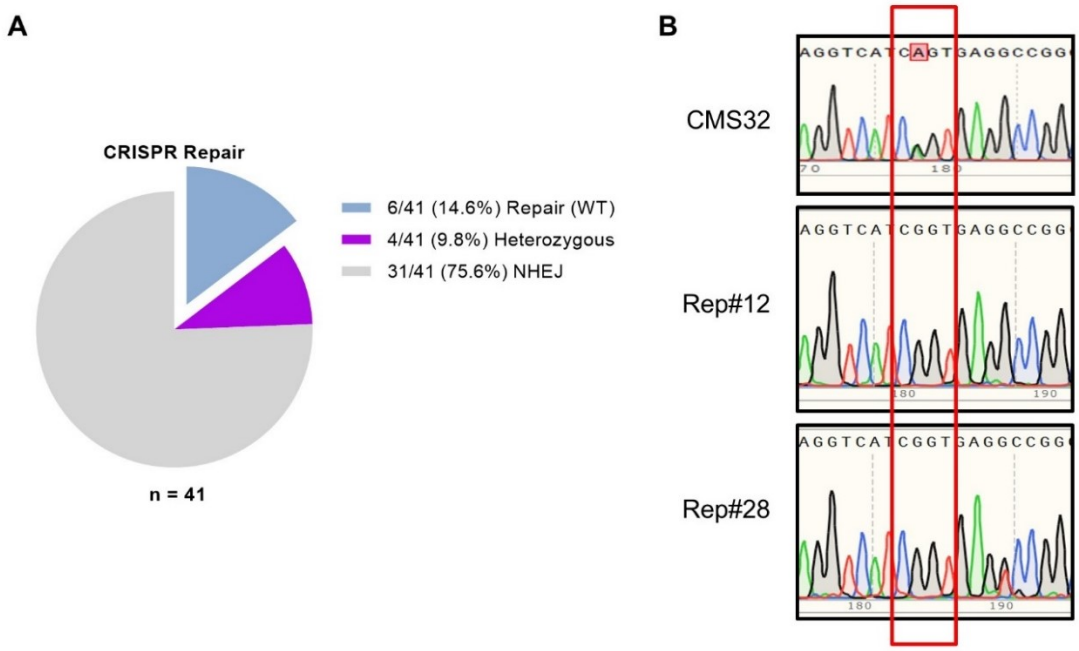

Figure 22: CRISPR Repair sequencing results
A *A total of 41 clones was analysed. Cas9 activity was 90.2% as calculated by percentage of NHEJ- and HDR-repaired clones out of the total number of clones.* ***B*** *Sequences of two representative HDR-repaired clones (Rep#12 and Rep#28) in comparison to CMS32. Mark as well the presence of the silent mutation in Rep#28. HDR: homology-directed repair; NHEJ: nonhomologous end joining; WT: wild-type.*

3.2.2 Creation of a bi-allelic *MYBPC3* mutant hiPSC line

As it was done for the clones of the CRISPR Repair approach, one 48-well was cryo-preserved for clonal expansion and another 48-well was used for genotyping (cf. 2.2.3). Agarose gel electrophoresis after PCR amplification of 12 representative clones for the CRISPR Mutation approach is shown in Figure 23. Fragment size was 247 bp here, as primers for longer amplification sizes were difficult to design. Therefore, larger deletions would not be detected with this strategy.

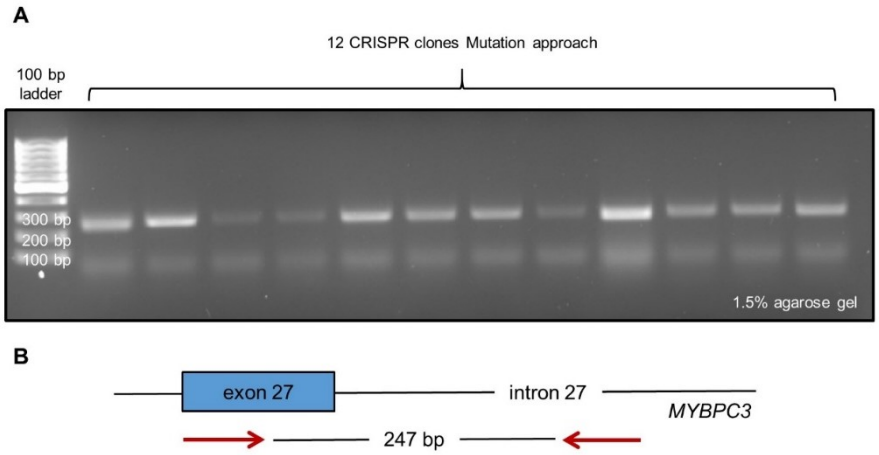

Figure 23: CRISPR Mutation PCR
A *Amplification of CRISPR Mutation analysis for 12 representative clones visualised by agarose gel electrophoresis. Fragment size is 247 bp.* ***B*** *Schematic depiction of primers and amplification region. Primers are indicated in red.*

Since some clones did not grow after picking and some errors in PCR for unknown reasons, only 93 of the 120 picked clones were fully analysed. Sequencing results (Figure 24A) revealed a high Cas9 activity of 90.3% (84/93). The number of unedited clones still carrying the wild-type nucleotide was 9 out of 93 (9.7%), the number of NHEJ-repaired clones was 78/93 (83.9%). However, to the major interest, sequencing also revealed 3/93 (3.2%) heterozygous clones and 3/93 homozygous (3.2%) clones for the mutation of interest. Representative peaks of one heterozygous clone (Mut#6) and one homozygous clone (Mut#103) are shown in Figure 24B.

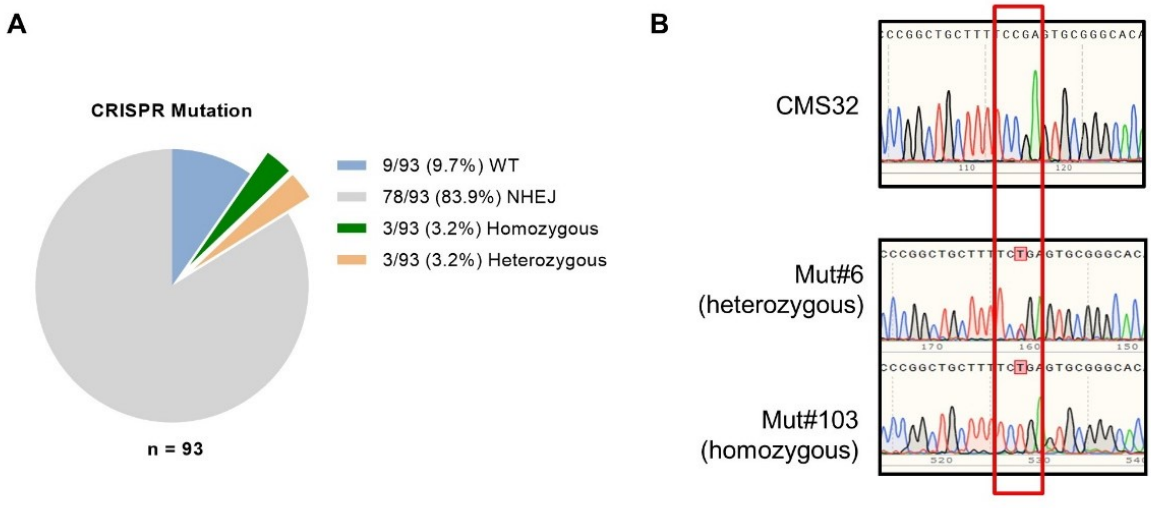

Figure 24: CRISPR Mutation sequencing results
A *A total of 93 clones was analysed. Cas9 activity was 90.3% as calculated by percentage of NHEJ- and HDR-repaired clones versus the total of clones.* ***B*** *Sequences of two representative HDR-repaired clones (Mut#6 and Mut#103) in comparison to CMS32. HDR: homology-directed repair; NHEJ: nonhomologous end joining; WT: wild-type.*

Due to unknown reasons subcloning of the heterozygous clones did not clarify the allelic distribution of this mutation in comparison to the patient's mutation (data not shown). A possible explanation is that either these were mosaic clones or the distance between the two mutations (exon 23 and exon 27), which needed to be amplified by PCR as one fragment for subcloning in order to validate the allelic distribution, was too long with 3794 bp, which made it technically difficult. Therefore, we focused on the homozygous mutant clone Mut#103, since it would functionally serve as a compound heterozygous clone due to presence of the heterozygous mutation in exon 23 and the second homozygous mutation in exon 27.

3.2.3 Off-targets analysis

The off-target analysis for the CRISPR Repair approach was performed for the top 10 most likely off-target regions (Table 6) as described in 2.2.4. After PCR amplification as shown in Figure 25A for clone Rep#20, all sequences were aligned to wild-type sequences provided from NCBI. Figure 25B summarises the alignment of all ten off-target loci for clone Rep#20 and demonstrates the absence of any off-target effects in these analysed loci. Off-target analysis for the isogenic controls Rep#11, Rep#12 and Rep#28 is shown in the supplement (Figure 52).

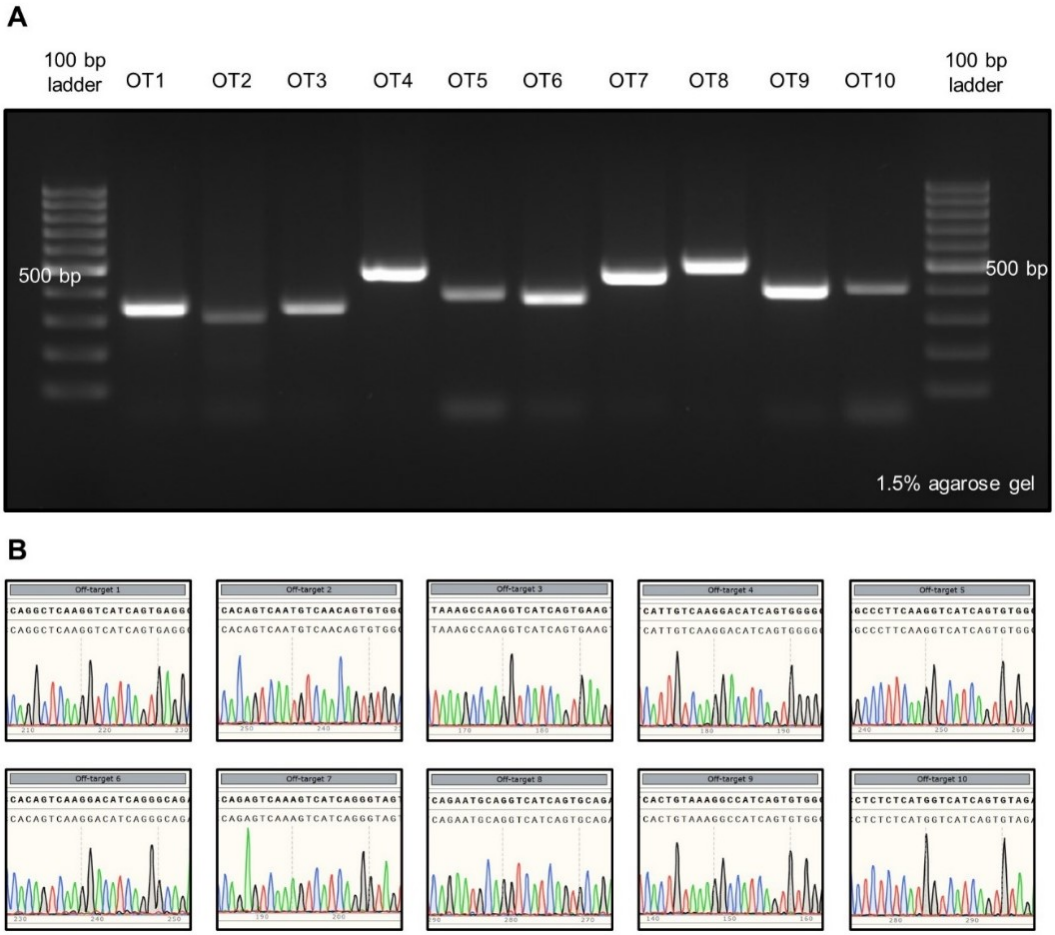

Figure 25: Off-target analysis CRISPR Repair
A *Representative example of an agarose gel showing the PCR amplification of the top 10 off-target regions of clone Rep#20.* ***B*** *Off-target sequences of Rep#20 aligned to wild-type showing no off-target effects. OT: off-target.*

The occurrence of off-targets was only excluded for these four isogenic controls (Rep#11, Rep#12, Rep#20 and Rep#28) since the residual two isogenic controls, that were identified after CRISPR analysis, were not expanded to a MCB and therefore not used for further experiments.

As for the isogenic controls, off-targets were also analysed for the bi-allelic mutant clone Mut#103. Here, the most likely off-target loci were determined for the gRNA of the CRISPR Mutation approach (cf. 2.2.4, Table 7). PCR amplification for this approach is shown in Figure 26A&B. Sanger sequences for Mut#103 were aligned in the same way as done for the isogenic controls (Figure 26C). Importantly, off-target effects could be excluded in these ten potential regions. Off-targets were not analysed for clone Mut#6 since allelic distribution of the heterozygous mutation in exon 27 remained unclear and no further experiments were done with this clone.

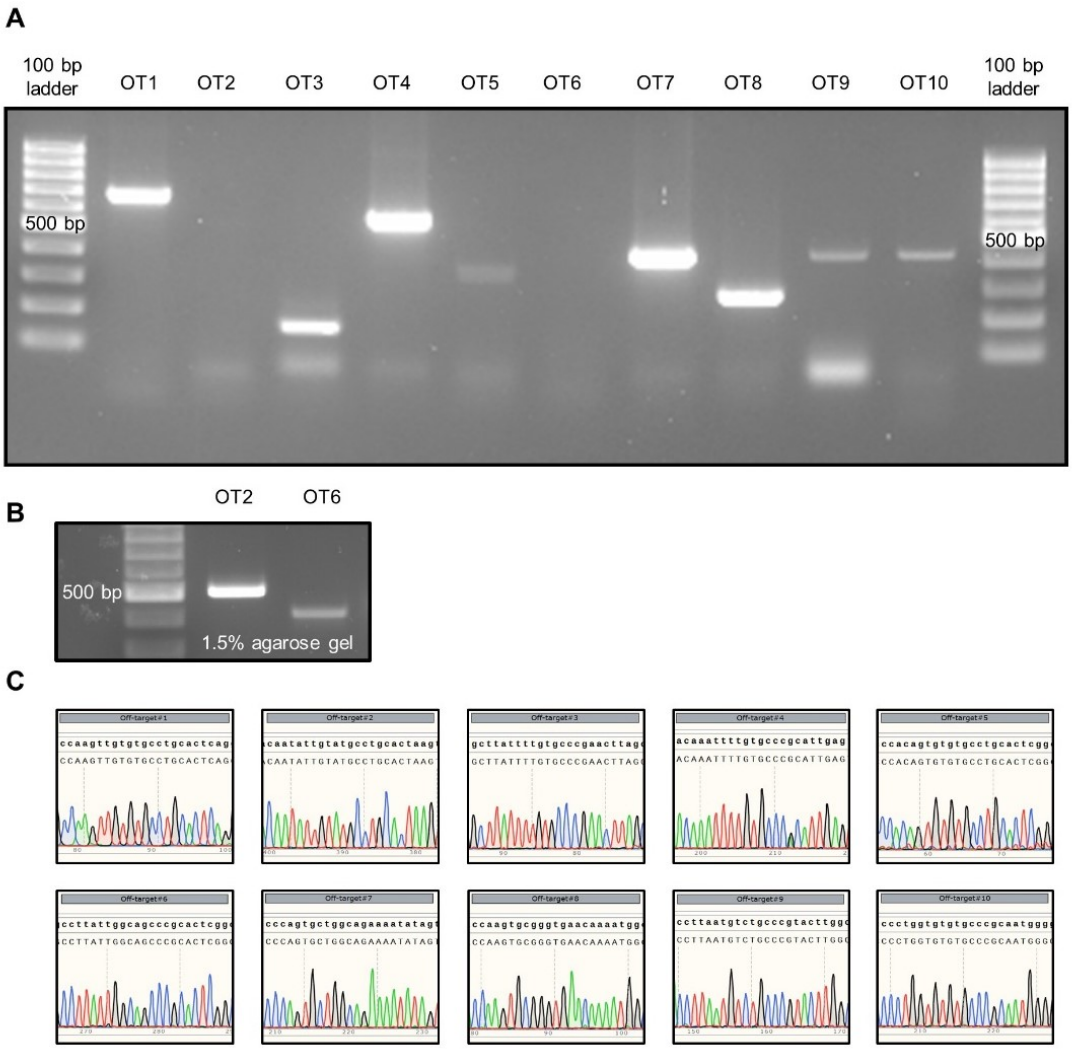

Figure 26: Off-target analysis CRISPR Mutation clone Mut#103
A *Amplification of the top 10 off-target regions of clone Mut#103.* ***B*** *Missing off-targets OT2 and OT6 were repeated as shown.* ***C*** *Off-target sequences of Mut#103 aligned to wild-type showing no off-target effects. OT: off-target.*

3.2.4 Subcloning of CRISPR clones

In order to validate clonal purity of the clones generated by CRISPR/Cas9, Rep#28 and Mut#103 were subcloned into *E.coli* and eight bacterial subclones per cell line were analysed. In case of Rep#28, sequencing of the extracted plasmids of the subclones revealed in 3 out of 8 subclones the wild-type sequence and in 5 out of 8 subclones the wild-type sequence with the silent mutation (Figure 27A). The silent mutation was shown to be incorporated heterozygously in the genomic sequence of Rep#28 before (Figure 22). Importantly, none of the subclones showed the G>A transition from the original cell line CMS32, which would indicate the presence of a mosaic population with still unedited or

NHEJ-repaired cells. For the bi-allelic mutant Mut#103 all 8/8 clones showed the C>T nucleotide exchange as expected for this CRISPR approach (Figure 27B).

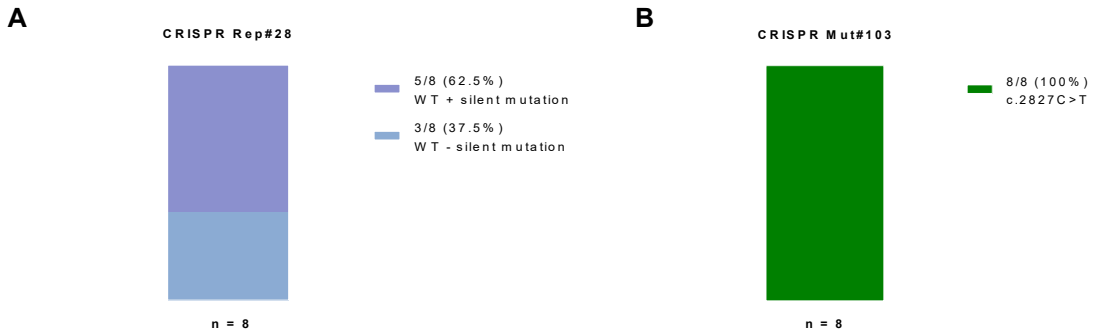

Figure 27: Subcloning of CRISPR clones into E.coli for determination of clonal purity
A *CRISPR clone Rep#28.* ***B*** *CRISPR clone Mut#103. WT: wild-type.*

3.3 Creation of a master cell bank

A MCB was created for CMS32, the isogenic controls (Rep#11, Rep#12, Rep#20, Rep#28) and the bi-allelic mutant (Mut#103). CMS32-hiPSCs were already expanded to the MCB before the CRISPR approach was started to be sure certain quality markers were present before usage of this cell line for the nucleofection. The genetically modified cell lines were expanded to MCBs after validation of the genotypes of the two CRISPR approaches. Table 19 gives an overview of the generated MCBs with the respective genotypes of the cell lines, the percentage of SSEA3-positive cells as an indicator for pluripotency, the screening for mycoplasm by PCR, the karyotype analysed with the NanoString method and the top 10 off-target analysis per cell line. To summarise, all cell lines of the MCBs showed high SSEA3 values, negative myoplasm screening, a normal karyotype and no off-target effects in the top 10 analysed. All genotypes were reconfirmed at the MCBs passage number (data not shown). Passage numbers were 19/20 for the MCB of CMS32, 31 for the isogenic controls and 33/34/35 for the bi-allelic mutant.

Table 19: Overview of the master cell banks of all hiPSC lines

HiPSC line	Description	Mutation	SSEA3	Mycoplasm	Karyotype	Off-targets (Top 10)
CMS32	Original cell line from index HCM patient	c.2308G>A (exon 23) – heterozygous	91.6%	negative	normal	-
Rep#11	Isogenic control for CMS32	Isogenic control with introduced silent mutation	94.7%	negative	normal	0/10
Rep#12	Isogenic control for CMS32	Isogenic control	98.6%	negative	normal	0/10
Rep#20	Isogenic control for CMS32	Isogenic control	89.5%	negative	normal	0/10
Rep#28	Isogenic control for CMS32	Isogenic control with introduced silent mutation	93.7%	negative	normal	0/10
Mut#103	Bi-allelic mutant	c.2308G>A (exon 23) – heterozygous *and* c.2827C>T (exon 27) – homozygous	96.4%	negative	normal	0/10

Figure 28 shows a representative example of the FACS analysis for the SSEA3 pluripotency marker. In this case, calculated SSEA3 values for clone Rep#12 were 98.6%.

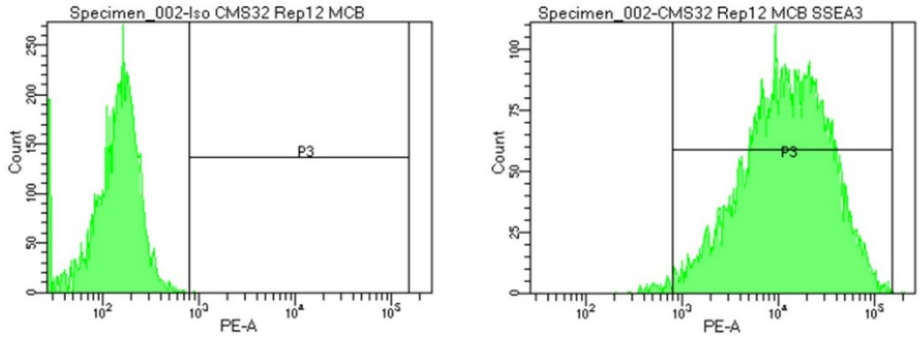

Figure 28: Validation for SSEA3 pluripotency marker by FACS
Representative FACS plot of CRISPR clone Rep#12 from the MCB showing 98.6% SSEA3-positive cells in comparison with the respective isotype control.

Figure 29 depicts the analysis of the karyotypes with the NanoString technology. All counts were compared to control cell lines with normal karyotype as validated by G-banding. No karyotypic abnormalities were found in the cell lines as shown.

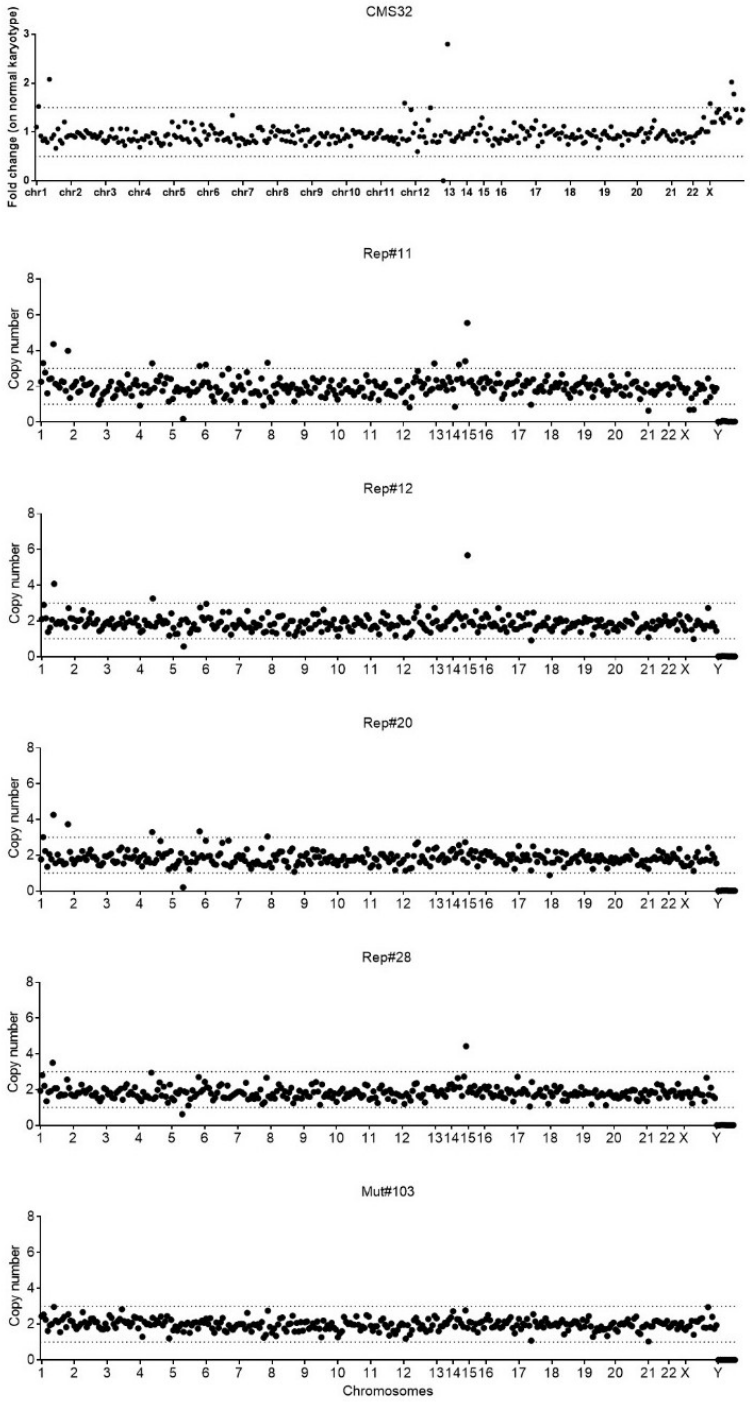

Figure 29: Validation of karyotype (nCounter Human Karyotype Panel)
Depicted are the karyotypes of the MCBs for CMS32, Rep#11, Rep#12, Rep#20, Rep#28 and Mut#103.

3.4 Differentiation of hiPSCs into cardiomyocytes

After establishment of all three hiPSC lines and expansion to MCBs, cells were prepared for cardiac differentiation. As described in 2.3, a monolayer based protocol was used. The protocol was started, when cells reached confluency of 70-80% (day 0) as shown in

Figure 30. At day 1, cells formed the typical “cheese-like” pattern, which gave this protocol the name “Cheese”. The following days, a large number of cells died and the holes were closed by growing cells (day 5). With the inhibition of the WNT signalling pathway from day 3 on and the addition of insulin (day 5), cells started to form a “mountain-like” pattern and an increasing cardiac morphology was observed (day 7). From then on, cells matured continiously and first contractions were visible around day 8/9 in the earliest cases or later around day 12. This differed between the differentiation runs and also between the hiPSC lines. The day when the CMs started to beat and their contraction behaviour gave hints towards a low or high CM percentage and therefore differentiation efficiency.

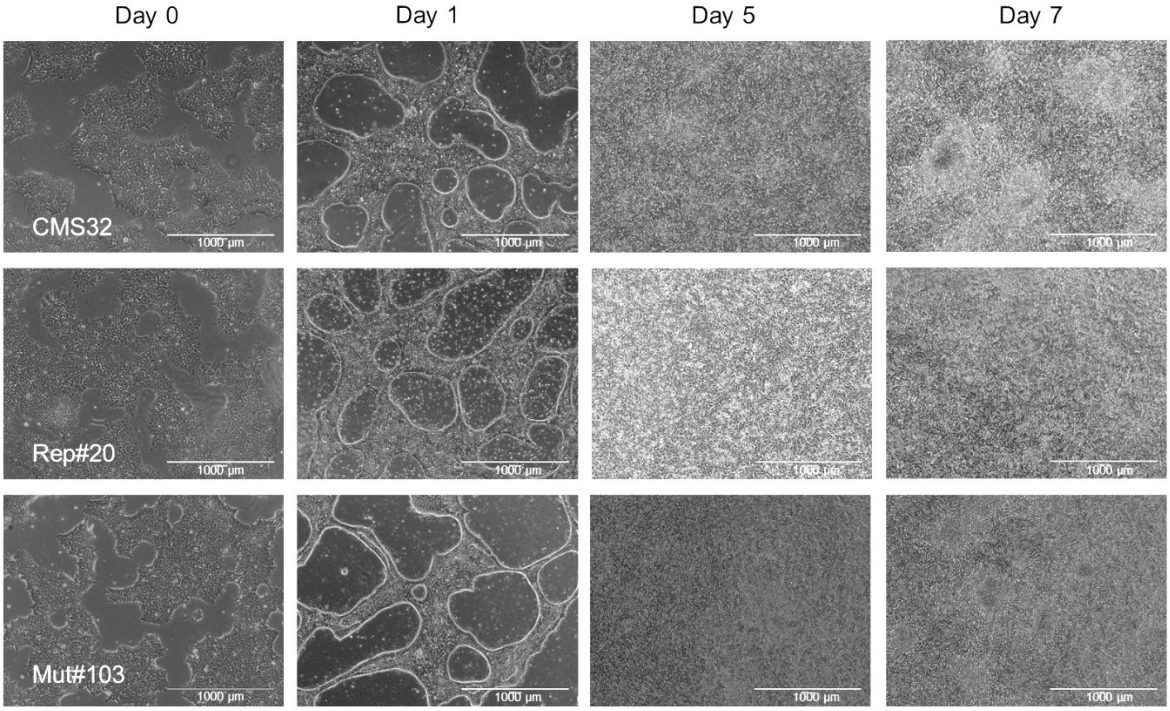

Figure 30: Representative pictures of the three cell lines during cardiac differentiation at different time points

In Table 20 all differentiation runs with the respective cell output and differentiation efficiency as calculated by cTnT values are listed. As known from previous experiments in the institute, a percentage of >60% of cTnT-positive cells was necessarily needed to generate beating EHTs and hence considered as a successful differentiation run. As depicted, the majority of differentiation runs reached above 80%.

Table 20: Overview of the differentiation runs and efficiencies

HiPSC line	Differentiation run	Number of seeded plates	Cell output	Efficiency (cTnT)
CMS32	Run#1	2 x 6-well-plates	19.6 x 10^6	94.8%
	Run#2	5 x 6-well-plates	65.4 x 10^6	65.2%
	Run#3	4 x 6-well-plates	47.7 x 10^6	91.4%
	Run#4	6 x 6-well-plates	71.2 x 10^6	34.5%
	Run#5	6 x 6-well-plates	38.0 x 10^6	35.8% / 46.3%
Rep#11	Run#1	2 x 6-well-plates	31.6 x 10^6	96.6%
Rep#12	Run#1	2 x 6-well-plates	12.4 x 10^6	91.1%
Rep#20	Run#1	2 x 6-well-plates	25.6 x 10^6	95%
Rep#28	Run#1	3 x 6-well-plates	59.9 x 10^6	99.5%
Mut#103	Run#1	4 x 6-well-plates	33 x 10^6	86%
	Run#2	2 x 6-well-plates	15 x 10^6	94.8%

In case of Run#5 of CMS32 two populations were separately analysed, which led to two different numbers of cTnT-percentages in this run.

A representative FACS plot with cTnT-positivity of 99.5% for clone Rep#28 is shown in Figure 31.

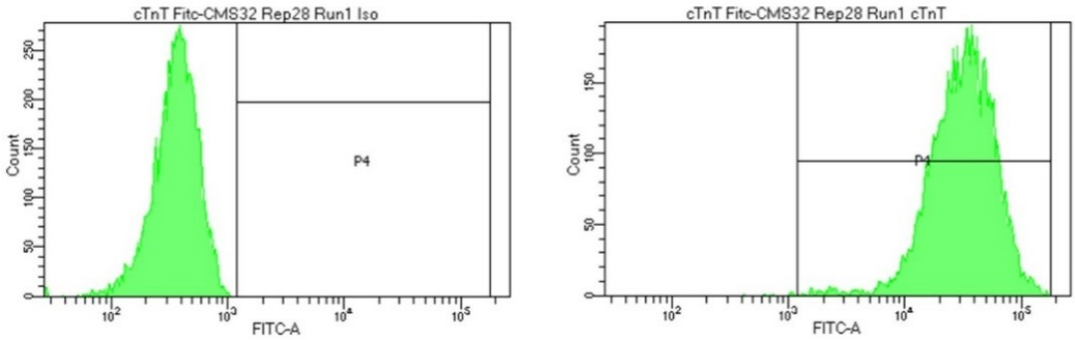

Figure 31: Staining for cardiac troponin T (cTnT) as marker for differentiation efficiency
Representative FACS plot of CRISPR clone Rep#28 showing 99.5% cTnT-positive cells in comparison with the respective isotype control.

3.5 Phenotypic analysis of cardiomyocytes in 2D culture

3.5.1 Impact of *MYBPC3* gene replacement therapy on transcript level

HiPSC-CMs were transduced with an AAV6 carrying the wild-type human *MYBPC3* sequence in order to test gene replacement therapy in 2D culture. Cells were harvested after one week for molecular analysis (cf. 2.4.3). The MOI was 10,000. PCR amplification

was performed with three different primer pairs for each cell line, one pair for amplification of total *MYBPC3* (primers in exon 1 and exon 2), one pair for the exogenous *MYBPC3* (primer in FLAG-tag and exon 2) and one primer pair for *GAPDH* as housekeeping gene. Importantly, the same amount of RNA was transcribed into cDNA for all samples. As shown in Figure 32, all samples with gene therapy (GT) expressed the exogenous *MYBPC3* and none of the non-transduced (NT) samples did, as expected. Additionally, the transgene was present among all groups as shown by the -RT (-RT from one GT sample per cell line), which could not be explained due to genomic DNA contamination since the *GAPDH* control was negative. Although this was not a quantitative PCR, some conclusions can be drawn in terms of expression levels since same amounts were loaded, *GAPDH* referred as loading control and PCR conditions were equal among the groups (number of cycles). In case of CMS32 (Figure 32A), NT samples seemed to be loaded slightly more than GT samples. This was also reflected in the intensity of total *MYBPC3* transcripts, where no major difference between GT samples and NT samples was notified or even slightly more intensity in the NT samples was observed. Hence, it can not be drawn the conclusion of higher expression levels after gene therapy for the heterozygous clone from this experiment. In contrast, for the bi-allelic mutant (Figure 32C) a slight increase in intensity of the GT band compared to the NT band with same loading intensities is visible, suggesting higher expression levels of *MYBPC3.* Interestingly, the NT sample of Mut#103 showed a band on transcript level for total *MYBPC3,* reflecting potentially the nonsense transcript that is not degraded at this point. This finding suggests that the mechanism of NMD is not fully working here, indicating likely the immaturity of the hiPSC-CMs. At last, an increase in intensity in the GT samples for total *MYBPC3* transcripts was found in the samples of Rep#28 compared to NT samples (Figure 32B).

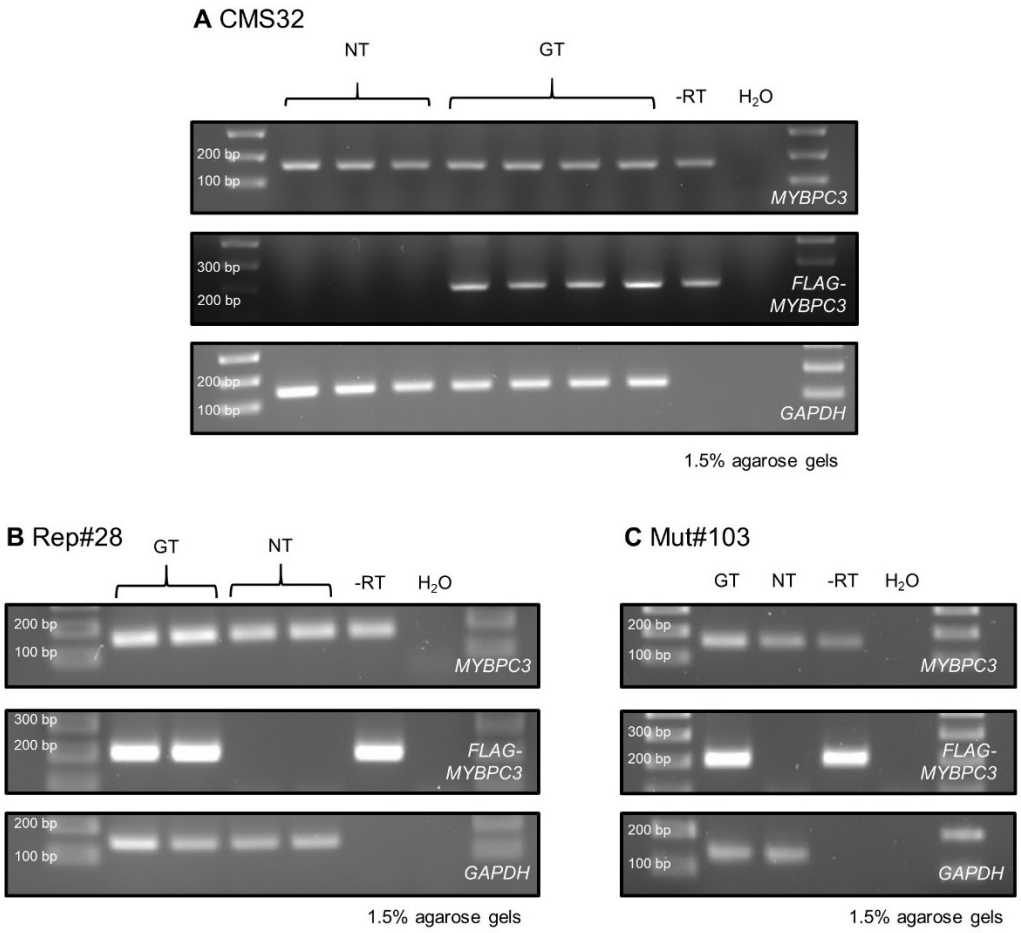

Figure 32: MYBPC3 expression levels after transduction with AAV6-TNNT2-FLAG-MYBPC3 (MOI 10,000)
Depicted are qualitative transcript (cDNA) levels of total MYBPC3 (151 bp), exogenous FLAG-MYBPC3 (193 bp) and GAPDH (136 bp) in hiPSC-CMs (2D). ***A*** *CMS32.* ***B*** *Rep#28.* ***C*** *Mut#103. GT: gene therapy; NT: non-transduced; -RT: without reverse transcriptase.*

In conclusion, since all three cell lines showed expression of FLAG-tagged *MYBPC3*, this experiment provided proof-of-principle for gene replacement therapy as this was already shown before (Prondzynski et al., 2017). Nevertheless, these data are preliminary and sample number and batch number must be increased to support these findings.

3.5.2 Evaluation of protein levels by Western blot

Analysis of protein levels by Western blot was performed on the one hand in order to compare protein amounts among the three genotypes (heterozygous, repaired and compound heterozygous) and on the other hand in order to analyse protein levels after gene replacement therapy. Gene replacement therapy was performed as described in 2.4.3 in detail.

First, we investigated whether the different CRISPR approaches lead to higher cMyBP-C levels in the isogenic control than in the heterozygous clone and absence of cMyBP-C in

the bi-allelic mutant as an indicator for successful creation of a functional knock-out due to the truncating mutations in both alleles of *MYBPC3*. Figure 33 shows a Western blot with protein levels of the three cell lines with (GT) and without (NT) gene therapy compared to cTnT as marker for cardiomyocyte loading and Ponceau as marker for loading of total protein amounts. When analysing the NT samples, the isogenic control Rep#28 showed highest levels of cMyBP-C among the three cell lines after quantification, as expected (Figure 34). In case of CMS32, cMyBP-C protein amounts differed a lot between two different samples. When taking the mean, calculated protein levels were 30.6% related to Rep#28 NT (Figure 34), which would suggest a state that is close to haploinsufficiency. But of much more interest is the fact that the bi-allelic mutant Mut#103 did not show any cMyBP-C expression, meaning that the mutant protein is not found although mutant transcripts were stable (cf. 3.5.1). This functional knock-out was also confirmed by quantification of the protein levels (Figure 34).

Second, the GT samples were analysed. Here, Rep#28 showed again the highest protein levels and even slightly higher protein levels (22.5%) in GT than in NT sample (Figure 34). In case of CMS32, three samples were loaded. For quantification, the first of the three samples was excluded since Ponceau was weak and cTnT only barely detected. Taking the mean of the two other samples, quantification analysis revealed 21.5% protein related to Rep#28 NT (Figure 34). This was lower than expected and also lower than its NT counterpart samples. As the heterozygous cell line remained difficult in evaluating the transcript levels as well (cf. 3.5.1), this suggests that either transduction did not work as properly as in the other cell lines (same AAV6 transduction experiment and CM batch) or it might be the case that the heterozygous state leads to allelic imbalance and is quite heterogenous among its own genotype. Eventually, when looking at Mut#103, 21.6% protein levels were found compared to Rep#28 NT (Figure 34). As no cMyBP-C was found in the NT sample of this genotype, this leads to the conclusion that this must be exogenous cMyBP-C and therefore gene replacement. Although protein amounts were not restored to wild-type levels, this provides a proof-of-principle of gene replacement therapy in the bi-allelic mutant.

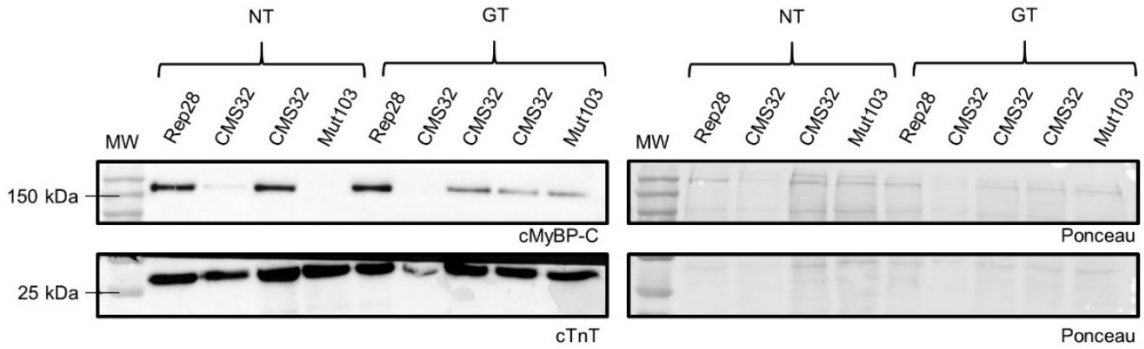

Figure 33: Western blot with antibodies directed against cMyBP-C and cTnT and Ponceau as loading controls
GT: gene therapy; MW: molecular weight; NT: non-transduced.

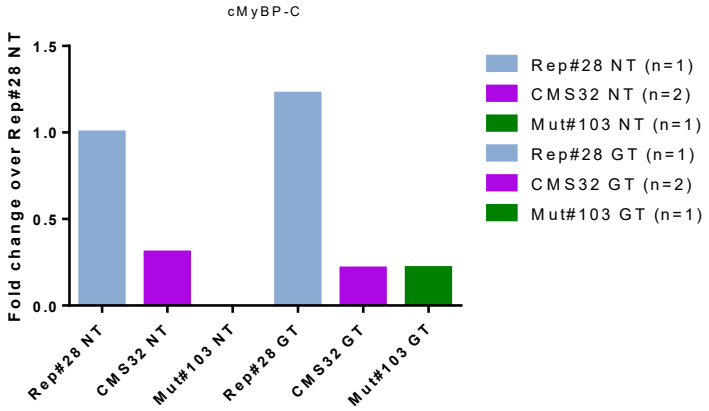

Figure 34: Quantification of cMyBP-C levels of the different cell lines before and after gene therapy
GT: gene therapy; NT: non-transduced; data are expressed as mean.

Next, a Western Blot with the same samples but with an antibody directed against FLAG-cMyBP-C was performed (Figure 35). cTnT and Ponceau were used again as loading controls. Eventhough unspecific bands and background signal were present for this antibody, some important observation could be done.

First, FLAG-specific band was not present in the NT samples, as expected. Second, Rep#28 GT showed the highest amount of exogenous cMyBP-C and was therefore set as reference for quantification (Figure 36). Third, as for total cMyBP-C one CMS32 GT sample was excluded from the analysis. When analysing the mean of the two other samples of this cell line, 43.9% exogenous cMyBP-C as compared to Rep#28 GT were found, meaning that exogenous *MYBPC3* was translated but not as successful as in its isogenic control (Figure 36). It remains unclear whether this was a technical transduction issue or whether this was due to the diseased cell line itself. Last, 18.9% of exogenous protein amounts were found in the Mut#103 GT sample compared to Rep#28 GT, leading towards the same direction of what was seen in the Western blot with total cMyBP-C, namely proof-of-principle

for gene replacement but with low efficiency in terms of protein restoration in the bi-allelic mutant.

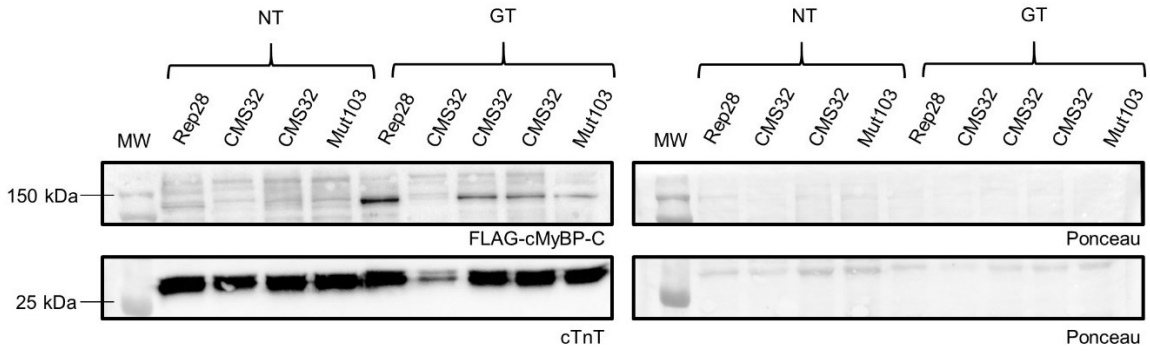

Figure 35: Western blot with antibodies directed against FLAG-cMyBP-C and cTnT and Ponceau as loading controls
GT: gene therapy; MW: molecular weight; NT: non-transduced.

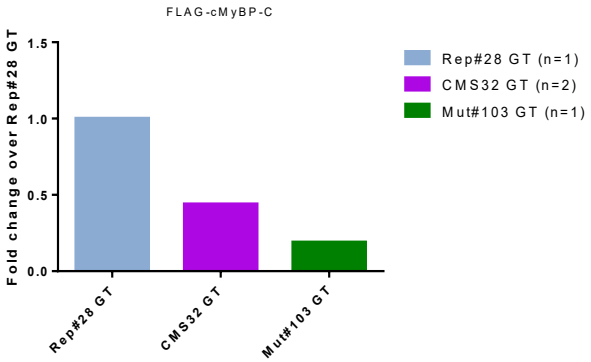

Figure 36: Quantification of exogenous cMyBP-C levels after gene therapy
GT: gene therapy; data are expressed as mean.

Hence, further experiments are necessary in order to underline these findings, increase efficiency of gene therapy and to validate also functional benefits of gene therapy in mutant cell lines.

3.5.3 Immunofluorescence analysis

Immunofluorescence analysis was performed in order to evaluate the localisation of cMyBP-C into the sarcomere and visualise potential differences between the cell lines. Images were taken from fixed cardiomyocytes after one week of culture as described in 2.4.6. First, immunofluorescence pictures with antibodies against cMyBP-C, α-actinin 2, which stains the Z-disks, and Hoechst for nuclei were examined (Figure 37).

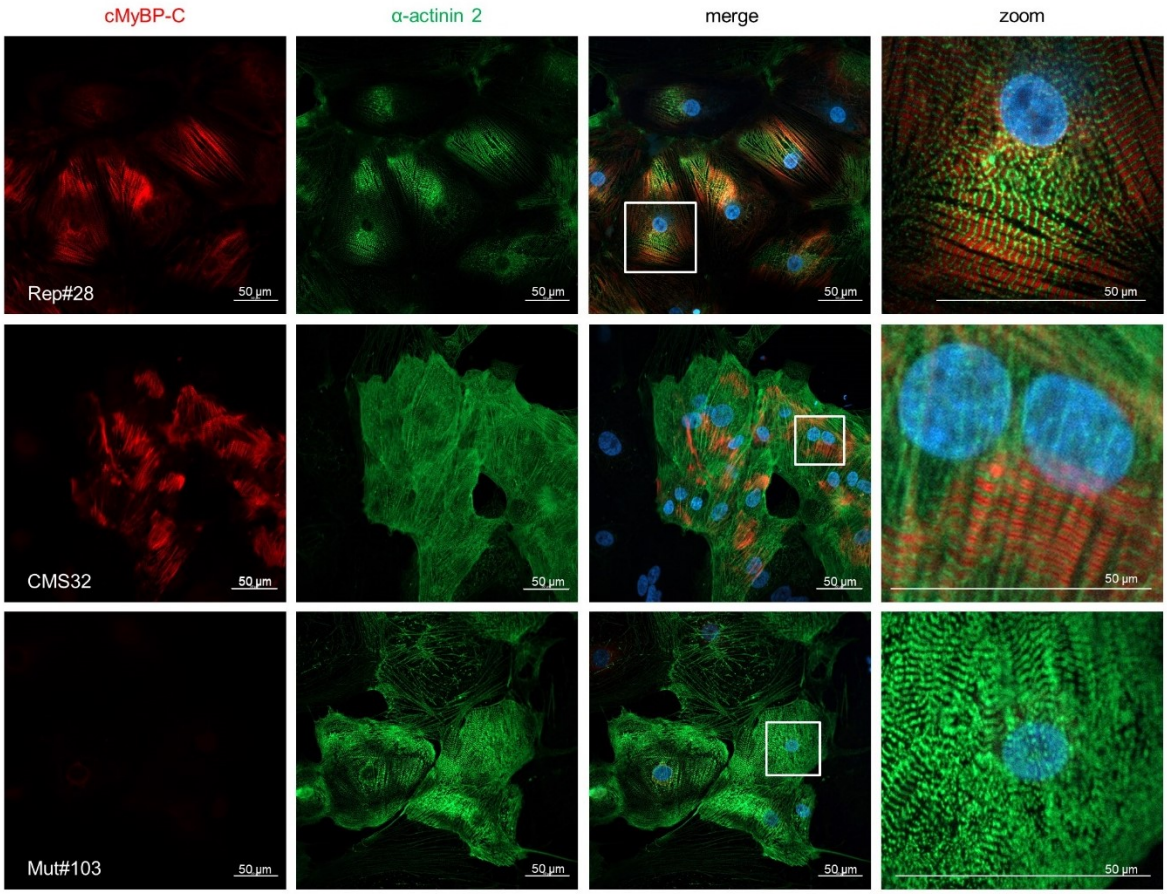

Figure 37: Representative immunofluorescence images of the three hiPSC-CM lines without gene therapy
Location of the zoom is reflected by the white rectangles.

In Rep#28-CMs and CMS32-CMs, the expected doublets of cMyBP-C in the sarcomere were found, suggesting correct localisation. See also Figure 53 in the supplement for additional images. Importantly, immunofluorescence pictures showed no signal for cMyBP-C in the bi-allelic mutant Mut#103 in none of the images taken. This confirms the findings by Western blot, namely the absence of cMyBP-C in the bi-allelic mutant and successful creation of a functional knock-out by CRISPR/Cas9 genome editing.

Next, immunofluorescence images taken after gene therapy were examined (Figure 38). AAV6-mediated transduction was performed as described in 2.4.3. For staining of exogenous cMyBP-C an antibody directed against FLAG-tag was used. Alpha-actinin 2 was used to stain the Z-disks of the sarcomere and Hoechst for nuclear staining. Interestingly, the signal for exogenous FLAG-cMyBP-C was higher in CMS32 than in Rep#28, suggesting higher translation or transduction of exogenous *MYBPC3* in the diseased cell line. Furthermore, the bi-allelic mutant Mut#103 exhibited FLAG-cMyBP-C, as expected from the findings in the Western blot, and importantly, the exogenous protein was properly incorporated into the sarcomere as validated by formation of typical doublets.

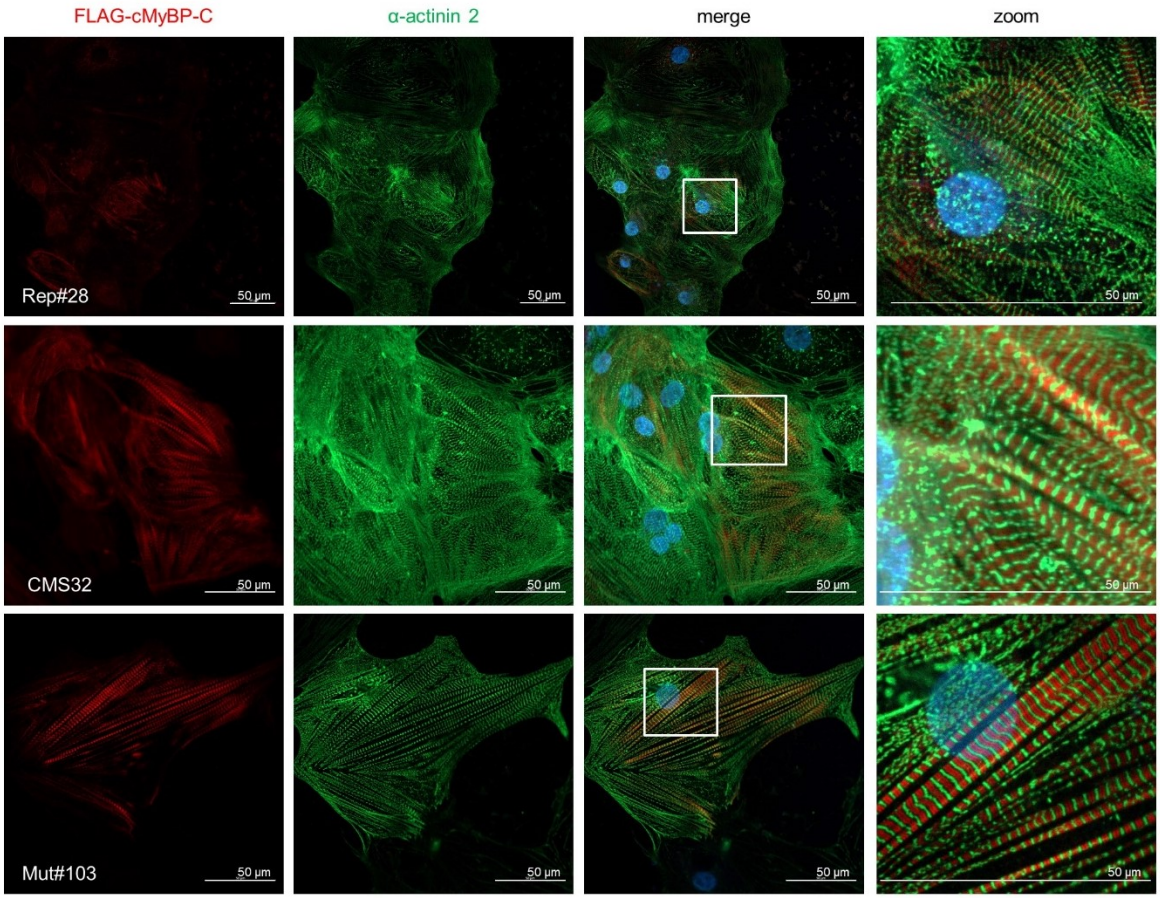

Figure 38: Representative immunofluorescence images of the three hiPSC-CM lines after MYBPC3 gene therapy
Exogenous cMyBP-C is detected by an antibody directed against the FLAG tag. Location of the zoom is reflected by the white rectangles.

Next, immunofluorescence analysis with co-staining with anti-cMyBP-C and anti-FLAG tag antibodies was performed in order to detect total cMyBP-C and exogenous cMyBP-C at the same time (Supplement Figure 54). Here, total cMyBP-C is shown in red and FLAG-cMyBP-C in green. Interestingly, while all cells were red, only few cells were co-stained in Rep#28, suggesting a low transduction efficiency. In addition, the green signal was way more intense in Mut#103, suggesting more transduction or stronger translation of the exogenous protein.

3.5.4 Measurement of cell size

As larger cell size is one of the typically reported hallmark of HCM, cell size measurements were performed in 2D culture from confocal images as described in 2.4.6. Preliminary results for cell size of CMS32-CMs before and after gene therapy are visualised in Figure 39.

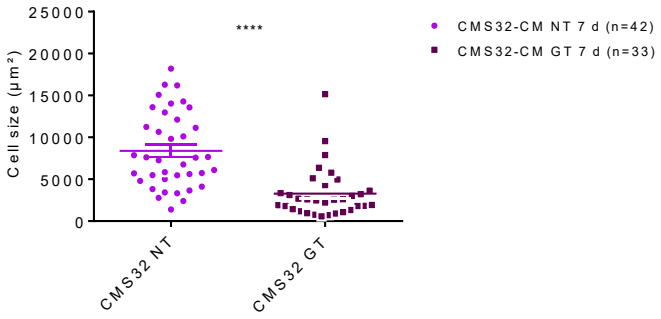

Figure 39: Cell size measurement
*d: days in vitro; GT: gene therapy; NT: non-transduced; data are expressed as mean ± SEM, ****p < 0.0001, unpaired t test.*

As shown, gene therapy in 2D monolayer culture led to a significant reduction in cell size. This hints towards beneficial effect of exogenous wild-type *MYBPC3* after gene replacement for the heterozygous *MYBPC3* mutant cell line.

3.6 Phenotypic analysis in 3D engineered heart tissues

3.6.1 Generation of EHTs and video-optical measurement

Human EHTs were successfully generated for all three genotype. Figure 40 shows representative images of EHTs of all three cell lines 33 to 34 days after casting. Pictures were taken while contraction patterns were recorded with the use of the video-optical measurement system called “Whitebox”. On the right hand side of each EHT, typical contraction peaks are shown as measured in 1.8 mM [Ca^{2+}] tyrode’s solution under spontaneous beating. The differences in terms of frequency and force generation under these conditions can be notified. The highest and lowest forces were achieved by the isogenic control (Rep#28) and the bi-allelic mutant (Mut#103), respectively. Conversely, the highest and lowest beating frequencies were observed in the bi-allelic mutant (Mut#103) and the isogenic control (Rep#28), respectively. In terms of frequency, this may be considered as a gene-dose-dependent increase in frequency, meaning that the number of beats per minute increased with the number of gene mutations of the cell line. Vice versa, a gene-dose-dependent decrease was observed concerning force.

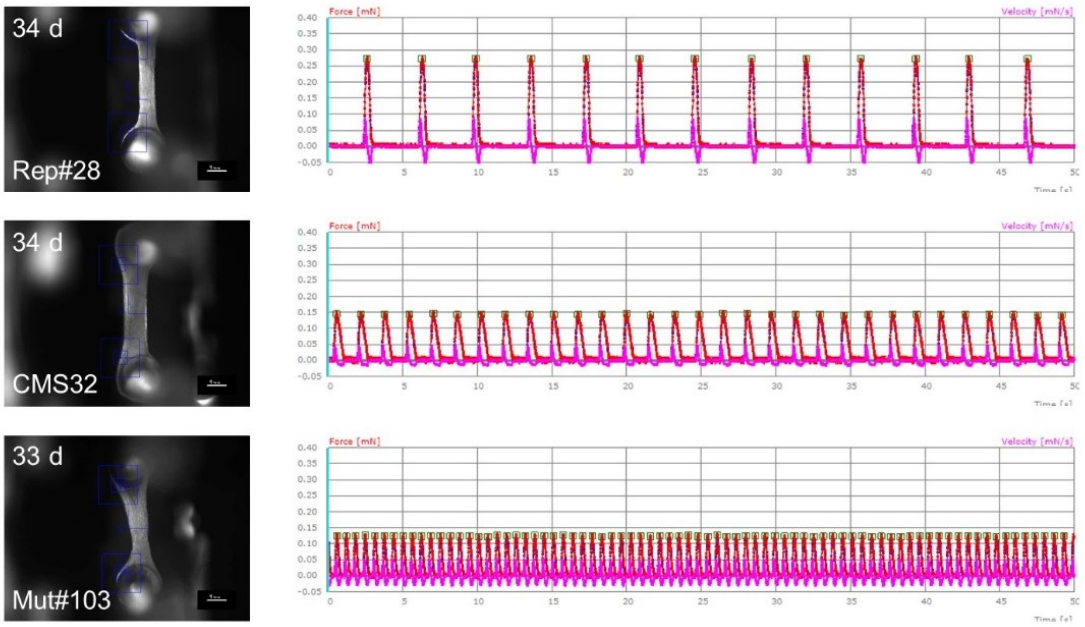

Figure 40: Representative images of EHTs and contraction peaks in 1.8 mM [Ca^{2+}] tyrode unpaced
d: days in vitro.

3.6.2 Baseline measurements

Force and frequency development

Contraction kinetics at baseline were recorded over time by video-optical measurement. Figure 41 shows the EHT force development of the three cell lines under spontaneous beating. Of note, the two isogenic control cell lines reached higher forces than the heterozygous and the bi-allelic mutant EHTs. The latter showed the weakest force development among the different genotype. In detail, maximal force was 0.28 mN in Rep#28, 0.20 mN in Rep#20, 0.14 mN in CMS32 and 0.12 mM in Mut#103, indicating that bi-allelic mutant EHTs generated solely about half of the force of its isogenic controls in this experimental setting.

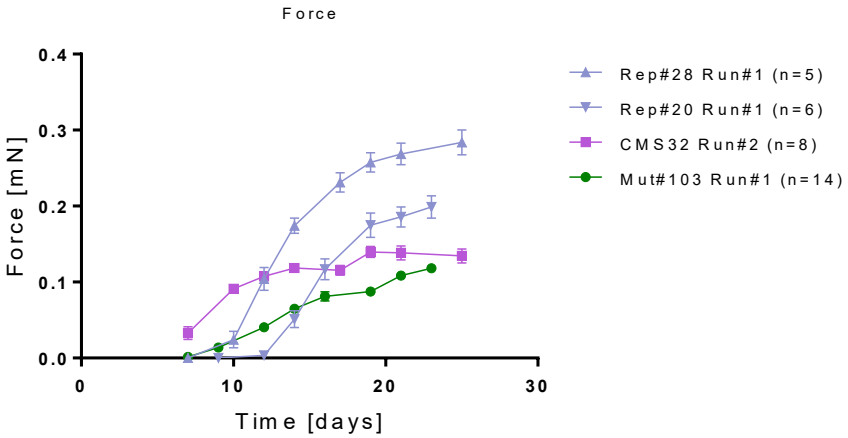

Figure 41: Force development in EHTs
n indicates the number of biological replicates from one differentiation batch. Data are expressed as mean ± SEM.

The beating rate was inversely correlated with the gene defect. Indeed, the bi-allelic mutant EHTs showed the highest beating rate, whereas the two isogenic control EHTs showed the lowest beating frequency. The heterozygous mutant EHTs (CMS32) showed intermediary beating rate frequency. Interestingly, all curves declined after they reached their maximum and did not stay on a plateau. This trend suggests that beating frequency might be reduced over time when EHTs are cultured for several weeks as a hypothetical consequence of the maturation process.

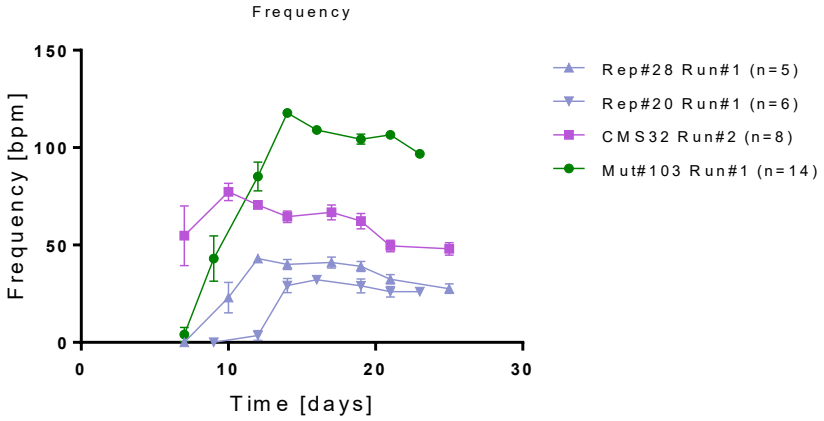

Figure 42: Frequency development in EHTs
n indicates the number of biological replicates from one differentiation batch. Data are expressed as mean ± SEM.

Contraction ($T1_{20\%}$) and relaxation ($T2_{20\%}$) kinetics analysed over time are presented in the supplement (Figure 55).

Average contraction peaks

Figure 43 shows absolute and normalised average contraction peaks in 1.8 mM [Ca^{2+}] tyrode's solution. EHTs were paced at 1.5 Hz. Visualisation of the contraction patterns here emphasizes the higher absolute force values (left) of the isogenic controls compared to the heterozygous cell line and the bi-allelic mutant. The shape of the normalised average contraction peaks (right) hints towards faster contraction kinetics in the bi-allelic mutant than in the other genotypes.

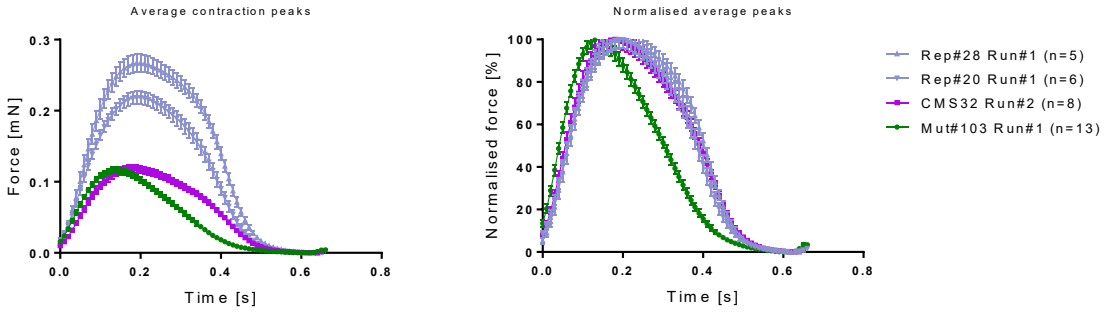

Figure 43: Absolute and normalised average contraction peaks of EHTs
Analysis was done after 33-34 days in culture. EHTs were paced at 1.5 Hz. n indicates the number of biological replicates from one differentiation batch. Data are expressed as mean ± SEM.

Comparison of force, frequency, $T1_{20\%}$ and $T2_{20\%}$

For further insights into contraction behaviour, a deeper analysis was done for four contraction parameters, namely force, frequency, contraction time ($T1_{20\%}$) and relaxation time ($T2_{20\%}$) after 33-34 days of culture in all groups as visualised in Figure 44.

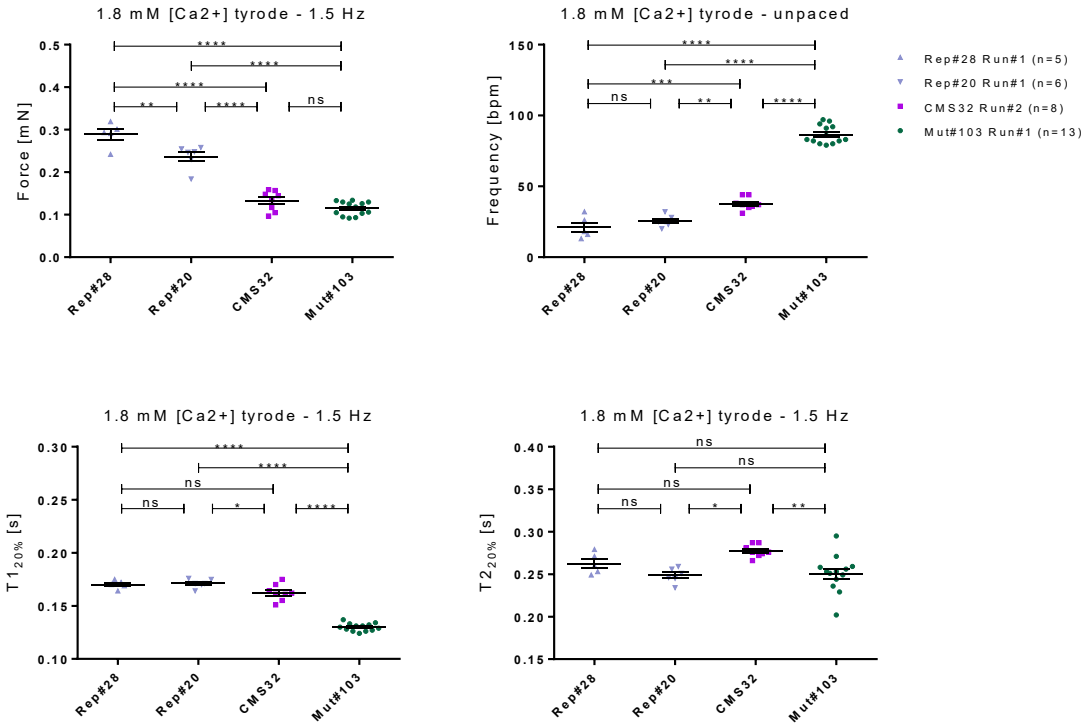

Figure 44: Comparison of force, frequency, $T1_{20\%}$ and $T2_{20\%}$ in EHTs
*Analysis was done at day 33-34 days in culture. n indicates the number of biological replicates from one differentiation batch. Data are expressed as mean ± SEM. ns = not significant, * p<0.05, **P<0.01, ***P<0.001, ****p < 0.0001, one-way ANOVA with Bonferroni post-test.*

Analysis of force showed significant differences between the groups except for the bi-allelic mutant versus the heterozygous mutant, which was not significant. Eventhough both isogenic control EHTs developed higher forces than the other genotypes, the force was significantly different among them, although the p-value was less strong than between the other groups. In terms of frequency, all EHTs groups were significantly different from each other except for the two isogenic controls and the bi-allelic mutant EHTs exhibited the highest beating frequency as compared to the other groups. In case of $T1_{20\%}$, the bi-allelic mutant EHTs had the fastest contraction behaviour and significantly shorter than all other EHTs groups fitting the fastest beating rates. Rep#28 and Rep#20 EHTs didn't significantly differ neither in contraction nor relaxation time. $T2_{20\%}$ analysis revealed mixed results without clear trends between the genotype.

3.6.3 Response to high calcium concentrations

In order to investigate the susceptibility to arrhythmic beating patterns, EHTs were challenged with high calcium concentrations over night. Afterwards, the RR scatter, a parameter of irregularity between contraction peaks, was analysed. Unexpectedly, only

Rep#28 EHTs showed high RR scatters, whereas Mut#103, CMS32 and Rep#20 EHTs did not get arrhythmic.

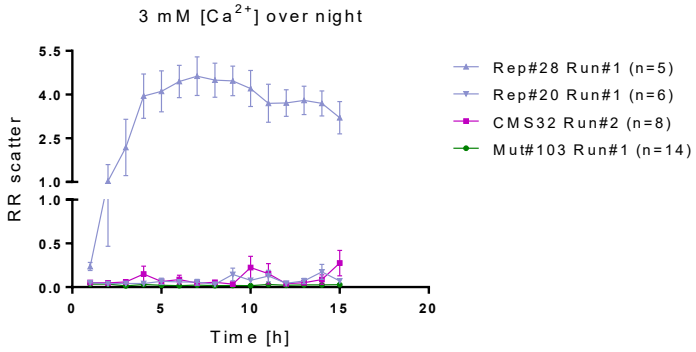

Figure 45: RR scatter analysis during high calcium exposure of EHTs
n indicates the number of biological replicates from one differentiation batch. Data are expressed as mean ± SEM.

Nevertheless, some interesting findings in the EHTs after long incubation time could be observed. On the one hand, some EHTs stopped beating during long exposure of high calcium, especially CMS32 (data not shown). On the other hand, morphological differences in Mut#103 were found after this experiment (Figure 46). Some of these bi-allelic mutant EHTs got cracks and holes. This might either be explained due to the higher beating frequency itself that was even more increased during high calcium exposure (data not shown) or it might be an issue of this cell line to handle high calcium concentrations.

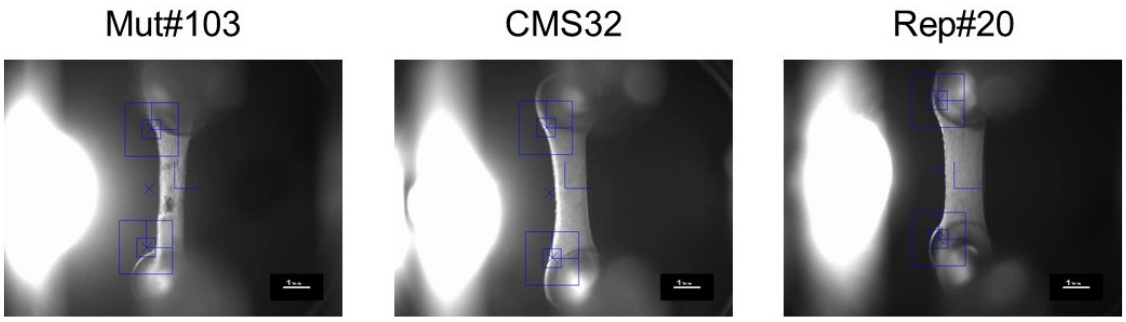

Figure 46: Examples of EHT morphology after 15 hours in 3 mM [Ca^{2+}]

3.6.4 Calcium concentration-response curve

To analyse the effect of calcium on force generation, EHTs were exposed to different external calcium concentrations. Figure 47 depicts the calcium concentration curve for all three genotypes, comparing normalised forces of each group with different calcium levels. Data are plotted as Hill slope and EC_{50} values for calcium were calculated in order to investigate calcium sensitivity. Starting at 0.3 mM external calcium, all groups showed an increase in force until 10 mM. Nevertheless, differences were observed between the

groups. EC_{50} values were lower in both isogenic controls (Rep#28: EC_{50} = 0.44 mM; Rep#20: EC_{50} = 0.53 mM) than in CMS32 (EC_{50} = 0.88 mM) and bi-allelic mutant EHTs (Mut#103: EC_{50} = 1.1 mM). In the direct comparison, the latter needed the highest calcium concentration to generate half maximal force. Hill slopes differed in steepness accordingly (Mut#103: 2.51; CMS32: 2.20; Rep#28: 1.63; Rep#20: 1.45). In summary, these data suggest lower calcium sensitivity towards external calcium in the diseased cell lines than in the isogenic controls, although this should be taken only as a trend due to few biological replicates.

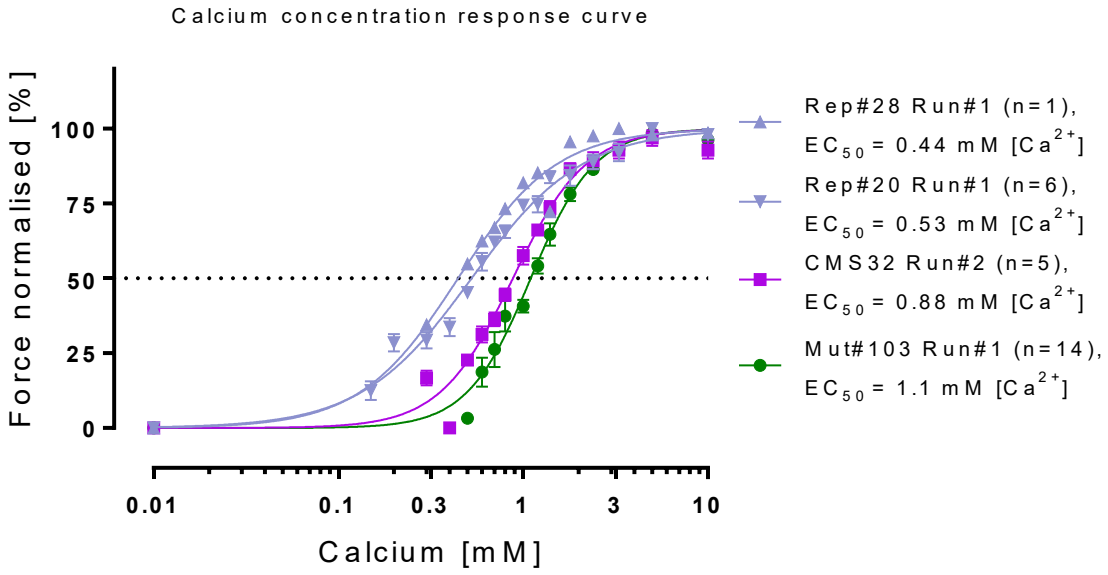

Figure 47: Calcium concentration curve of EHTs
n indicates the number of biological replicates from one differentiation batch. Data are expressed as mean ± SEM.

3.6.5 Response to isoprenaline and carbachol

The next step was to elucidate the effect of the β-adrenergic agonist isoprenaline and the muscarinic receptor agonist carbachol on the three EHT genotypes. Isoprenaline is known as a positive inotropic drug and carbachol, theoretically, antagonises this effect due to stimulation of muscarinic receptors. Therefore, EHTs were placed in tyrode's solution containing the calculated EC_{50} values for calcium. In all three groups, this led to a reduction in force but to a different extent (Figure 48A). Force of Mut#103, CMS32 and pooled Rep#20/28 EHTs was reduced to 71%, 64% and 51% respectively. Compared to baseline in 1.8 mM [Ca^{2+}] isoprenaline was able to recover force, when added to EHTs in their respective EC_{50} for calcium (CMS32 to 95%; Rep#20/28 to 92%), except for the bi-allelic mutant EHTs, which had significantly lower force after addition of 100 nM isoprenaline

reaching only 85% of baseline level. Still, when compared to EC_{50} for calcium, isoprenaline showed an increase in force but was not able to recover force completely, as this was the case for the other groups. Among all genotypes, addition of isoprenaline showed the expected positive inotropic effect, when added to EHTs in their respective EC_{50} calcium concentrations. Moreover, addition of carbachol on top of isoprenaline led to partial antagonism of isoprenaline's effect (Mut#103: -23%; CMS32: -16%; Rep#20/28: -21%) to similar extents in all EHTs groups. Isoprenaline treatment was expected to lead to a positive chronotropic effect on beating rates. Figure 48B shows the analysis of frequency in the three groups. Isoprenaline had a strong positive chronotropic effect in the heterozygous mutant (CMS32: +67%) and the isogenic control EHTs (Rep#20/28: +87%). The increase in beating rate for Mut#103 EHTs was very small, only 6% compared to baseline in EC_{50} for calcium in tyrode. In all three groups, carbachol led to a reduction of frequency, when added to isoprenaline treated EHTs (Mut#103: -20%; CMS32: -44%; Rep#20/28: -62%).

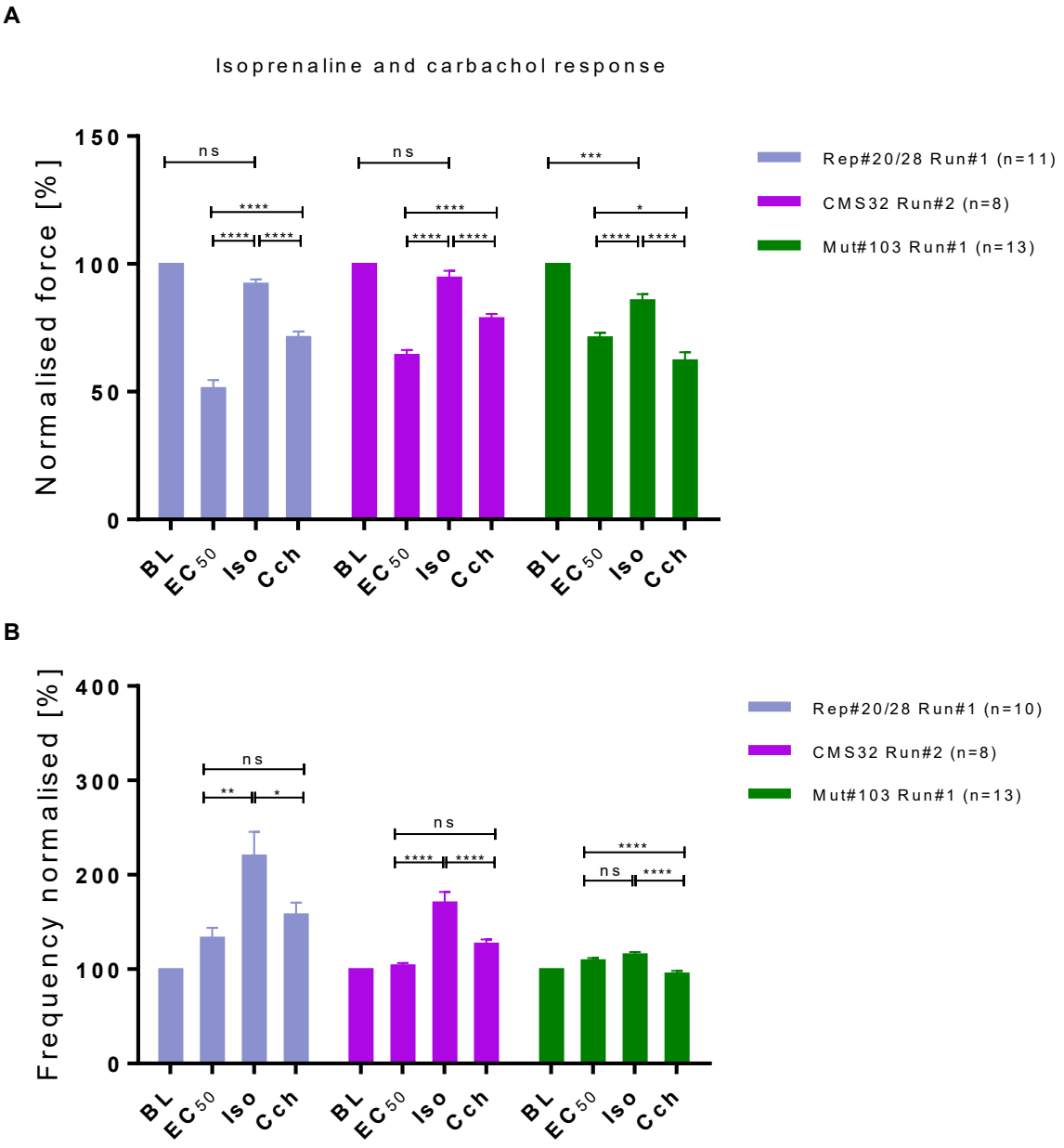

Figure 48: Isoprenaline and carbachol response of EHTs – Force and frequency
A *Effect on force (paced).* ***B*** *Effect on frequency (unpaced). n indicates the number of biological replicates from one differentiation batch. Data are expressed as mean ± SEM. ns = not significant, *p<0.05, **P<0.01, ***P<0.001, ****p < 0.0001, one-way ANOVA with Bonferroni post-test. BL = baseline in 1.8 mM [Ca^{2+}]; Cch = carbachol (10 µM); EC_{50} = measurements at calculated EC_{50} calcium levels; Iso = isoprenaline (100 nM). Pacing frequencies: Rep#20/28 (1.0 Hz), CMS32 (1.0 Hz), Mut#103 (2.0 Hz).*

Data of contraction ($T1_{20\%}$) and relaxation times ($T2_{20\%}$) under isoprenaline and carbachol treatment are shown in the supplement (Figure 56).

3.6.6 Force-Frequency-Relationship

The influence of frequency on force generation was tested in the three genetic groups. Due to the difference in spontaneous beating rates, EHTs which did not follow the pacing were excluded from the analysis. Results are shown in Figure 49.

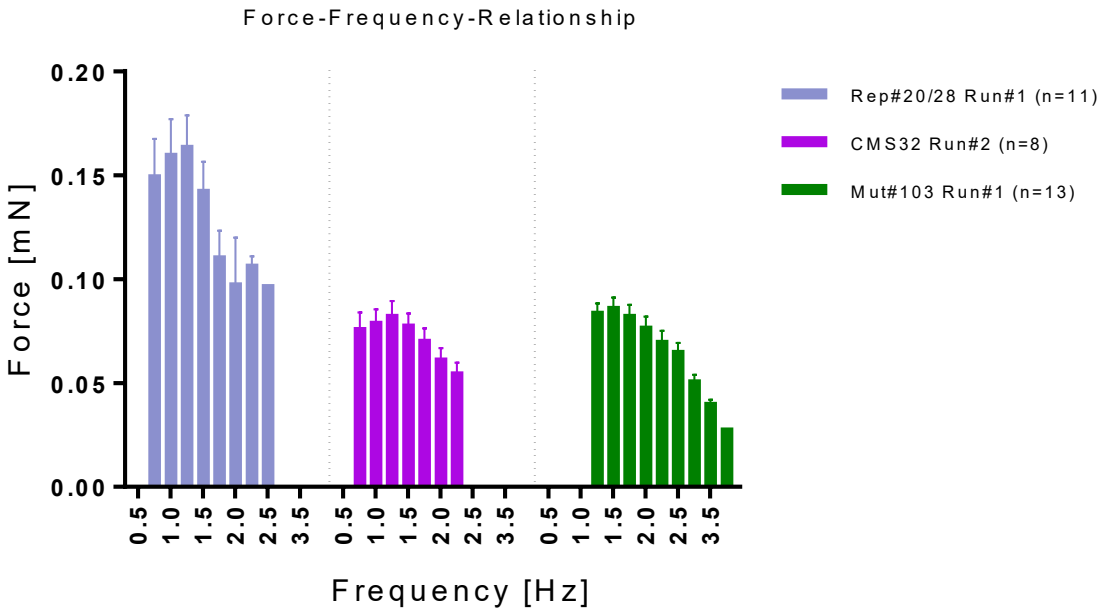

Figure 49: Force-Frequency-Relationship in EHTs
Measurements were done at calculated EC_{50} calcium levels. n indicates the number of biological replicates from one differentiation batch. Data are expressed as mean ± SEM.

As depicted, all three cell lines show a “mountain-like” pattern with increasing force at lower frequencies until a maximum followed by a decrease at higher pacing frequencies. Mut#103 showed maximal force at 1.5 Hz while CMS32 and the isogenic control EHTs at 1.25 Hz. The bi-allelic mutant EHTs were able to follow higher pacing frequencies as expected from its higher spontaneous beating rate.

4 Discussion

In the background of the importance of HCM as the most frequent cardiac genetic disease the present study was conducted. HCM caused by *MYBPC3* mutations reflects the major cause of sudden cardiac death among young people (Braunwald, 2017). Double-truncating *MYBPC3* mutations are very severe and lead to death of infants at very young age (Ortiz et al., 2009; Wessels et al., 2015). For these, heart transplantation is the only therapeutic option to date (Carrier, 2020). Therefore, deciphering the disease mechanisms and developing new treatment options for these children is very important. Especially *MYBPC3* gene therapy could cure the cause of the disease, namely the absence of cMyBP-C in these patients (Prondzynski et al., 2019b).

In this study, we aimed at [1] implementing an hiPSC-based disease model for HCM with mono- and bi-allelic truncating *MYBPC3* mutations and creating an isogenic control with CRISPR/Cas9, [2] investigating the molecular and functional consequences of these mutations and [3] analysing the disease phenotype using hiPSC-derived CMs in 2D and 3D EHTs.

The main findings of this work can be summarised as follows.

[1] A human cellular model was implemented with the use of CRISPR/Cas9 genome editing and the hiPSC technology. From the hiPSC line of the index HCM patient carrying a heterozygous truncating *MYBPC3* mutation (c.2308G>A), we created two hiPSC lines, an isogenic control and a bi-allelic mutant carrying two distinct truncating *MYBPC3* mutations (heterozygous c.2308G>A and homozygous c.2827C>T), which subsequently led to the complete absence of cMyBP-C (functional knock-out). Off-target effects were not found in the top 10 analysed.

[2] *MYBPC3* mRNA levels were lower with 72.5% in the septal myectomy of the HCM patient than in non-failing heart samples. Nonsense transcripts were not detectable by sequencing. In hiPSC-CMs, mutant transcripts were detectable, although at low extent, but were extensively stabilised after inhibiting the NMD. Mutant transcripts reflected 17.6% of total *MYBPC3* transcripts after treatment of heterozygous *MYBPC3* hiPSC-derived CMs.

[3] Sequencing of mutant transcripts revealed first evidence for the molecular consequence of the index patient's mutation (c.2308G>A), namely partial retention (298 bp) of the adjacent intron 23 inducing a frameshift with a PTC (Asp770Serfs98X).

[4] Truncated cMyBP-C was not detected by Western blot.

[5] cMyBP-C protein levels were lower (30.6%) in the heterozygous than in the isogenic control hiPSC-CMs.

[6] All three genotypes were successfully transferred to the 3D EHT model and underwent further examination. The absence of cMyBP-C in the bi-allelic mutant line led to higher beating frequency and lower force generation than in the heterozygous and repaired (isogenic control) EHTs. Furthermore, frequency and force developments under β-adrenergic stimulation were impaired in the bi-allelic mutant EHTs.

[7] AAV6-mediated *MYBPC3* gene replacement therapy confirmed proof-of-principle for gene therapy in hiPSC-CMs with heterozygous and for the first time bi-allelic *MYBPC3* mutations *in vitro*. Cell size was reduced in heterozygous hiPSC-CMs after gene therapy.

The present work shows that HCM can be modelled *in vitro* in a human context with the use of CRISPR/Cas9 genome editing to manipulate hiPSCs and their subsequent differentiation into CMs with its advantages and future implications discussed below.

4.1 CRISPR/Cas9 gene editing as a tool for engineering the genome

The major advantages of the CRISPR/Cas9 technology are obvious. Above all, it facilitates genome editing to an enormous extent in terms of labour time and editing efficiency. This led to a dramatic increase in CRISPR/Cas9-related publications even from research groups that have not used genome editing techniques before and which were able to enrich their methodical spectrum through this (Sternberg and Doudna, 2015).

In the present study, it was shown that CRISPR/Cas9 can be used to correct a disease specific mutation in *MYBPC3* and to introduce a second, unrelated mutation in the other allele in *MYBPC3* at the homozygous state. To achieve this, the RNP-based CRISPR approach was used instead of the older plasmid or mRNA strategies for the expression of Cas9. This was reported to cause less cellular toxicity, higher editing efficiencies and less off-target effects (Kim et al., 2014; Liang et al., 2015). Indeed, high Cas9 activity (>90%) was observed in the CRISPR clones analysed here. The activity was even higher than the 87% of indel rates in iPSCs that were reported by the group of Liang et al. (2015) and markedly higher than the reported indel rates of plasmid approaches (Fu et al., 2013). Additionally, even the HDR pathway, that is known to occur at low rates as well as with a huge variability in rate (Ran et al., 2013), occurred with high efficiency in the present CRISPR approaches with rates up to 14.6% in the case of creation of the isogenic controls. The approach with the insertion of the second mutation showed 6.4% of HDR-repaired

clones, which may be explained due to the assumption that targeting a monoallelic mutation with one specific guide RNA is easier than introducing a mutation (heterozygous or homozygous) in a locus with two wild-type alleles. Here, the occurrence of indels would cover the HDR event on the other allele since the guide RNA binds specifically to both alleles. Nonetheless, these data suggest that the *MYBPC3* gene may be easily engineered, although it is known that gene and locus specific differences exist in the repair mechanisms after DSBs and these data cannot exclude locus specific differences among the *MYBPC3* gene (Ran et al., 2013; Saleh-Gohari and Helleday, 2004).

One major obstacle to deal with when using the CRISPR/Cas9 technology is the potential of off-target effects in the genome, meaning that other loci with high homology to the on-target region may be targeted by the gRNA. Since the 5'-NGG PAM sequence for the *S. pyogenes* Cas9 exists every 8-12 bp in the genome, it is very likely that homologous regions are recognised by the gRNA (Ran et al., 2013). The use of other Cas9 species recognising different PAM sequences than NGG or Cas9 nickase strategies might be helpful to decrease off-target probability, but often they are less efficient or less investigated than the well-known Cas9 from *S. pyogenes* (Hu et al., 2018; Ran et al., 2013). Due to these reasons, the present study was carried out with the RNP-based CRISPR approach using recombinant Cas9 from *S. pyogenes* since off-target activity was shown to be substantially lower with this strategy (Kim et al., 2014; Liang et al., 2015). Still, excluding off-targets is necessary in order to provide reliable data. Indeed, sequencing of the top 10 off-target loci revealed no off-target activity. For off-target analysis, primer pairs spanning at least 300 bp were designed (except for two off-targets in the CRISPR Mutation approach) whenever possible. Here, deletions ranging in this fragment size would have been detected.

Yet, another major concern is that large and devastating on-target deletions would have been overlooked. Kosicki et al. (2018) reported that they have found deletions scaling up until the range of kilobases. This is especially dramatic when using the CRISPR/Cas9 technology *in vivo*. Still, in the specific case of the present study the occurrence of monoallelic deletions in the on-target region can be objected by the following. (1) In the case of the bi-allelic mutant, a large deletion followed by a reframing on the one hand would have been detected by Western blot and seems therefore unlikely. On the other hand, a deletion followed by a frameshift would subsequently lead to a PTC and therefore implicate the same consequence as the inserted point mutation, namely a functional knock-out. Indeed, the absence of cMyBP-C was validated by Western blot and immunofluorescence. (2) In the case of isogenic controls, the on-target PCR validating the genotype spanned an amplification region of 1011 bp, which may already be considered as sufficient to detect most deletions. Furthermore, two of the isogenic control clones – Rep#28 and Rep#11 –

heterozygously incorporated a silent mutation from the repair template, validating its bi-allelic state in this locus. Nevertheless, incorporation of silent mutations from templates is often but not consistently seen in previous studies (Ma et al., 2017; Paquet et al., 2016; Prondzynski et al., 2019a) and hence is not necessarily present. HDR may also be achieved by using the wild-type allele as template instead of the provided ssODN (Ma et al., 2017). For future studies, off-target analysis may also be combined with the means of next generation sequencing and whole genome sequencing (Ran et al., 2013; Zhang et al., 2015).

Although the list of concerns and negative implications related to the CRISPR/Cas9 technology is probably as long as the list of advantages, one fact should be further emphasised. Investigations of mutation-specific phenotypes have never been as reliable as to date since CRISPR/Cas9 opened the opportunity of investigations under isogenic conditions, which is especially of interest for disease modelling (Eschenhagen and Carrier, 2019; Zhang et al., 2018). Hence, data artefacts due to different genetic backgrounds between unrelated individuals are excluded.

4.2 Using hiPSC-CMs as an *in vitro* disease model system

In the past years, there has been a growing interest in modelling diseases using hiPSCs since it offered the opportunity of an unlimited source of human cells (Hockemeyer and Jaenisch, 2016; Merkle and Eggan, 2013). It is well accepted that small and large animal models are useful to study a whole organism in a disease context, but in contrast, animals, especially rodents, are different from humans and gained knowledge cannot always been transferred to human diseases (Rajala et al., 2011). Therefore, hiPSC-CMs have been used recently to model cardiac disease *in vitro* with the underlying assumption that phenotypes of patients will be visible in the dish (Eschenhagen et al., 2015). Still, one major limitation of this model is the immaturity of these cells. They display many characteristics of fetal-like CMs in terms of electrophysiologic and morphologic properties as well as gene expression patterns (Feric and Radisic, 2016). Many attempts have been used in order to improve and mature the phenotype of hiPSC-CMs. Generation of 3D EHTs is considered to improve maturity in many aspects as recently described and is accepted as one of the models with the most similarly reproducing human physiology that is available to date, at least in terms of function and maturity (Feric and Radisic, 2016; Mannhardt et al., 2016; Ulmer et al., 2018). Therefore, the decision was to perform the present disease modelling study with the use of this model in addition to 2D culture experiments.

Since the limitations of this highly elaborated and sophisticated model of hiPSC-CMs and EHTs are well known, certain quality controls when using this model are regarded of urgent necessity, e.g. karyotypic testing, CM content, pluripotency of hiPSCs, etc… (Eschenhagen and Carrier, 2019; Musunuru et al., 2018). This study was conducted whilst following the statement of the American Heart Association with regards to testing the karyotype and none of the cell lines used had abnormalities. Genomic instability is often reported for hiPSC-derived cell lines and prolonged culture time is even increasing instability (Taapken et al., 2011). Therefore, the CRISPR/Cas9 approaches and following experiments were restricted to passage numbers >19 and <40. Additionally, it is recommended to provide a certain number of differentiation batches – the greater the better, but at least n=3 as our institute internal standard – since inter-batch variability is reported to be higher than intra-batch variability in EHTs (Mannhardt et al., 2017; Musunuru et al., 2018). In this study, number of batches remained low due to the limited time. Hence, the number must be increased in future experiments according to the guidelines.

Moreover, the cardiac differentiation protocol – monolayer or EB-based – is reported to influence cell outcome in different aspects. On the one hand, monolayer protocols are shown to lead to high CM purity, whereas EB-based protocols to high scalability (Breckwoldt et al., 2017; Zhang et al., 2012). In this study, a monolayer protocol was used and high CM efficiencies with mostly over 80% were yielded in eight out of eleven differentiation runs. Three additional differentiation runs failed (cTnT < 70%) due to unknown reasons. Furthermore, the differentiation method may also have an impact on maturity and cell properties of the resulting CM population (Jeziorowska et al., 2017), although this has only rarely been examined. The comparison of the two differentiation methods was out of the scope of this thesis. Therefore, sticking consistently to the same differentiation method was considered optimal here providing the most comparable experimental conditions.

Despite the fact that the EHT model may display many of the characteristics found in a human heart, e.g. Ca^{2+} handling and electrophysiologic properties (Stoehr et al., 2014; Uzun et al., 2016), it is obvious that it is morphologically way apart from a human heart composed of the four chambers with separating walls and valves. Besides, it is usually generated by using a cellular population containing mainly CMs but also to a lower and from batch-to-batch variable proportion of non-myocytes resulting from cardiac differentiation. This does not represent at all the composition of cell types found in a human heart, where other cell types, such as endothelial cells and fibroblasts play also an important role (Zhou and Pu, 2016). Additionally, EHTs are not intrinsically under neurohumoral and hormonal stimulation as the adult human heart is usually exposed to *in vivo* (Feric and Radisic, 2016) and co-culture of hiPSC-CMs with sympathetic neurons is therefore under investigation for instance

(Winbo et al., 2020). For this reason, EHTs may give valuable but limited insights into physiology and pathophysiology of diseases such as cardiomyopathies.

While most HCM patients develop symptoms at middle age showing that the phenotype of those patients with mostly heterozygous mutations has a late onset (Marian and Braunwald, 2017), hiPSC-CMs and EHTs are immature, meaning that especially early development is accessible to be studied as discussed above. Of course, investigations of early developmental states may be of special interest if the aim is to study pre-symptomatic cases and test early therapeutic interventions in order to prevent development of a phenotype. However, the immature state of hiPSC-CMs does not resemble the state of myectomy tissues, which represent the end-stage of the disease (Helms et al., 2014; Nijenkamp et al., 2018). In the case of the newly created bi-allelic *MYBPC3* mutant cell line, which is supposed to mimic the severe and early-onset cardiomyopathy in newborns, the use of EHTs may be powerful as alterations were already expected without need of maturation. In the case of heterozygous *MYBPC3* patient-derived cell line, it is thus possible that some disease-specific phenotypic alterations may be potentially missed due to later disease development, which would not be detected in this model unless EHTs are maintained for a long period of time. In order to provoke a phenotype also in this heterozygous cell line, the EHTs were exposed to different stress conditions that might promote maturation such as electrical pacing and β-adrenergic stimulation with isoprenaline.

Nevertheless, it must be taken into account how heterogeneous cardiomyopathies are and the focus of this study was therefore to elucidate mutation specific alterations compared to isogenic controls.

4.3 Assessing the phenotype in HCM patient-derived hiPSC-CMs

4.3.1 Phenotype in human tissue and 2D culture of hiPSC-CMs

Before investigating the *in vitro* phenotype of the implemented cell lines, the patient's mutation was first to be evaluated on molecular level in order to elucidate its role in pathogenesis. The study of Helms et al. (2014) provided fundamental insights into the correlation of different HCM mutations and their consequences on mRNA and protein levels. This study did include the septal myectomy of a patient carrying the same *MYBPC3* c.2308G>A mutation that we studied here and provided some remarkable findings. They reported that they neither found a nonsense transcript nor a truncated cMyBP-C, which they considered due to the prevailing hypothesis that it is a truncating mutation and the nonsense

transcript is degraded by the NMD. Using the hiPSC technology we investigated in this study whether NMD is involved in nonsense transcript regulation by treating hiPSC-CMs with puromycine, emetine and CHX. These drugs are known to effectively inhibit the NMD and therefore prevent the degradation of nonsense mRNAs (Kosmidis et al., 2016; Vignier et al., 2009). As expected, the nonsense transcript was efficiently stabilised. Sanger sequencing revealed a 298-bp intronic retention followed by a frameshift and a PTC in exon 24. Hence, this provided first evidence for the molecular consequence of this specific mutation, showing that it is not leading to exon skipping as supposed from its localisation at a splice donor sequence, but rather to intronic retention. This was different to the observation done in the *Mybpc3*-targeted knock-in mice carrying a G>A transition on the last nucleotide of exon 6 generated some years ago by the Carrier's group (Vignier et al., 2009). In this mice, three different mutant transcripts were produced due to this nucleotide exchange with one being the skipping of exon 6, one deletion/insertion with subsequent partial retention of intron 8 together with skipping of exon 6 and one missense variant. Nonetheless, retention of the adjacent intron of the mutation site was not found. Altogether, the molecular consequences of a mutation on the last nucleotide of an exon appears to be different depending on the locus and species analysed. Therefore, it can be concluded that mutation-specific consequences exist and should be ruled out in every single case.

As opposed to the findings of Helms et al. (2014), the nonsense transcript was also identified in the myectomy tissue, although the presence of a band revealing the mutant transcript in the tissue was only detectable to a very low amount (Figure 14). Yet, the mutant transcript seems to be efficiently degraded in the adult heart tissue, suggesting a highly active NMD in this late stage of disease. In contrast, in the hiPSC-CMs the nonsense transcript was even visible without inhibiting the NMD (DMSO sample, Figure 16), although to a lower extent than in the treated CMs. In the latter, mutant transcripts reflected 17.6% of total transcripts after treatment, which is in line with the assumption of a 1:5 ratio of mutant to wild-type transcripts for truncating *MYBPC3* mutations (Helms et al., 2014). This supports the hypothesis of allelic imbalance for this mutation. Furthermore, it shows that the NMD is the underlying mechanism of degradation of the mutant transcript and that it could be specifically and effectively inhibited (Figure 16). Moreover, it can be concluded that the NMD is not as efficient in the hiPSC-CMs as it is in the adult tissue, suggesting underdevelopment and immaturity of these cells. In line with this hypothesis, the potential nonsense transcript was also detected in the bi-allelic *MYBPC3* hiPSC-CMs, when analysing gene therapy replacement (Mut#103 NT sample, Figure 32C). The fact that truncated cMyBP-C is not detected by Western blot in these CMs despite the presence of nonsense transcripts suggests the involvement of other safety mechanisms protecting the cell from poisoning

peptides. These are likely the UPS and the ALP or impairment of the translation (Mearini et al., 2008; Zech et al., 2019).

Analysis on protein level showed that truncated cMyBP-C is neither detected in the heterozygous nor in the bi-allelic *MYBPC3* hiPSC-CMs. This finding is in line with previous reports showing that truncated cMyBP-C was never found in patient's tissue or *MYBPC3*-hiPSC-CM models (Carrier et al., 2015; Helms et al., 2014; Seeger et al., 2019). Quantification of protein levels in the heterozygous hiPSC-CMs led to 30.6% calculated cMyBP-C levels as compared to its isogenic control. Although sample number was low, this hints towards haploinsufficiency. Haploinsufficiency is often reported as the major disease mechanism for truncating *MYBPC3* mutations in HCM (Carrier et al., 2015; Marston et al., 2012; Wijnker et al., 2016). This concept has been challenged by Helms et al. (2014) as well as very recently by Seeger et al. (2019). Interestingly, Seeger et al. (2019) created a homozygous hiPSC line using the same *MYBPC3* founder mutation as the introduced second mutation of the bi-allelic mutant (c.2827C>T) described here. Since this mutation creates a direct PTC, they also produced a knock-out of the *MYBPC3* gene. Due to their finding of reduced *MYBPC3* mutant transcripts but normal protein levels compared to isogenic controls, they claim that haploinsufficiency is not the mechanism of disease development in PTC-containing *MYBPC3* mutations causing HCM. Instead, they state it to be a chronic activation of the NMD. In contrast, Helms et al. (2014) proposed that haploinsufficiency might be present in early disease development and might be overcome at late stages of the disease, when compensated by the wild-type allele. This would be in line with the findings of the present hiPSC-CM model, which rather reflects early disease stages. Nevertheless, the true answer to this question, whether it is indeed haploinsufficiency or another mechanism, may not fully be answered here and should be subject to future studies.

One interesting observation that was validated with the present data is the finding that cMyBP-C is not necessary to build the sarcomere (Prondzynski et al., 2017; Seeger et al., 2019). Even in the complete absence of cMyBP-C such as in the bi-allelic mutant cell line, correct assembly of the sarcomere was observed as shown by proper localisation of α-actinin 2 at the Z-disk by immunofluorescence. This is in line with the findings of Carrier et al. (2004) and Wijnker et al. (2016) and the fact that *MYBPC3* knock-out mice are normally living although suffering from left ventricular hypertrophy (Marston et al., 2012).

4.3.2 Phenotype in EHTs

As hypercontractility, higher sensitivity towards external calcium and an increase in relaxation time are frequently reported findings in HCM, it was considered that these may be reflected in the phenotype of the EHTs (Eschenhagen and Carrier, 2019; Marston et al., 2012; Spudich, 2019; Stohr et al., 2013). Concerning force, no clear trend was found as reviewed recently by Eschenhagen and Carrier (2019). In this review, the authors summarised a number of typically reported parameters of HCM and DCM of 38 studies on the *in vitro* phenotype in hiPSC-CMs and outlined the general diversity of these parameters even among one clinical phenotype, either HCM or DCM.

First, generated forces and beating frequencies were compared among the different EHTs (isogenic control, heterozygous and bi-allelic *MYBPC3* mutants). The bi-allelic *MYBPC3* mutant EHTs exhibited lower force development with higher frequencies than the isogenic control EHTs. Interestingly, frequency was increased with the number of mutations in *MYBPC3* showing a gene-dose-dependent correlation. Of note, also in the study of Seeger et al. (2019) the full absence of cMyBP-C in EHTs led to impaired force development well fitting with the findings presented here.

Second, higher sensitivity towards external calcium was not found in the diseased hiPSC-EHTs. Indeed, it was the contrary. The bi-allelic mutant as well as the heterozygous *MYBPC3* hiPSC-EHTs had a higher sensitivity towards external calcium, which can be related to the respective maximum forces of the cell lines. Interestingly, Marian and Braunwald (2017) recently reported that higher calcium sensitivity is rather related to mutations of thin filament components, whereas mutations in thick-filament-associated proteins, such as β-MHC (β-myosin heavy chain) and cMyBP-C, are reported to cause decreased calcium sensitivity. In general, EC_{50} values of external calcium concentrations are not systematically investigated in hiPSC-CMs to date. A study from Mannhardt et al. (2016) reported 0.6 mM calcium as the concentration leading to half maximal forces in hiPSC-CMs derived from a healthy control cell line. Nevertheless, unpublished data from the institute also suggested a variability of this parameter among different healthy control hiPSC-CM lines. The EC_{50} values for calcium of the isogenic controls in the present study were 0.44 mM and 0.53 mM, which is closer to 0.6 mM than what was found in the heterozygous line (0.88 mM) and the bi allelic mutant (1.1 mM). Yet, in the heterozygous and bi-allelic mutant lines this value resulted only from EHTs of one differentiation batch, and lower sensitivity towards external calcium suggests more a DCM phenotype, which is still of interest as the aim was to model severe cardiomyopathies in general. Still, additional measurements of the relation between force and intracellular calcium in skinned

(= perforated sarcolemma) EHTs with the use of the Aurora system as done by Prondzynski et al. (2019a) could be performed in future studies to validate this finding. Furthermore, a deeper analysis on calcium handling should be conducted in the future as the study of Seeger et al. (2019) showed abnormal calcium signalling in their homozygous cell line, and we observed here destructive morphologic changes after exposure to high [Ca^{2+}] in the EHTs of the bi-allelic mutant.

Third, the relaxation time measured from peak height to 20% of baseline ($T2_{20\%}$) did not show prolongation as expected for HCM. Instead, faster contraction times ($T1_{20\%}$) in the bi-allelic *MYBPC3* mutant were found as opposed to the other genotype. This finding could instead be explained by a hypercontractile behaviour of the severe cell line regarding frequency, which is a typical feature of HCM (Spudich, 2019; Stohr et al., 2013).

Fourth, the isoprenaline and carbachol treatment experiments showed interesting differences between the bi-allelic mutant and the two other genotypes. When confronted with isoprenaline, the EHTs, with the exception of the cMyBP-C knock-out EHTs, recapitulated basic behaviour, namely positive inotropic effects and positive chronotropic effects as previously reported for control EHTs (Mannhardt et al., 2016). Only in the bi-allelic mutant, the addition of isoprenaline to the EC_{50} for calcium was not able to recover the force to its initial level at baseline, although it must have been more facile to recover the force since it was not even decreased to 50% as expected in the calculated EC_{50} for calcium. Moreover, no positive chronotropic effect was seen for this cell line, which was different from what was observed for the isogenic controls and heterozygous cell line and what is expected after isoprenaline treatment. This could be either explained by the preexisting high beating rate of the bi-allelic *MYBPC3* mutant EHTs at baseline that could not be increased further or by an issue of the CMs to handle isoprenaline because of failed phosphorylation of the motif region due to absence of cMyBP-C. Altogether and apparently, the cMyBP-C knock-out EHTs are not able to handle isoprenaline as the other groups. On the one hand, the lack of positive inotropic and chronotropic responses under β-adrenergic stimulation with isoprenaline suggests a key role of cMyBP-C phosphorylation for these parameters. On the other hand, treatment with carbachol led to partial antagonism of isoprenaline in all three genotype as expected (Mannhardt et al., 2016).

Of note, the following conclusions can be drawn concerning the EHT data. (1) The two isogenic controls, which resulted from two independent CRISPR clones, behaved similarly in most respects, suggesting that the observed effects truly relied on the repair of the mutation. (2) The heterozygous *MYBPC3* cell line did not show a clear HCM phenotype, which can be explained by the fact that the disease onset is expected to be late in

heterozygotes, whereas hiPSC-CMs are more suitable for modelling early disease states. (3) The bi-allelic *MYBPC3* mutant shows several alterations, namely reduced force, increased frequencies as well as impaired response to β-adrenergic stimulation. Since this cell line is supposed to mimic severe cardiomyopathies in general, as seen in the affected infants, it is at the end not important if the disease phenotype are more HCM or DCM oriented as it should model a grave cardiomyopathy phenotype.

4.4 Treatment implications based on hiPSCs *in vitro* model

In vitro experiments are necessary in order to investigate disease mechanisms. In the development of new treatment options for certain diseases, important insights are gained in these models, which are evaluated together with the findings of *in vivo* experiments in small animal models. Subsequently, these may evolve into further experiments in larger animal models followed by clinical trials. For children born with severe cardiomyopathy associated to bi-allelic truncating *MYBPC3* mutations, new treatment options are urgently needed since the only option to date is the rare heart transplantation. Hence, *MYBPC3* gene therapy is very attractive since it targets the effect of the disease-causing mutations itself, i.e. the absence of cMyBP-C protein (Prondzynski et al., 2019b).

Mearini et al. (2014) showed that gene therapy in neonatal homozygous *Mybpc3*-targeted knock-in (KI) mice partially prevented the development of cardiac hypertrophy. These KI mice mimicked the neonatal cardiomyopathy found in affected infants with bi-allelic truncating *MYBPC3* mutations. Goal of the present study was to show the feasibility of gene therapy in the hiPSC-CMs fully depleted of cMyBP-C, which would accomplish proof-of-principle for the bi-allelic mutant state. As gene therapy strategy, the gene replacement approach was chosen since haploinsufficiency is regarded as the main disease mechanism of truncating *MYBPC3* mutations (Carrier et al., 2015; Marston et al., 2012; Wijnker et al., 2016). As vector for delivery an AAV was used to transport the full-length *MYBPC3* cDNA as AAVs are able to transduce differentiated cells and due to other reasons described above (cf. 1.6). Eventually, we showed that exogenous *MYBPC3* is expressed in both heterozygous and compound heterozygous CMs (Figure 32). Furthermore, exogenous cMyBP-C is incorporated into the sarcomere as proved by the typical formation of doublets by immunofluorescence (Figure 38). These data support *MYBPC3* gene therapy in hiPSC-CMs with heterozygous *MYBPC3* mutation confirming a previous study from the group (Prondzynski et al., 2017). Furthermore and most importantly, it shows proof-of-principle for gene replacement therapy even in the bi-allelic state of truncating *MYBPC3* mutations *in vitro*.

AAVs show tissues and host-specific differences regarding tropism (Chamberlain et al., 2017). In the case of the *in vitro* experiments presented here, an AAV serotype 6 was chosen due to knowledge gained previously in the institute (data not shown). For *in vivo* murine studies AAV serotype 9 was shown to be most efficient in transducing CMs, but knowledge about the optimal serotype for hiPSC-CMs as well as the optimal gene transfer method in humans is still ongoing (Chamberlain et al., 2017; Prondzynski et al., 2019b). The question, how the gene therapy product can be efficiently and exclusively delivered to the heart, is potentially the most demanding obstacle when dealing with the clinical translation (Chamberlain et al., 2017). In the present work, a MOI of 10,000 has been used resulting in a transduction efficiency of hiPSC-CMs of more than 80% perfectly matching results previously published by the group (Prondzynski et al., 2017). Nevertheless, in the future when gene therapy would be conducted in humans, the dose that is sufficient to rescue disease development has to be determined for the specific gene therapy medicinal product.

The molecular effect of gene replacement was evaluated at protein level. AAV6-mediated transduction of exogenous *MYBPC3* led to 21.6% of cMyBP-C levels in the bi-allelic mutant related to the isogenic control hiPSC-CMs. In the heterozygous cell line, protein levels led to controversial findings, which was probably caused by the low sample number (Figure 34). Interestingly, the highest amount of exogenous cMyBP-C was found in the isogenic control as compared to the heterozygous and bi-allelic mutant cell line (Figure 34 and Figure 36). A possible explanation would be that the protein turnover in the defined stoichiometry of the cardiac sarcomere is operating different in the wild-type and the MOI is not sufficient for the diseased cell line to refill the missing cMyBP-C in the bi-allelic mutant hiPSC-CMs. Indeed, in the immunofluorescence images not all CMs were transduced and the FLAG signal was patchy in the latter. Hence, the amount of exogenous cMyBP-C was inversely correlated to the number of mutations with 43.9% in the heterozygous cell line and 18.9% in the bi-allelic mutant. If so, this observation would limit the efficacy of gene replacement therapy, although this has to be further evaluated and more batches are needed. Despite low amount of exogenous cMyBP-C, the protein was properly localised in the sarcomere, suggesting also correct function (Figure 38).

In terms of cell size as an important hallmark of HCM, we could show a significant reduction in the heterozygous hiPSC-CMs after gene replacement therapy (cf. 3.5.4). This emphasises that cell size may be an important aspect of the phenotype in these cells and that cell size may be accessible for gene replacement therapy. This is in line with previous findings from the group (Prondzynski et al., 2017; Prondzynski et al., 2019a).

Nevertheless, as gene therapy experiments were solely performed in 2D culture and not yet in EHTs, conclusions concerning functional improvements are only speculations. Assessing the phenotype after gene therapy in 3D EHTs would allow to draw conclusions concerning functionality in future studies.

The present data show that gene therapy might be a promising option for infants showing severe cardiomyopathy due to bi-allelic *MYBPC3* mutations, although these data are preliminary and future experiments need to show efficiency and feasibility *in vivo*. Currently, a group in Munich works in implementing disease modelling in pigs (Klymiuk et al., 2016). In collaboration with Lucie Carrier, one goal is to establish *MYBPC3* gene therapy in this porcine model in addition to the other models mentioned.

One important question that still needs to be answered in future studies is whether gene therapy would be able to rescue the disease phenotype, even prevent the occurrence of the disease, e.g. in the heterozygous population with later onset of the disease, or whether it might only improve the outcome and phenotype of the patients, which already presented with the typical symptoms.

4.5 Future perspectives and conclusion

The present study has provided several insights into biology of hiPSC-CMs in monolayer and EHTs generated from three genotypically different but related hiPSC lines, namely a heterozygous *MYBPC3* line derived from an HCM patient, a bi-allelic mutant and isogenic controls created by CRISPR/Cas9. Nevertheless, the number of independent differentiation batches per cell line remained low and needs to be increased in future experiments to validate the findings.

To date, only one previous study exists that models the mutation in exon 27 (c.2827C>T) of the bi-allelic mutant. In this study from Seeger et al. (2019) starting from heterozygous *MYBPC3* patient-derived iPSCs an homozygous and the isogenic control have been created by CRISPR/Cas9 gene editing. So far, no study with hiPSC-CMs investigating the mutation in exon 23 (c.2308G>A) has been published. Hence, additional studies and particularly more differentiation batches are required to verify or falsify, what has been described here concerning the consequences of these mutations.

Besides, an expanded analysis should be done in different aspects. On the one hand, fundamental analysis using omic technologies, i.e. genomics, transcriptomics, e.g. RNAseq technologies, proteomics, e.g. mass spectrometry, and metabolomics is needed

prospectively (Bayes-Genis et al., 2020; Cyganek et al., 2018). On the other hand, morphologic and functional assessment should be extended. Morphologically, it would be of interest to deeper investigate cell size as hypertrophy marker and myocardial disarray, as these are frequently reported hallmarks of HCM (Eschenhagen and Carrier, 2019; Marian and Braunwald, 2017; Prondzynski et al., 2019a). Functionally, further experiments in EHTs with increased numbers of biological and technical replicates are needed. Moreover, electrophysiologic data may be added such as measuring the action potential durations (APDs) with sharp micro-electrodes or the ion channel current via the patch clamp technique (Lemoine et al., 2017; Prondzynski et al., 2019a). To strengthen the data, it might be of interest as well to validate the findings in an unrelated healthy control hiPSC line, where the mutations of interest are introduced by CRISPR/Cas9. Mutation-specific alterations would be underlined with this method. Improvements in high-throughput genome editing and cardiac differentiation, higher standardised experimental procedures, EHT generation and culture as well as CM maturation will allow facilitated phenotypic screening in the future.

Furthermore, developments in precision medicine, meaning deduction of individual treatment implications due to the *in vitro* experiments, will increasingly be in the focus in the future since the hiPSC technology and CRISPR/Cas9 opened new opportunities in this respect. Using this technique for precision medicine was recently succesfully shown by Ma et al. (2018) and Prondzynski et al. (2019a).

Hence, the following conclusion can be made. As HCM/DCM phenotypes are so diversely and controversially reported in the hiPSC models and vary among and in comparison to animal models, this outlines the need for isogenic controls (Eschenhagen and Carrier, 2019). Investigations under isogenic conditions lead the focus into another direction, namely that especially mutation specific alterations may potentially be investigated in this model.

5 Summary

Cardiomyopathies are cardiac genetic diseases, leading to heart failure and sudden cardiac death even among young people. One of the most important genes affected is the *MYBPC3* gene, encoding cardiac myosin-binding protein-C (cMyBP-C). Bi-allelic truncating mutations - homozygous or compound heterozygous - are very severe and cause death of infants in the first year of life. Up to now there is no disease curing treatment other than heart transplant. Therefore, the aim of this thesis was to analyse the effect of bi-allelic truncating *MYBPC3* mutations, which mimic the genetic of infants with a severe course of disease, in human-induced pluripotent stem cell-derived cardiomyocytes (hiPSC-CMs) in 2D and 3D engineered heart tissues (EHTs) and test *MYBPC3* gene replacement therapy.

HiPSCs (CMS32) were reprogrammed from a female patient with hypertrophic cardiomyopathy (HCM) who carried a heterozygous mutation in *MYBPC3* (c.2308G>A). The mutation is located on the last nucleotide of exon 23, which belongs to the highly conserved 5' donor splice site sequence. Consequently, it is considered as a truncating mutation. To detect the nonsense mRNA, CMS32-hiPSCs were differentiated into cardiomyocytes (CMs) and treated with drugs inhibiting the nonsense-mediated mRNA decay (NMD), which stabilised the nonsense mRNA that is normally degraded by this safety control mechanism. Sequencing identified a nonsense mRNA with a 298-bp retention of intron 23 and therefore a frameshift followed by a premature termination codon (PTC; Asp770Serfs98X).

Furthermore, the CMS32 cell line was used to repair the existing mutation (isogenic control) and to introduce a Dutch founder mutation (c.2827C>T, p.Arg943X) with the CRISPR/Cas9 genome editing to mimic the genetic situation of the affected children (bi-allelic truncating mutant). Sequencing revealed that 6/41 CRISPR clones were corrected and 6/93 CRISPR clones harboured the second mutation in heterozygous or homozygous state. Four of the repaired cell lines were expanded to a master cell bank (MCB) as well as one bi-allelic clone with homozygous founder mutation. The MCBs were checked for hiPSC quality markers and for the absence of the top 10 *in silico* predicted off-targets. HiPSC lines were then differentiated into CMs for further experiments.

Analysis on protein level by Western blot validated the functional cMyBP-C knock-out in the bi-allelic mutant hiPSC-CMs. Besides, truncated cMyBP-C was not detected, neither in the bi-allelic mutant nor in CMS32-CMs. In the latter, cMyBP-C levels were lower (30.6%) than in the isogenic control. Furthermore, functional analysis in EHTs revealed a markedly lower force development and a higher beating frequency in the bi-allelic mutant than in the other

genotypes. In addition, β-adrenergic stimulation with isoprenaline did not lead to full recovery of force (inotropic response) and frequency (chronotropic response) in bi-allelic mutant in contrast to the heterozygous mutant and repaired EHTs.

Finally, the three hiPSC-CM lines were transduced (multiplicity of infection: 10,000) with an adeno-associated virus serotype 6 carrying the wild-type *MYBPC3* cDNA as gene therapy to replace the missing protein as haploinsufficiency was considered the disease mechanism. Qualitative PCR, Western blot and immunofluorescence analysis showed that exogenous *MYBPC3* is expressed, and cMyBP-C protein is well incorporated in transduced cells and led to a reduction of cell size in the heterozygous state, which provided proof-of-principle of gene replacement therapy in hiPSC-CMs *in vitro*.

6 Zusammenfassung

Kardiomyopathien sind genetische Herzerkrankungen, die zu Herzinsuffizienz und plötzlichem Herztod bei jungen Menschen führen können. Eines der wichtigsten beteiligten Gene ist das *MYBPC3*-Gen, welches für das kardiale Myosin-bindende Protein C (cMyBP-C) kodiert. Biallelische trunkierende Mutationen - homozygot oder komplex heterozygot - sind besonders schwerwiegend und führen innerhalb des ersten Lebensjahres zum Tod der betroffenen Kinder. Bisher gibt es keine kausale Therapie außer der Herztransplantation. Daher war es das Ziel dieser Doktorarbeit, die Auswirkung von biallelischen trunkierenden *MYBPC3*-Mutationen, welche die Genetik der Kinder mit schwerem Krankheitsverlauf modellieren, in humanen induzierten pluripotenten Stammzell (hiPSC)-abgeleiteten Kardiomyozyten in 2D-Zellkultur und 3D künstlichen Herzgeweben (EHTs) zu untersuchen und eine *MYBPC3*-Genersatztherapie zu testen.

Die humanen iPSCs (CMS32) stammten von einer Patientin mit hypertropher Kardiomyopathie, bei der eine heterozygote Genmutation im *MYBPC3*-Gen (c.2308G>A) festgestellt wurde. Diese Mutation liegt auf dem letzten Nukleotid des Exons 23, welches zur hoch konservierten 5‘ Donor-Spleißstellen-Sequenz gehört. Infolgedessen wird es für eine trunkierende Mutation gehalten. Um die Nonsense-mRNA nachzuweisen, wurden die CMS32-hiPSCs zu Kardiomyozyten differenziert und mit pharmakologischen Substanzen behandelt, welche den Nonsense-vermittelten mRNA Abbau (NMD) inhibieren. Hierdurch wurde die Nonsense-mRNA stabilisiert, die normalerweise von diesem Sicherheits-Kontrollmechanismus abgebaut wird. Durch Sequenzierung konnte daraufhin eine Nonsense-mRNA mit einer 298 bp-langen Retention von Intron 23 identifiziert werden. Diese führte zu einem Frameshift gefolgt von einem vorzeitigen Stopcodon (Asp770Serfs98X).

Darüber hinaus wurde die CMS32-Zelllinie dazu genutzt, die vorliegende Mutation mit Hilfe der CRISPR/Cas9 Geneditierungsmethode zu reparieren (isogene Kontrolle) sowie eine niederländische Gründermutation (c.2827C>T, p.Arg943X) einzubringen, um die genetische Situation betroffener Kinder nachzuahmen (biallelisch trunkierend). In der Sequenzierung zeigte sich, dass 6 von 41 CRISPR-Klonen repariert wurden und 6 von 93 CRISPR-Klonen die zweite Mutation heterozygot oder homozygot beinhalteten. Vier der reparierten Zellklone sowie ein biallelischer Klon mit der homozygoten Gründermutation wurden zu einer Master-Zell-Bank (MCB) expandiert. Die MCBs wurden auf hiPSC-Qualitätskriterien hin geprüft und die Top 10 der *in silico*-ermittelten Off-targets wurden ausgeschlossen. Die hiPSC-Linien wurden daraufhin für weitere Experimente zu Kardiomyozyten differenziert.

Die Analyse auf Proteinebene mittels Western Blot bestätigte den funktionellen cMyBP-C-Knockout in den biallelisch mutierten hiPSC-CMs. Des Weiteren zeigte sich, dass trunkiertes cMyBP-C weder in der biallelisch mutierten Zelllinie noch in der CMS32-Zelllinie gefunden werden konnte. In letzterer waren die cMyBP-C-Spiegel geringer (30,6%) als in der isogenen Kontrolle. Ferner zeigte sich in der funktionellen Analyse der EHTs eine deutlich geringere Kraftentwicklung und eine höhere Schlagfrequenz in der biallelisch mutierten Zelllinie als in den anderen Genotypen. Im Gegensatz zu den heterozygoten und reparierten EHTs führte eine β-adrenerge Stimulation mit Isoprenalin nicht zu einer vollständigen Wiederherstellung der Kraft (inotroper Effekt) und Frequenz (chronotroper Effekt) in den biallelisch mutierten EHTs.

Zu guter Letzt wurden die drei hiPSC-Kardiomyozytenlinien mit einem Adeno-assoziierten Virus des Serotyps 6 transduziert (Multiplizität der Infektion: 10.000). Dieser trug die Wildtyp *MYBPC3*-cDNA-Sequenz, um als Gentherapie das fehlende Protein zu ersetzen, da Haploinsuffizienz als ursächlicher Krankheitsmechanismus anzusehen war. Eine qualitative Polymerase-Kettenreaktion, Western Blot sowie eine Immunfluoreszenz-Analyse zeigten, dass das exogene *MYBPC3* in den transduzierten Zellen exprimiert und cMyBP-C korrekt eingebaut wurde und zu einer Reduktion der Zellgröße in den heterozygoten Kardiomyozyten führte. Damit konnte der Nachweis hinsichtlich der prinzipiellen Durchführbarkeit der Genersatztherapie in hiPSC Kardiomyozyten *in vitro* erbracht werden.

7 References

AMOASII, L., HILDYARD, J. C. W., LI, H., SANCHEZ-ORTIZ, E., MIREAULT, A., CABALLERO, D., HARRON, R., STATHOPOULOU, T. R., MASSEY, C., SHELTON, J. M., BASSEL-DUBY, R., PIERCY, R. J. & OLSON, E. N. 2018. Gene editing restores dystrophin expression in a canine model of Duchenne muscular dystrophy. *Science,* 362**,** 86-91.

AMOASII, L., LONG, C., LI, H., MIREAULT, A. A., SHELTON, J. M., SANCHEZ-ORTIZ, E., MCANALLY, J. R., BHATTACHARYYA, S., SCHMIDT, F., GRIMM, D., HAUSCHKA, S. D., BASSEL-DUBY, R. & OLSON, E. N. 2017. Single-cut genome editing restores dystrophin expression in a new mouse model of muscular dystrophy. *Sci Transl Med,* 9.

BATALOV, I. & FEINBERG, A. W. 2015. Differentiation of Cardiomyocytes from Human Pluripotent Stem Cells Using Monolayer Culture. *Biomark Insights,* 10**,** 71-6.

BAYES-GENIS, A., LIU, P. P., LANFEAR, D. E., DE BOER, R. A., GONZALEZ, A., THUM, T., EMDIN, M. & JANUZZI, J. L. 2020. Omics phenotyping in heart failure: the next frontier. *Eur Heart J,* 41**,** 3477-3484.

BEDADA, F. B., WHEELWRIGHT, M. & METZGER, J. M. 2016. Maturation status of sarcomere structure and function in human iPSC-derived cardiac myocytes. *Biochim Biophys Acta,* 1863**,** 1829-38.

BEHRENS-GAWLIK, V., MEARINI, G., GEDICKE-HORNUNG, C., RICHARD, P. & CARRIER, L. 2014. MYBPC3 in hypertrophic cardiomyopathy: from mutation identification to RNA-based correction. *Pflugers Arch,* 466**,** 215-23.

BRANDAO, K. O., TABEL, V. A., ATSMA, D. E., MUMMERY, C. L. & DAVIS, R. P. 2017. Human pluripotent stem cell models of cardiac disease: from mechanisms to therapies. *Dis Model Mech,* 10**,** 1039-1059.

BRAUNWALD, E. 2017. Cardiomyopathies: An Overview. *Circ Res,* 121**,** 711-721.

BRECKWOLDT, K., LETUFFE-BRENIERE, D., MANNHARDT, I., SCHULZE, T., ULMER, B., WERNER, T., BENZIN, A., KLAMPE, B., REINSCH, M. C., LAUFER, S., SHIBAMIYA, A., PRONDZYNSKI, M., MEARINI, G., SCHADE, D., FUCHS, S., NEUBER, C., KRAMER, E., SALEEM, U., SCHULZE, M. L., RODRIGUEZ, M. L., ESCHENHAGEN, T. & HANSEN, A. 2017. Differentiation of cardiomyocytes and generation of human engineered heart tissue. *Nat Protoc,* 12**,** 1177-1197.

BURKE, M. A., COOK, S. A., SEIDMAN, J. G. & SEIDMAN, C. E. 2016. Clinical and Mechanistic Insights Into the Genetics of Cardiomyopathy. *J Am Coll Cardiol,* 68**,** 2871-2886.

BURRIDGE, P. W. & ZAMBIDIS, E. T. 2013. Highly efficient directed differentiation of human induced pluripotent stem cells into cardiomyocytes. *Methods Mol Biol,* 997**,** 149-61.

CARRIER, L. 2020. Targeting the population for gene therapy with MYBPC3. *J Mol Cell Cardiol*.

CARRIER, L., BONNE, G., BAHREND, E., YU, B., RICHARD, P., NIEL, F., HAINQUE, B., CRUAUD, C., GARY, F., LABEIT, S., BOUHOUR, J. B., DUBOURG, O., DESNOS, M., HAGEGE, A. A., TRENT, R. J., KOMAJDA, M., FISZMAN, M. & SCHWARTZ, K. 1997. Organization and sequence of human cardiac myosin binding protein C gene (MYBPC3) and identification of mutations predicted to produce truncated proteins in familial hypertrophic cardiomyopathy. *Circ Res,* 80**,** 427-34.

CARRIER, L., KNOLL, R., VIGNIER, N., KELLER, D. I., BAUSERO, P., PRUDHON, B., ISNARD, R., AMBROISINE, M. L., FISZMAN, M., ROSS, J., JR., SCHWARTZ, K. & CHIEN, K. R. 2004. Asymmetric septal hypertrophy in heterozygous cMyBP-C null mice. *Cardiovasc Res,* 63**,** 293-304.

CARRIER, L., MEARINI, G., STATHOPOULOU, K. & CUELLO, F. 2015. Cardiac myosin-binding protein C (MYBPC3) in cardiac pathophysiology. *Gene,* 573**,** 188-97.

CHAMBERLAIN, K., RIYAD, J. M. & WEBER, T. 2017. Cardiac gene therapy with adeno-associated virus-based vectors. *Curr Opin Cardiol*.
CYGANEK, L., TIBURCY, M., SEKERES, K., GERSTENBERG, K., BOHNENBERGER, H., LENZ, C., HENZE, S., STAUSKE, M., SALINAS, G., ZIMMERMANN, W. H., HASENFUSS, G. & GUAN, K. 2018. Deep phenotyping of human induced pluripotent stem cell-derived atrial and ventricular cardiomyocytes. *JCI Insight,* 3.
DEVALLA, H. D. & PASSIER, R. 2018. Cardiac differentiation of pluripotent stem cells and implications for modeling the heart in health and disease. *Sci Transl Med,* 10.
DOUDNA, J. A. & CHARPENTIER, E. 2014. Genome editing. The new frontier of genome engineering with CRISPR-Cas9. *Science,* 346**,** 1258096.
EDER, A., VOLLERT, I., HANSEN, A. & ESCHENHAGEN, T. 2016. Human engineered heart tissue as a model system for drug testing. *Adv Drug Deliv Rev,* 96**,** 214-24.
EGLI, D., ZUCCARO, M. V., KOSICKI, M., CHURCH, G. M., BRADLEY, A. & JASIN, M. 2018. Inter-homologue repair in fertilized human eggs? *Nature,* 560**,** E5-E7.
ESCHENHAGEN, T. & CARRIER, L. 2019. Cardiomyopathy phenotypes in human-induced pluripotent stem cell-derived cardiomyocytes-a systematic review. *Pflugers Arch,* 471**,** 755-768.
ESCHENHAGEN, T., FINK, C., REMMERS, U., SCHOLZ, H., WATTCHOW, J., WEIL, J., ZIMMERMANN, W., DOHMEN, H. H., SCHAFER, H., BISHOPRIC, N., WAKATSUKI, T. & ELSON, E. L. 1997. Three-dimensional reconstitution of embryonic cardiomyocytes in a collagen matrix: a new heart muscle model system. *FASEB J,* 11**,** 683-94.
ESCHENHAGEN, T., MUMMERY, C. & KNOLLMANN, B. C. 2015. Modelling sarcomeric cardiomyopathies in the dish: from human heart samples to iPSC cardiomyocytes. *Cardiovasc Res,* 105**,** 424-38.
FERIC, N. T. & RADISIC, M. 2016. Maturing human pluripotent stem cell-derived cardiomyocytes in human engineered cardiac tissues. *Adv Drug Deliv Rev,* 96**,** 110-34.
FU, Y., FODEN, J. A., KHAYTER, C., MAEDER, M. L., REYON, D., JOUNG, J. K. & SANDER, J. D. 2013. High-frequency off-target mutagenesis induced by CRISPR-Cas nucleases in human cells. *Nat Biotechnol,* 31**,** 822-6.
FUSAKI, N., BAN, H., NISHIYAMA, A., SAEKI, K. & HASEGAWA, M. 2009. Efficient induction of transgene-free human pluripotent stem cells using a vector based on Sendai virus, an RNA virus that does not integrate into the host genome. *Proc Jpn Acad Ser B Phys Biol Sci,* 85**,** 348-62.
GALLI, F., BRAGG, L., MEGGIOLARO, L., ROSSI, M., CAFFARINI, M., NAZ, N., SANTOLERI, S. & COSSU, G. 2018. Gene and Cell Therapy for Muscular Dystrophies: Are We Getting There? *Hum Gene Ther,* 29**,** 1098-1105.
HANSEN, A., EDER, A., BONSTRUP, M., FLATO, M., MEWE, M., SCHAAF, S., AKSEHIRLIOGLU, B., SCHWOERER, A. P., UEBELER, J. & ESCHENHAGEN, T. 2010. Development of a drug screening platform based on engineered heart tissue. *Circ Res,* 107**,** 35-44.
HARVEY, P. A. & LEINWAND, L. A. 2011. The cell biology of disease: cellular mechanisms of cardiomyopathy. *J Cell Biol,* 194**,** 355-65.
HATTORI, F., CHEN, H., YAMASHITA, H., TOHYAMA, S., SATOH, Y. S., YUASA, S., LI, W., YAMAKAWA, H., TANAKA, T., ONITSUKA, T., SHIMOJI, K., OHNO, Y., EGASHIRA, T., KANEDA, R., MURATA, M., HIDAKA, K., MORISAKI, T., SASAKI, E., SUZUKI, T., SANO, M., MAKINO, S., OIKAWA, S. & FUKUDA, K. 2010. Nongenetic method for purifying stem cell-derived cardiomyocytes. *Nat Methods,* 7**,** 61-6.
HELMS, A. S., DAVIS, F. M., COLEMAN, D., BARTOLONE, S. N., GLAZIER, A. A., PAGANI, F., YOB, J. M., SADAYAPPAN, S., PEDERSEN, E., LYONS, R., WESTFALL, M. V., JONES, R., RUSSELL, M. W. & DAY, S. M. 2014. Sarcomere mutation-specific expression patterns in human hypertrophic cardiomyopathy. *Circ Cardiovasc Genet,* 7**,** 434-43.

HIRT, M. N., BOEDDINGHAUS, J., MITCHELL, A., SCHAAF, S., BORNCHEN, C., MULLER, C., SCHULZ, H., HUBNER, N., STENZIG, J., STOEHR, A., NEUBER, C., EDER, A., LUTHER, P. K., HANSEN, A. & ESCHENHAGEN, T. 2014. Functional improvement and maturation of rat and human engineered heart tissue by chronic electrical stimulation. *J Mol Cell Cardiol,* 74**,** 151-61.

HOCKEMEYER, D. & JAENISCH, R. 2016. Induced Pluripotent Stem Cells Meet Genome Editing. *Cell Stem Cell,* 18**,** 573-86.

HU, J. H., MILLER, S. M., GEURTS, M. H., TANG, W., CHEN, L., SUN, N., ZEINA, C. M., GAO, X., REES, H. A., LIN, Z. & LIU, D. R. 2018. Evolved Cas9 variants with broad PAM compatibility and high DNA specificity. *Nature,* 556**,** 57-63.

JACOBI, A. M., RETTIG, G. R., TURK, R., COLLINGWOOD, M. A., ZEINER, S. A., QUADROS, R. M., HARMS, D. W., BONTHUIS, P. J., GREGG, C., OHTSUKA, M., GURUMURTHY, C. B. & BEHLKE, M. A. 2017. Simplified CRISPR tools for efficient genome editing and streamlined protocols for their delivery into mammalian cells and mouse zygotes. *Methods,* 121-122**,** 16-28.

JEZIOROWSKA, D., FONTAINE, V., JOUVE, C., VILLARD, E., DUSSAUD, S., AKBAR, D., LETANG, V., CERVELLO, P., ITIER, J. M., PRUNIAUX, M. P. & HULOT, J. S. 2017. Differential Sarcomere and Electrophysiological Maturation of Human iPSC-Derived Cardiac Myocytes in Monolayer vs. Aggregation-Based Differentiation Protocols. *Int J Mol Sci,* 18.

JINEK, M., CHYLINSKI, K., FONFARA, I., HAUER, M., DOUDNA, J. A. & CHARPENTIER, E. 2012. A programmable dual-RNA-guided DNA endonuclease in adaptive bacterial immunity. *Science,* 337**,** 816-21.

KATTMAN, S. J., WITTY, A. D., GAGLIARDI, M., DUBOIS, N. C., NIAPOUR, M., HOTTA, A., ELLIS, J. & KELLER, G. 2011. Stage-specific optimization of activin/nodal and BMP signaling promotes cardiac differentiation of mouse and human pluripotent stem cell lines. *Cell Stem Cell,* 8**,** 228-40.

KEMPF, H., KROPP, C., OLMER, R., MARTIN, U. & ZWEIGERDT, R. 2015. Cardiac differentiation of human pluripotent stem cells in scalable suspension culture. *Nat Protoc,* 10**,** 1345-61.

KHAN, J. M., LYON, A. R. & HARDING, S. E. 2013. The case for induced pluripotent stem cell-derived cardiomyocytes in pharmacological screening. *Br J Pharmacol,* 169**,** 304-17.

KILPINEN, H., GONCALVES, A., LEHA, A., AFZAL, V., ALASOO, K., ASHFORD, S., BALA, S., BENSADDEK, D., CASALE, F. P., CULLEY, O. J., DANECEK, P., FAULCONBRIDGE, A., HARRISON, P. W., KATHURIA, A., MCCARTHY, D., MCCARTHY, S. A., MELECKYTE, R., MEMARI, Y., MOENS, N., SOARES, F., MANN, A., STREETER, I., AGU, C. A., ALDERTON, A., NELSON, R., HARPER, S., PATEL, M., WHITE, A., PATEL, S. R., CLARKE, L., HALAI, R., KIRTON, C. M., KOLB-KOKOCINSKI, A., BEALES, P., BIRNEY, E., DANOVI, D., LAMOND, A. I., OUWEHAND, W. H., VALLIER, L., WATT, F. M., DURBIN, R., STEGLE, O. & GAFFNEY, D. J. 2017. Common genetic variation drives molecular heterogeneity in human iPSCs. *Nature,* 546**,** 370-375.

KIM, S., KIM, D., CHO, S. W., KIM, J. & KIM, J. S. 2014. Highly efficient RNA-guided genome editing in human cells via delivery of purified Cas9 ribonucleoproteins. *Genome Res,* 24**,** 1012-9.

KLYMIUK, N., SEELIGER, F., BOHLOOLY, Y. M., BLUTKE, A., RUDMANN, D. G. & WOLF, E. 2016. Tailored Pig Models for Preclinical Efficacy and Safety Testing of Targeted Therapies. *Toxicol Pathol,* 44**,** 346-57.

KOLOKOTRONIS, K., KUHNISCH, J., KLOPOCKI, E., DARTSCH, J., ROST, S., HUCULAK, C., MEARINI, G., STORK, S., CARRIER, L., KLAASSEN, S. & GERULL, B. 2019. Biallelic mutation in MYH7 and MYBPC3 leads to severe cardiomyopathy with left ventricular noncompaction phenotype. *Hum Mutat*.

KOSICKI, M., TOMBERG, K. & BRADLEY, A. 2018. Repair of double-strand breaks induced by CRISPR-Cas9 leads to large deletions and complex rearrangements. *Nat Biotechnol,* 36**,** 765-771.

KOSMIDIS, G., VEERMAN, C. C., CASINI, S., VERKERK, A. O., VAN DE PAS, S., BELLIN, M., WILDE, A. A., MUMMERY, C. L. & BEZZINA, C. R. 2016. Readthrough-Promoting Drugs Gentamicin and PTC124 Fail to Rescue Nav1.5 Function of Human-Induced Pluripotent Stem Cell-Derived Cardiomyocytes Carrying Nonsense Mutations in the Sodium Channel Gene SCN5A. *Circ Arrhythm Electrophysiol,* 9.

LAHTI, A. L., KUJALA, V. J., CHAPMAN, H., KOIVISTO, A. P., PEKKANEN-MATTILA, M., KERKELA, E., HYTTINEN, J., KONTULA, K., SWAN, H., CONKLIN, B. R., YAMANAKA, S., SILVENNOINEN, O. & AALTO-SETALA, K. 2012. Model for long QT syndrome type 2 using human iPS cells demonstrates arrhythmogenic characteristics in cell culture. *Dis Model Mech,* 5**,** 220-30.

LANDER, E. S. 2016. The Heroes of CRISPR. *Cell,* 164**,** 18-28.

LEMME, M., ULMER, B. M., LEMOINE, M. D., ZECH, A. T. L., FLENNER, F., RAVENS, U., REICHENSPURNER, H., ROL-GARCIA, M., SMITH, G., HANSEN, A., CHRIST, T. & ESCHENHAGEN, T. 2018. Atrial-like Engineered Heart Tissue: An In Vitro Model of the Human Atrium. *Stem Cell Reports,* 11**,** 1378-1390.

LEMOINE, M. D., MANNHARDT, I., BRECKWOLDT, K., PRONDZYNSKI, M., FLENNER, F., ULMER, B., HIRT, M. N., NEUBER, C., HORVATH, A., KLOTH, B., REICHENSPURNER, H., WILLEMS, S., HANSEN, A., ESCHENHAGEN, T. & CHRIST, T. 2017. Human iPSC-derived cardiomyocytes cultured in 3D engineered heart tissue show physiological upstroke velocity and sodium current density. *Sci Rep,* 7**,** 5464.

LIAN, X., HSIAO, C., WILSON, G., ZHU, K., HAZELTINE, L. B., AZARIN, S. M., RAVAL, K. K., ZHANG, J., KAMP, T. J. & PALECEK, S. P. 2012. Robust cardiomyocyte differentiation from human pluripotent stem cells via temporal modulation of canonical Wnt signaling. *Proc Natl Acad Sci U S A,* 109**,** E1848-57.

LIANG, X., POTTER, J., KUMAR, S., ZOU, Y., QUINTANILLA, R., SRIDHARAN, M., CARTE, J., CHEN, W., ROARK, N., RANGANATHAN, S., RAVINDER, N. & CHESNUT, J. D. 2015. Rapid and highly efficient mammalian cell engineering via Cas9 protein transfection. *J Biotechnol,* 208**,** 44-53.

MA, H., MARTI-GUTIERREZ, N., PARK, S. W., WU, J., LEE, Y., SUZUKI, K., KOSKI, A., JI, D., HAYAMA, T., AHMED, R., DARBY, H., VAN DYKEN, C., LI, Y., KANG, E., PARK, A. R., KIM, D., KIM, S. T., GONG, J., GU, Y., XU, X., BATTAGLIA, D., KRIEG, S. A., LEE, D. M., WU, D. H., WOLF, D. P., HEITNER, S. B., BELMONTE, J. C. I., AMATO, P., KIM, J. S., KAUL, S. & MITALIPOV, S. 2017. Correction of a pathogenic gene mutation in human embryos. *Nature,* 548**,** 413-419.

MA, N., ZHANG, J. Z., ITZHAKI, I., ZHANG, S. L., CHEN, H., HADDAD, F., KITANI, T., WILSON, K. D., TIAN, L., SHRESTHA, R., WU, H., LAM, C. K., SAYED, N. & WU, J. C. 2018. Determining the Pathogenicity of a Genomic Variant of Uncertain Significance Using CRISPR/Cas9 and Human-Induced Pluripotent Stem Cells. *Circulation,* 138**,** 2666-2681.

MAHMOOD, S. S., LEVY, D., VASAN, R. S. & WANG, T. J. 2014. The Framingham Heart Study and the epidemiology of cardiovascular disease: a historical perspective. *Lancet,* 383**,** 999-1008.

MANNHARDT, I., BRECKWOLDT, K., LETUFFE-BRENIERE, D., SCHAAF, S., SCHULZ, H., NEUBER, C., BENZIN, A., WERNER, T., EDER, A., SCHULZE, T., KLAMPE, B., CHRIST, T., HIRT, M. N., HUEBNER, N., MORETTI, A., ESCHENHAGEN, T. & HANSEN, A. 2016. Human Engineered Heart Tissue: Analysis of Contractile Force. *Stem Cell Reports,* 7**,** 29-42.

MANNHARDT, I., EDER, A., DUMOTIER, B., PRONDZYNSKI, M., KRAMER, E., TRAEBERT, M., SOHREN, K. D., FLENNER, F., STATHOPOULOU, K., LEMOINE, M. D., CARRIER, L., CHRIST, T., ESCHENHAGEN, T. & HANSEN, A.

2017. Blinded Contractility Analysis in hiPSC-Cardiomyocytes in Engineered Heart Tissue Format: Comparison With Human Atrial Trabeculae. *Toxicol Sci,* 158**,** 164-175.
MARIAN, A. J. & BRAUNWALD, E. 2017. Hypertrophic Cardiomyopathy: Genetics, Pathogenesis, Clinical Manifestations, Diagnosis, and Therapy. *Circ Res,* 121**,** 749-770.
MARON, B. J. 2002. Hypertrophic cardiomyopathy: a systematic review. *JAMA,* 287**,** 1308-20.
MARON, B. J., MARON, M. S. & SEMSARIAN, C. 2012. Double or compound sarcomere mutations in hypertrophic cardiomyopathy: a potential link to sudden death in the absence of conventional risk factors. *Heart Rhythm,* 9**,** 57-63.
MARSTON, S., COPELAND, O., GEHMLICH, K., SCHLOSSAREK, S. & CARRIER, L. 2012. How do MYBPC3 mutations cause hypertrophic cardiomyopathy? *J Muscle Res Cell Motil,* 33**,** 75-80.
MEARINI, G., SCHLOSSAREK, S., WILLIS, M. S. & CARRIER, L. 2008. The ubiquitin-proteasome system in cardiac dysfunction. *Biochim Biophys Acta,* 1782**,** 749-63.
MEARINI, G., STIMPEL, D., GEERTZ, B., WEINBERGER, F., KRAMER, E., SCHLOSSAREK, S., MOUROT-FILIATRE, J., STOEHR, A., DUTSCH, A., WIJNKER, P. J., BRAREN, I., KATUS, H. A., MULLER, O. J., VOIT, T., ESCHENHAGEN, T. & CARRIER, L. 2014. Mybpc3 gene therapy for neonatal cardiomyopathy enables long-term disease prevention in mice. *Nat Commun,* 5**,** 5515.
MEARINI, G., STIMPEL, D., KRAMER, E., GEERTZ, B., BRAREN, I., GEDICKE-HORNUNG, C., PRECIGOUT, G., MULLER, O. J., KATUS, H. A., ESCHENHAGEN, T., VOIT, T., GARCIA, L., LORAIN, S. & CARRIER, L. 2013. Repair of Mybpc3 mRNA by 5'-trans-splicing in a Mouse Model of Hypertrophic Cardiomyopathy. *Mol Ther Nucleic Acids,* 2**,** e102.
MERKLE, F. T. & EGGAN, K. 2013. Modeling human disease with pluripotent stem cells: from genome association to function. *Cell Stem Cell,* 12**,** 656-68.
MINAMI, I., YAMADA, K., OTSUJI, T. G., YAMAMOTO, T., SHEN, Y., OTSUKA, S., KADOTA, S., MORONE, N., BARVE, M., ASAI, Y., TENKOVA-HEUSER, T., HEUSER, J. E., UESUGI, M., AIBA, K. & NAKATSUJI, N. 2012. A small molecule that promotes cardiac differentiation of human pluripotent stem cells under defined, cytokine- and xeno-free conditions. *Cell Rep,* 2**,** 1448-60.
MOJICA, F. J., DIEZ-VILLASENOR, C., GARCIA-MARTINEZ, J. & SORIA, E. 2005. Intervening sequences of regularly spaced prokaryotic repeats derive from foreign genetic elements. *J Mol Evol,* 60**,** 174-82.
MOJICA, F. J., FERRER, C., JUEZ, G. & RODRIGUEZ-VALERA, F. 1995. Long stretches of short tandem repeats are present in the largest replicons of the Archaea Haloferax mediterranei and Haloferax volcanii and could be involved in replicon partitioning. *Mol Microbiol,* 17**,** 85-93.
MOSQUEIRA, D., MANNHARDT, I., BHAGWAN, J. R., LIS-SLIMAK, K., KATILI, P., SCOTT, E., HASSAN, M., PRONDZYNSKI, M., HARMER, S. C., TINKER, A., SMITH, J. G. W., CARRIER, L., WILLIAMS, P. M., GAFFNEY, D., ESCHENHAGEN, T., HANSEN, A. & DENNING, C. 2018. CRISPR/Cas9 editing in human pluripotent stem cell-cardiomyocytes highlights arrhythmias, hypocontractility, and energy depletion as potential therapeutic targets for hypertrophic cardiomyopathy. *Eur Heart J,* 39**,** 3879-3892.
MUSUNURU, K., SHEIKH, F., GUPTA, R. M., HOUSER, S. R., MAHER, K. O., MILAN, D. J., TERZIC, A., WU, J. C., AMERICAN HEART ASSOCIATION COUNCIL ON FUNCTIONAL, G., TRANSLATIONAL, B., COUNCIL ON CARDIOVASCULAR DISEASE IN THE, Y., COUNCIL ON, C. & STROKE, N. 2018. Induced Pluripotent Stem Cells for Cardiovascular Disease Modeling and Precision Medicine: A Scientific Statement From the American Heart Association. *Circ Genom Precis Med,* 11**,** e000043.

NIJENKAMP, L., BOLLEN, I. A. E., VAN VELZEN, H. G., REGAN, J. A., VAN SLEGTENHORST, M., NIESSEN, H. W. M., SCHINKEL, A. F. L., KRUGER, M., POGGESI, C., HO, C. Y., KUSTER, D. W. D., MICHELS, M. & VAN DER VELDEN, J. 2018. Sex Differences at the Time of Myectomy in Hypertrophic Cardiomyopathy. *Circ Heart Fail,* 11**,** e004133.

OHIRI, J. C. & MCNALLY, E. M. 2018. Gene Editing and Gene-Based Therapeutics for Cardiomyopathies. *Heart Fail Clin,* 14**,** 179-188.

OJALA, M. & AALTO-SETÄLÄ, K. 2016. Modeling Hypertrophic Cardiomyopathy with Human Induced Pluripotent Stem Cells, Pluripotent Stem Cells - From the Bench to the Clinic, Minoru Tomizawa. *IntechOpen*.

ORTIZ, M. F., RODRIGUEZ-GARCIA, M. I., HERMIDA-PRIETO, M., FERNANDEZ, X., VEIRA, E., BARRIALES-VILLA, R., CASTRO-BEIRAS, A. & MONSERRAT, L. 2009. A homozygous MYBPC3 gene mutation associated with a severe phenotype and a high risk of sudden death in a family with hypertrophic cardiomyopathy. *Rev Esp Cardiol,* 62**,** 572-5.

PAQUET, D., KWART, D., CHEN, A., SPROUL, A., JACOB, S., TEO, S., OLSEN, K. M., GREGG, A., NOGGLE, S. & TESSIER-LAVIGNE, M. 2016. Efficient introduction of specific homozygous and heterozygous mutations using CRISPR/Cas9. *Nature,* 533**,** 125-9.

PARIKH, S. S., BLACKWELL, D. J., GOMEZ-HURTADO, N., FRISK, M., WANG, L., KIM, K., DAHL, C. P., FIANE, A., TONNESSEN, T., KRYSHTAL, D. O., LOUCH, W. E. & KNOLLMANN, B. C. 2017. Thyroid and Glucocorticoid Hormones Promote Functional T-Tubule Development in Human-Induced Pluripotent Stem Cell-Derived Cardiomyocytes. *Circ Res,* 121**,** 1323-1330.

PARK, I. H., LEROU, P. H., ZHAO, R., HUO, H. & DALEY, G. Q. 2008. Generation of human-induced pluripotent stem cells. *Nat Protoc,* 3**,** 1180-6.

PRONDZYNSKI, M., KRAMER, E., LAUFER, S. D., SHIBAMIYA, A., PLESS, O., FLENNER, F., MULLER, O. J., MUNCH, J., REDWOOD, C., HANSEN, A., PATTEN, M., ESCHENHAGEN, T., MEARINI, G. & CARRIER, L. 2017. Evaluation of MYBPC3 trans-Splicing and Gene Replacement as Therapeutic Options in Human iPSC-Derived Cardiomyocytes. *Mol Ther Nucleic Acids,* 7**,** 475-486.

PRONDZYNSKI, M., LEMOINE, M. D., ZECH, A. T., HORVATH, A., DI MAURO, V., KOIVUMAKI, J. T., KRESIN, N., BUSCH, J., KRAUSE, T., KRAMER, E., SCHLOSSAREK, S., SPOHN, M., FRIEDRICH, F. W., MUNCH, J., LAUFER, S. D., REDWOOD, C., VOLK, A. E., HANSEN, A., MEARINI, G., CATALUCCI, D., MEYER, C., CHRIST, T., PATTEN, M., ESCHENHAGEN, T. & CARRIER, L. 2019a. Disease modeling of a mutation in alpha-actinin 2 guides clinical therapy in hypertrophic cardiomyopathy. *EMBO Mol Med***,** e11115.

PRONDZYNSKI, M., MEARINI, G. & CARRIER, L. 2019b. Gene therapy strategies in the treatment of hypertrophic cardiomyopathy. *Pflugers Arch,* 471**,** 807-815.

RAJALA, K., PEKKANEN-MATTILA, M. & AALTO-SETALA, K. 2011. Cardiac differentiation of pluripotent stem cells. *Stem Cells Int,* 2011**,** 383709.

RAN, F. A., HSU, P. D., WRIGHT, J., AGARWALA, V., SCOTT, D. A. & ZHANG, F. 2013. Genome engineering using the CRISPR-Cas9 system. *Nat Protoc,* 8**,** 2281-2308.

RICHARD, P., CHARRON, P., CARRIER, L., LEDEUIL, C., CHEAV, T., PICHEREAU, C., BENAICHE, A., ISNARD, R., DUBOURG, O., BURBAN, M., GUEFFET, J. P., MILLAIRE, A., DESNOS, M., SCHWARTZ, K., HAINQUE, B., KOMAJDA, M. & PROJECT, E. H. F. 2003. Hypertrophic cardiomyopathy: distribution of disease genes, spectrum of mutations, and implications for a molecular diagnosis strategy. *Circulation,* 107**,** 2227-32.

RONALDSON-BOUCHARD, K., MA, S. P., YEAGER, K., CHEN, T., SONG, L., SIRABELLA, D., MORIKAWA, K., TELES, D., YAZAWA, M. & VUNJAK-NOVAKOVIC, G. 2018. Advanced maturation of human cardiac tissue grown from pluripotent stem cells. *Nature,* 556**,** 239-243.

RUAN, J. L., TULLOCH, N. L., RAZUMOVA, M. V., SAIGET, M., MUSKHELI, V., PABON, L., REINECKE, H., REGNIER, M. & MURRY, C. E. 2016. Mechanical Stress Conditioning and Electrical Stimulation Promote Contractility and Force Maturation of Induced Pluripotent Stem Cell-Derived Human Cardiac Tissue. *Circulation,* 134**,** 1557-1567.

SABATER-MOLINA, M., PEREZ-SANCHEZ, I., HERNANDEZ DEL RINCON, J. P. & GIMENO, J. R. 2018. Genetics of hypertrophic cardiomyopathy: A review of current state. *Clin Genet,* 93**,** 3-14.

SALEH-GOHARI, N. & HELLEDAY, T. 2004. Conservative homologous recombination preferentially repairs DNA double-strand breaks in the S phase of the cell cycle in human cells. *Nucleic Acids Res,* 32**,** 3683-8.

SCHAAF, S., SHIBAMIYA, A., MEWE, M., EDER, A., STOHR, A., HIRT, M. N., RAU, T., ZIMMERMANN, W. H., CONRADI, L., ESCHENHAGEN, T. & HANSEN, A. 2011. Human engineered heart tissue as a versatile tool in basic research and preclinical toxicology. *PLoS One,* 6**,** e26397.

SCHLOSSAREK, S., MEARINI, G. & CARRIER, L. 2011. Cardiac myosin-binding protein C in hypertrophic cardiomyopathy: mechanisms and therapeutic opportunities. *J Mol Cell Cardiol,* 50**,** 613-20.

SEEGER, T., SHRESTHA, R., LAM, C. K., CHEN, C., MCKEITHAN, W. L., LAU, E., WNOROWSKI, A., MCMULLEN, G., GREENHAW, M., LEE, J., OIKONOMOPOULOS, A., LEE, S., YANG, H., MERCOLA, M., WHEELER, M., ASHLEY, E. A., YANG, F., KARAKIKES, I. & WU, J. C. 2019. A Premature Termination Codon Mutation in MYBPC3 Causes Hypertrophic Cardiomyopathy via Chronic Activation of Nonsense-Mediated Decay. *Circulation,* 139**,** 799-811.

SEMSARIAN, C., INGLES, J., MARON, M. S. & MARON, B. J. 2015. New perspectives on the prevalence of hypertrophic cardiomyopathy. *J Am Coll Cardiol,* 65**,** 1249-1254.

SPATER, D., HANSSON, E. M., ZANGI, L. & CHIEN, K. R. 2014. How to make a cardiomyocyte. *Development,* 141**,** 4418-31.

SPUDICH, J. A. 2019. Three perspectives on the molecular basis of hypercontractility caused by hypertrophic cardiomyopathy mutations. *Pflugers Arch,* 471**,** 701-717.

STERNBERG, S. H. & DOUDNA, J. A. 2015. Expanding the Biologist's Toolkit with CRISPR-Cas9. *Mol Cell,* 58**,** 568-74.

STOEHR, A., NEUBER, C., BALDAUF, C., VOLLERT, I., FRIEDRICH, F. W., FLENNER, F., CARRIER, L., EDER, A., SCHAAF, S., HIRT, M. N., AKSEHIRLIOGLU, B., TONG, C. W., MORETTI, A., ESCHENHAGEN, T. & HANSEN, A. 2014. Automated analysis of contractile force and Ca2+ transients in engineered heart tissue. *Am J Physiol Heart Circ Physiol,* 306**,** H1353-63.

STOHR, A., FRIEDRICH, F. W., FLENNER, F., GEERTZ, B., EDER, A., SCHAAF, S., HIRT, M. N., UEBELER, J., SCHLOSSAREK, S., CARRIER, L., HANSEN, A. & ESCHENHAGEN, T. 2013. Contractile abnormalities and altered drug response in engineered heart tissue from Mybpc3-targeted knock-in mice. *J Mol Cell Cardiol,* 63**,** 189-98.

TAAPKEN, S. M., NISLER, B. S., NEWTON, M. A., SAMPSELL-BARRON, T. L., LEONHARD, K. A., MCINTIRE, E. M. & MONTGOMERY, K. D. 2011. Karotypic abnormalities in human induced pluripotent stem cells and embryonic stem cells. *Nat Biotechnol,* 29**,** 313-4.

TAKAHASHI, K., TANABE, K., OHNUKI, M., NARITA, M., ICHISAKA, T., TOMODA, K. & YAMANAKA, S. 2007. Induction of pluripotent stem cells from adult human fibroblasts by defined factors. *Cell,* 131**,** 861-72.

TAKAHASHI, K. & YAMANAKA, S. 2006. Induction of pluripotent stem cells from mouse embryonic and adult fibroblast cultures by defined factors. *Cell,* 126**,** 663-76.

TARDIFF, J. C., CARRIER, L., BERS, D. M., POGGESI, C., FERRANTINI, C., COPPINI, R., MAIER, L. S., ASHRAFIAN, H., HUKE, S. & VAN DER VELDEN, J. 2015. Targets for therapy in sarcomeric cardiomyopathies. *Cardiovasc Res,* 105**,** 457-70.

ULMER, B. M., STOEHR, A., SCHULZE, M. L., PATEL, S., GUCEK, M., MANNHARDT, I., FUNCKE, S., MURPHY, E., ESCHENHAGEN, T. & HANSEN, A. 2018. Contractile Work Contributes to Maturation of Energy Metabolism in hiPSC-Derived Cardiomyocytes. *Stem Cell Reports,* 10**,** 834-847.

UZUN, A. U., MANNHARDT, I., BRECKWOLDT, K., HORVATH, A., JOHANNSEN, S. S., HANSEN, A., ESCHENHAGEN, T. & CHRIST, T. 2016. Ca(2+)-Currents in Human Induced Pluripotent Stem Cell-Derived Cardiomyocytes Effects of Two Different Culture Conditions. *Front Pharmacol,* 7**,** 300.

VIGNIER, N., SCHLOSSAREK, S., FRAYSSE, B., MEARINI, G., KRAMER, E., POINTU, H., MOUGENOT, N., GUIARD, J., REIMER, R., HOHENBERG, H., SCHWARTZ, K., VERNET, M., ESCHENHAGEN, T. & CARRIER, L. 2009. Nonsense-mediated mRNA decay and ubiquitin-proteasome system regulate cardiac myosin-binding protein C mutant levels in cardiomyopathic mice. *Circ Res,* 105**,** 239-48.

WANG, C., ZHAI, X., ZHANG, X., LI, L., WANG, J., LIU, D. P. & CHINESE ACADEMY OF MEDICAL, S. 2019. Gene-edited babies: Chinese Academy of Medical Sciences' response and action. *Lancet,* 393**,** 25-26.

WEINBERGER, F., BRECKWOLDT, K., PECHA, S., KELLY, A., GEERTZ, B., STARBATTY, J., YORGAN, T., CHENG, K. H., LESSMANN, K., STOLEN, T., SCHERRER-CROSBIE, M., SMITH, G., REICHENSPURNER, H., HANSEN, A. & ESCHENHAGEN, T. 2016. Cardiac repair in guinea pigs with human engineered heart tissue from induced pluripotent stem cells. *Sci Transl Med,* 8**,** 363ra148.

WESSELS, M. W., HERKERT, J. C., FROHN-MULDER, I. M., DALINGHAUS, M., VAN DEN WIJNGAARD, A., DE KRIJGER, R. R., MICHELS, M., DE COO, I. F., HOEDEMAEKERS, Y. M. & DOOIJES, D. 2015. Compound heterozygous or homozygous truncating MYBPC3 mutations cause lethal cardiomyopathy with features of noncompaction and septal defects. *Eur J Hum Genet,* 23**,** 922-8.

WIJNKER, P. J., FRIEDRICH, F. W., DUTSCH, A., REISCHMANN, S., EDER, A., MANNHARDT, I., MEARINI, G., ESCHENHAGEN, T., VAN DER VELDEN, J. & CARRIER, L. 2016. Comparison of the effects of a truncating and a missense MYBPC3 mutation on contractile parameters of engineered heart tissue. *J Mol Cell Cardiol,* 97**,** 82-92.

WINBO, A., RAMANAN, S., EUGSTER, E., JOVINGE, S., SKINNER, J. R. & MONTGOMERY, J. M. 2020. Functional coculture of sympathetic neurons and cardiomyocytes derived from human-induced pluripotent stem cells. *Am J Physiol Heart Circ Physiol,* 319**,** H927-H937.

WRIGHT, A. V., NUNEZ, J. K. & DOUDNA, J. A. 2016. Biology and Applications of CRISPR Systems: Harnessing Nature's Toolbox for Genome Engineering. *Cell,* 164**,** 29-44.

YU, J., HU, K., SMUGA-OTTO, K., TIAN, S., STEWART, R., SLUKVIN, II & THOMSON, J. A. 2009. Human induced pluripotent stem cells free of vector and transgene sequences. *Science,* 324**,** 797-801.

ZECH, A. T. L., SINGH, S. R., SCHLOSSAREK, S. & CARRIER, L. 2019. Autophagy in cardiomyopathies. *Biochim Biophys Acta Mol Cell Res*.

ZHANG, J., KLOS, M., WILSON, G. F., HERMAN, A. M., LIAN, X., RAVAL, K. K., BARRON, M. R., HOU, L., SOERENS, A. G., YU, J., PALECEK, S. P., LYONS, G. E., THOMSON, J. A., HERRON, T. J., JALIFE, J. & KAMP, T. J. 2012. Extracellular matrix promotes highly efficient cardiac differentiation of human pluripotent stem cells: the matrix sandwich method. *Circ Res,* 111**,** 1125-36.

ZHANG, L., ZHONG, P., ZHAI, X., SHAO, Y., LU, S. & SIGNATORIES 2019. Open letter from Chinese HIV professionals on human genome editing. *Lancet,* 393**,** 26-27.

ZHANG, X. H., TEE, L. Y., WANG, X. G., HUANG, Q. S. & YANG, S. H. 2015. Off-target Effects in CRISPR/Cas9-mediated Genome Engineering. *Mol Ther Nucleic Acids,* 4**,** e264.

ZHANG, Y., LONG, C., BASSEL-DUBY, R. & OLSON, E. N. 2018. Myoediting: Toward Prevention of Muscular Dystrophy by Therapeutic Genome Editing. *Physiol Rev,* 98**,** 1205-1240.

ZHOU, P. & PU, W. T. 2016. Recounting Cardiac Cellular Composition. *Circ Res,* 118**,** 368-70.

ZIMMERMANN, W. H., DIDIE, M., WASMEIER, G. H., NIXDORFF, U., HESS, A., MELNYCHENKO, I., BOY, O., NEUHUBER, W. L., WEYAND, M. & ESCHENHAGEN, T. 2002. Cardiac grafting of engineered heart tissue in syngenic rats. *Circulation,* 106**,** I151-7.

8 List of figures

9 List of tables

10 Supplement

10.1 Additional figures

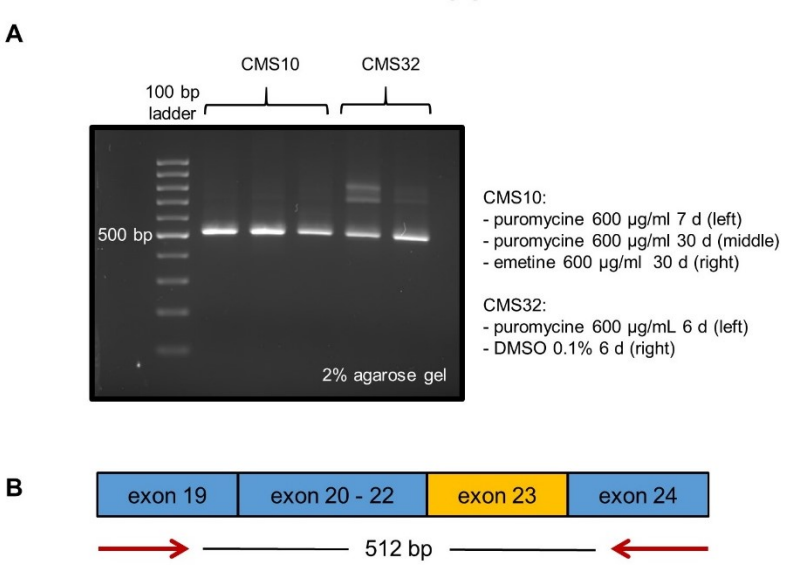

Figure 50: Inhibition of the nonsense-mediated mRNA decay (PCR#3)
Comparison between treated CMS32-CMs and CMs derived from another hiPSC-line (CMS10) with different MYBPC3 mutation to exclude drug treatment artefacts. ***A*** *mRNA analysis of hiPSC-CMs from CMS32 and CMS10 treated with puromycine (8 h) or emetine (4 h) in different concentrations after 6/7/30 days of culture (2D).* ***B*** *Short amplification strategy to detect the mutant transcript(s). Wild-type fragment size is 512 bp. d = days in vitro.*

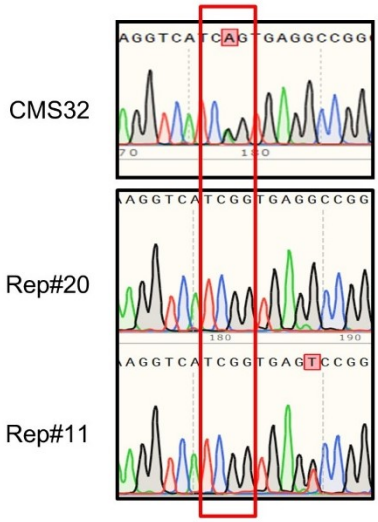

Figure 51: CRISPR Repair sequencing results
Sequences of HDR repaired hiPSC clones Rep#20 and Rep#11 in comparison to CMS32. Mark as well the presence of the silent mutation in Rep#11. HDR: homology-directed repair.

Figure 52: Off-target analysis CRISPR Repair (top 10)
A *Off-target sequences of Rep#11 aligned to wild-type.* ***B*** *Off-target sequences of Rep#12 aligned to wild-type.* ***C*** *Off-target sequences of Rep#28 aligned to wild-type.* ***A – C*** *showed no off-target effects.*

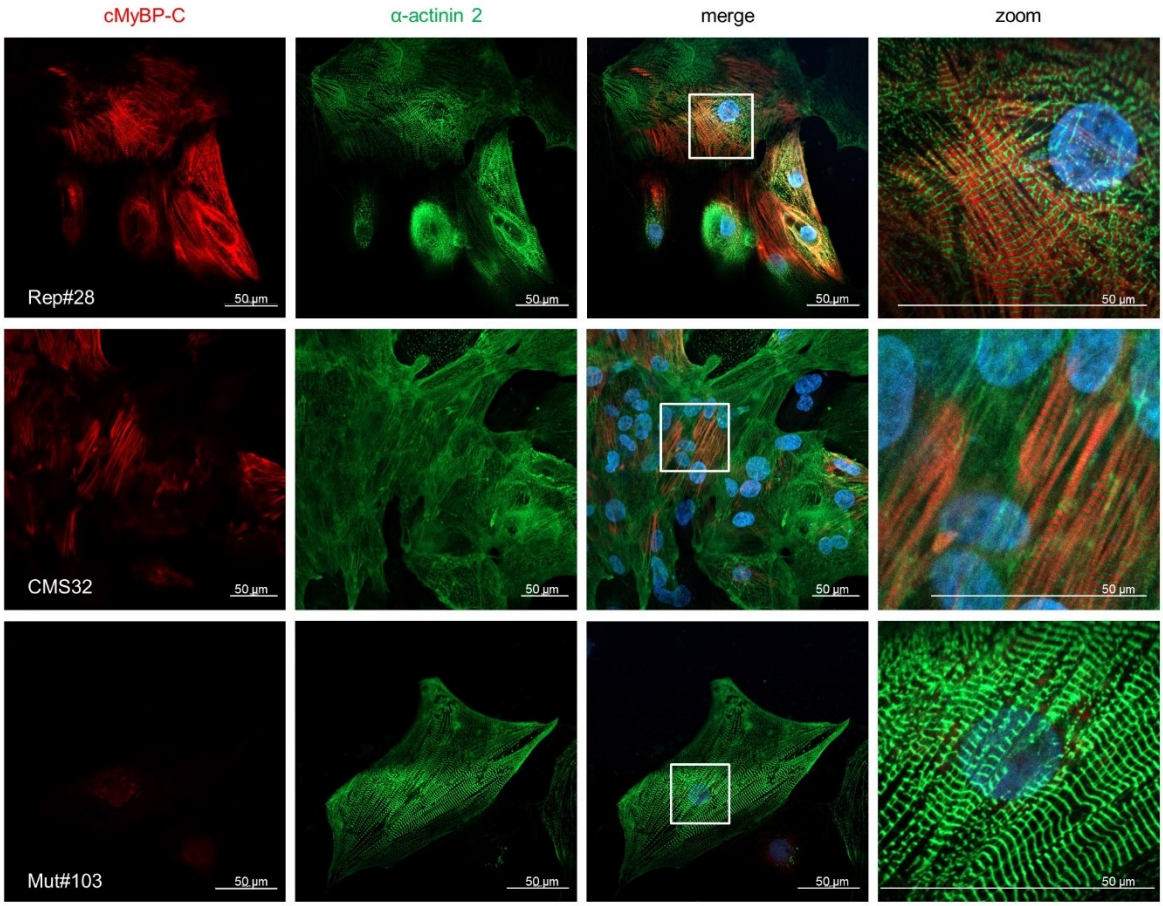

Figure 53: Representative immunofluorescence images of the three hiPSC-CM lines without gene therapy
Location of the zoom is reflected by the white rectangles.

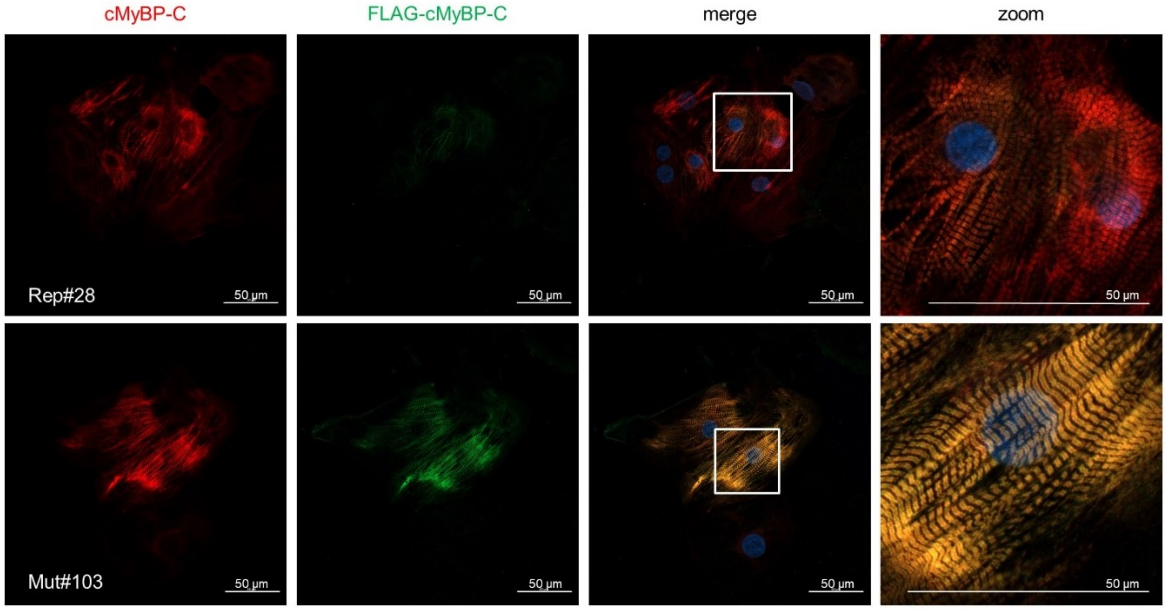

Figure 54: Representative immunofluorescence images of Rep#28 and Mut#103 hiPSC-CMs after MYBPC3 gene therapy
Location of the zoom is reflected by the white rectangles.

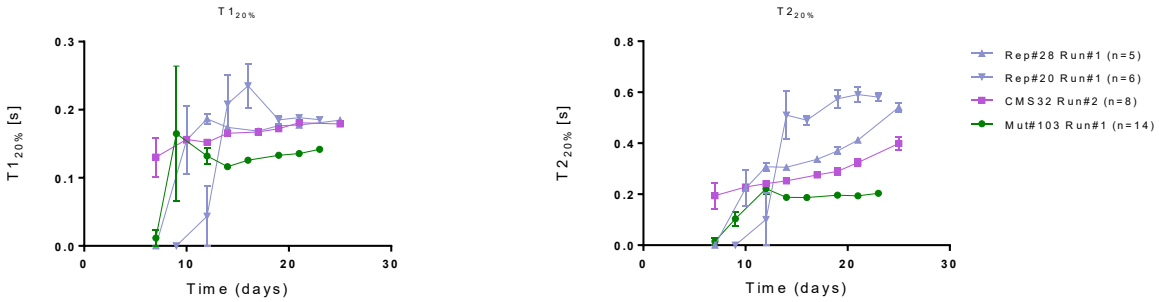

Figure 55: Development of contraction kinetics in EHTs
$T1_{20\%}$ and $T2_{20\%}$ are shown over time for the three genotypes. n indicates the number of biological replicates from one differentiation batch. Data are expressed as mean ± SEM.

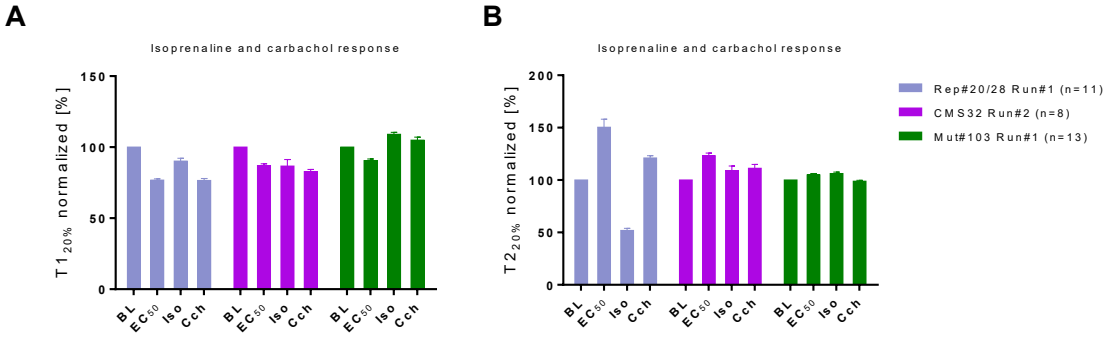

Figure 56: Isoprenaline and carbachol response of EHTs – $T1_{20\%}$ and $T2_{20\%}$
***A** Effect on $T1_{20\%}$. **B** Effect on $T2_{20\%}$. n indicates the number of biological replicates from one differentiation batch. Data are expressed as mean ± SEM. BL = baseline in 1.8 mM [Ca^{2+}]; Cch = carbachol (10 µM); EC_{50} = measurements at calculated EC_{50} calcium levels; Iso = isoprenaline (100 nM). Pacing frequencies: Rep#20/28 (1.0 Hz), CMS32 (1.0 Hz), Mut#103 (2.0 Hz).*

10.2 Abbreviations

°C	Degree celsius
β-MHC	β-myosin heavy chain
µg	Micrograms
µL	Microliter
µm	Micrometre
µM	Micromolar
2D	Two-dimensional
3D	Three-dimensional
A	Adenine
AAV	Adeno-associated virus
ACTC1	Cardiac muscle alpha actin (Gene)
ALP	Autophagy-lysosomal pathway
ANOVA	Analysis of variance
AO	Aorta

APD	Action potential duration
APS	Ammonium persulphate
ARVC	Arrhythmogenic right ventricular cardiomyopathy
bFGF	Basic fibroblast growth factor
BL	Baseline
BMP4	Bone morphogenetic protein 4
bp	Base pair(s)
bpm	Beats per minute
C	Cytosine
Ca^{2+}	Calcium
Cas	CRISPR-associated protein
Cch	Carbachol
CCR5	C-C chemokine receptor type 5 (Gene)
cDNA	Complementary deoxyribonucleic acid
CHX	Cycloheximide
CM/CMs	Cardiomyocyte/cardiomoycytes
cm	Centimetre
cMyBP-C	Cardiac myosin-binding protein C
c-Myc	Cellular myelocytomatosis
CRISPR	Clustered Regularly Interspaced Short Palindromic Repeats
crRNA	CRISPR RNA
cTNT	Cardiac troponin T
CV	Contraction velocity
d	Days *in vitro*
DCM	Dilated cardiomyopathy
DMD	Duchenne muscular dystrophy
DMEM	Dulbecco's Modified Eagle Medium
DMSO	Dimethyl sulfoxide
DNA	Deoxyribonucleic acid
dNTP	Deoxynucleoside triphosphate
DSB	Double-strand break
DTT	Dithiothreitol
e.g.	Exempli gratia (for example)
EB	Embryoid body
EC_{50}	Half maximal effective concentration
ECL	Enhanced chemiluminescence
EDTA	Ethylendiamintetraacetic acid
EHT	Engineered heart tissue
et al.	Et alii (and others)
F	Forward
FACS	Fluorescence-activated cell sorting
FCS	Fetal calf serum
FGF	Fibroblast growth factor
fs	Frameshift
FTDA	bFGF, TGFβ1, dorsomorphin and activin A based hiPSC culture medium
g	Gram
g	Gravitational constant
G	Guanine

G2 phase	Gap 2 phase
GAPDH	Glyceraldehyde-3-phosphate dehydrogenase
gDNA	Genomic DNA
gRNA	Guide RNA
GT	Gene therapy
h	Hour
HBSS	Hank's Balanced Salt Solution
HCM	Hypertrophic cardiomyopathy
HDR	Homology-directed repair
HEPES	4-(2-hydroxyethyl)-1piperazineethanesulfonic acid
hESCs	Human embryonic stem cells
hiPSCs	Human-induced pluripotent stem cells
hiPSC-CMs	Human iPSC-derived cardiomyocytes
HIV	Human immunodeficiency virus
Hz	Hertz
i.e.	Id est (that is)
IEPT	Institute of Experimental Pharmacology
IgG	Immunoglobulin G
iPSCs	Induced pluripotent stem cells
Iso	Isoprenaline
IVF	*in vitro* fertilisation
kb	Kilobase
kbp	Kilobase pair(s)
kDa	Kilodalton
KI	Knock-in
KLF4	Kruppel-like factor 4
l	litre
L	Litre
LA	Left atrium
LB	Lysogeny broth
LV	Left ventricle
LVNC	Left ventricular non-compaction
m	metre
M	Molar
mA	Milliampere
MCB	Master cell bank
MEF	Mouse embryonic fibroblasts
mg	Milligrams
Mg^{2+}	Magnesium
min	Minutes
mL	Millilitre
mm	Millimetre
mM	Millimolar
MOI	Multiplicity of infection
mRNA	Messenger ribonucleic acid
Mut	Mutant
MW	Molecular weight
MYBPC3	Cardiac myosin-binding protein C (Gene)

MYH7	β-myosin heavy chain (Gene)
MYL2	Cardiac myosin regulatory light chain 2 (Gene)
MYL3	Cardiac myosin essential light chain 3 (Gene)
N	Newton
NC	Nitrocellulose
NCBI	National Centre for Biotechnology Information
NF	Non-failing
NGG	N: any nucleotide base, G: Guanine
NHEJ	Nonhomologous end joining
NKM	Non cardiac myocyte medium
nm	Nanometre
NMD	Nonsense-mediated mRNA decay
ns	not significant
NT	Non-transduced
nt	Nucleotide(s)
Oct-4	Octamer-binding transcription factor 4
oligo(dT)	Oligodeoxythymidylic acid
OT	Off-target
PAGE	Polyacrylamide gel electrophoresis
PAM	Protospacer adjacent motif
PBS	Phosphate-buffered saline
PCR	Polymerase chain reaction
PDMS	Polydimethylsiloxane
PGD	Preimplantation genetic diagnosis
pH	-Log10 hydrogen ion activity
PTC	Premature termination codon
R	Reverse
RCM	Restrictive cardiomyopathy
RFP	Red fluorescent protein
RNA	Ribonucleic acid
RNP	Ribonucleoprotein
rpm	Revolutions per minute
RPMI	Roswell Park Memorial Institute
RT	Reverse transcriptase
RT	Room temperature
RT	Reverse transcription
RT-PCR	Reverse transcriptase PCR
RV	Relaxation velocity
RV	Right ventricle
s	Seconds
S phase	Synthesis Phase
S. pyogenes	Streptococcus pyogens
SDS	Sodium dodecyl sulfate
SDS-PAGE	Sodium dodecyl sulfate polyacrylamide gel electrophoresis
SEM	Standard error of the mean
Ser	Serine
sgRNA	Single guide RNA
SOC medium	Super Optimal Broth medium

SOP	Standard Operating Procedure
Sox2	Sex determining region Y-box 2
SSEA3	Stage-specific embryonic antigen 3
ssODN	Single-stranded DNA oligonucleotides
T	Thymine
$T1_{20\%}$	Contraction time
$T2_{20\%}$	Relaxation time
TAE	Tris acetate EDTA
TALEN	Transcription activator-like effector nucleases
TBS	Tris buffered saline
TBS-T	Tris buffered saline with Tween 20
TEMED	N, N, N´, N´-tetramethylethylenediamine
TGF-β	Transforming growth factor-β
TNNI3	Cardiac troponin I (Gene)
TNNT2	Cardiac troponin T (Gene)
TPM1	Tropomyosin alpha-1 chain (Gene)
tracrRNA	Trans-activating crRNA
TRIS	tris-(hydroxymethyl)-aminoethane
U	Unit
UKE	University Medical Centre Hamburg-Eppendorf
UPS	Ubiquitin-proteasome system
V	Volt
VUS	Variant of uncertain significance
WNT	Wingless/INT
WT	Wild-type
x	Times
ZFN	Zinc-finger nuclease

10.3 Materials

10.3.1 Cell Culture Media

Stem cell media

FTDA	Final concentration
DMEM/F-12 without Glutamine	Basis medium
L-Glutamine	2 mM
Transferrin	5 mg/L
Sodium selenite	5 µg/L
Human serum albumin	0.1%
Lipid mix	1:1000
Human recombinant insulin	5 mg/L
Dorsomorphin	50 nM
Activin A	2.5 ng/mL
Transforming growth factor-β 1 (TGFβ1)	0.5 ng/mL
bFGF (freshly added)	30 ng/mL

➔ sterile filtered, stored at 4°C

Conditioned medium	Final concentration
DMEM/F-12 without Glutamine	Basis medium
Non-essential amino acids (NEAA)	1%
L-Glutamine	1%
Penicillin/streptomycin	0.5%
2-Mercaptoethanol	3.5 µL/500 mL
Knockout serum replacement	20%

➔ For production of this medium, 10 ng/mL bFGF was added before use on mouse embryonic fibroblasts (MEFs, strain CF-1). These fibroblasts were inactivated while mitosis using 10 µg/mL mitomycin C for 2.5 hours. After dissociation with trypsin, the MEFs were seeded into a culture flask coated with 0.1% gelatine (seeding density of 60,000/cm^2). After 24 hours incubation time, the medium production was finished and medium was sterile filtered for usage. As for FTDA medium, bFGF was added freshly (30 ng/mL).

Cardiac differentiation

Cheese stage 0 / day 0	Final concentration
StemPro®-34 SFM Complete Medium	Basis medium
StemPro®-34 SFM-34 Nutrient Supplement	26 µL/mL
Matrigel® (for EHT generation)	1:100
BMP4	1 ng/mL
L-Glutamine	1:100

Cheese stage 1 / day 1	Final concentration
StemPro®-34 SFM Complete Medium	Basis medium
StemPro®-34 SFM-34 Nutrient Supplement	26 µL/mL
Activin A	8 ng/mL
BMP4	10 ng/mL
L-Glutamine	1:100

Cheese stage 2.1 / day 3	Final concentration
RPMI 1640	Basis medium
B27 minus insulin	1:50
KY 02111	10 µM
XAV 939	10 µM

Cheese stage 2.2 / day 5	Final concentration
RPMI 1640	Basis medium
B27 with insulin (0.156 mg/mL B27)	1:50
KY 02111	10 µM
XAV 939	10 µM

Cheese feeding medium / day 7 - dissociation	Final concentration
RPMI 1640	Basis medium
B27 with insulin (0.156 mg/mL B27)	1:50

➔ prepared fresh, used within a few days, stored at 4 °C

Engineered heart tissues

EHT medium	Final concentration
DMEM	Basis medium

Horse serum	10%
Insulin	10 µg/mL
Aprotinin	33 µg/mL
Penicillin/streptomycin	1%

➔ sterile filtered, prepared fresh

NKM	**Final concentration**
DMEM	Basis medium
Fetal Calf Serum superior	10%
L-Glutamine	2 mM
Penicillin/streptomycin	1%

➔ sterile filtered, prepared fresh

10.3.2 Antibodies for FACS

Antibodies for FACS	**Dilution**	**Manufacturer**
PE Rat anti-SSEA3 (Rat IgM clone MC-631)	1:5	BD Biosciences
PE Rat IgM, κ Isotype Control (Rat IgM clone R4-22)	1:80	BD Biosciences
Anti-cardiac troponin T-FITC (Recombinant human IgG1, clone REA400)	1:10	Miltenyi Biotec
REA Control (I)-FITC human (Isotype control IgG1, clone REA400)	1:10	Miltenyi Biotec

All other used antibodies for Western blots and immunofluorescence are listed in the respective chapters in the Material and methods (cf. 2).

10.3.3 Bacterial strains

Bacterial strain	**Manufacturer**
One Shot® TOP10 Chemically Competent *E.coli*	Invitrogen

10.3.4 Chemicals, reagents, drugs etc.

Chemicals, reagents, drugs etc.	**Manufacturer**
1,4-Dithiothreitol (DTT)	Roth
10x DMEM	Gibco
2-Mercaptoethanol	Sigma-Aldrich
2-Propanol	Merck Millipore
Accutase™ Cell Dissociation Reagent	Gibco
Acetic acid (concentrated; glacial, 100%)	Merck
Acrylamide/Bis 40%	Bio-Rad
Activin A	R&D Systems
Acyrlamide/bis solution (29:1)	Bio-Rad
Agarose	Invitrogen
Alt-R® Cas9 Electroporation Enhancer, 10nmol	IDT®
Alt-R® CRISPR-Cas9 crRNA, 2nmol: gRNA Repair and gRNA Mutation (Purification: Standard Desalting)	IDT®

Alt-R® CRISPR-Cas9 tracrRNA, ATTO™ 550, 5nmol	IDT®
Alt-R® S.p. Cas9 Nuclease 3NLS, 2nmol	IDT®
Ammoniumpersulfate (APS)	Bio-Rad
Ampicillin trihydrate	Serva
Aprotinin	Sigma-Aldrich
Aqua ad iniectabilia	Baxter S.A.
B27 minus insulin	home made
Bacto™ Agar	BD
Bacto™ Tryptone	BD
Bacto™ Yeast Extract	BD
BMP4	R&D Systems
BTS (N-Benzyl-p-Toluenesulfonamide)	TCI
$CaCl_2$ x $2H_2O$	Merck
Carbachol	Merck
Clarity™ and Clarity Max™ Western ECL Blotting Substrates	Bio-Rad
Collagenase II	Worthington
Cycloheximide (CHX)	Sigma-Aldrich
D(+)-Glucose anhydrous	Roth
DMEM	Biochrom
DMEM/F-12 without Glutamine	Gibco
DMSO for cell culture	Sigma-Aldrich
DMSO for molecular experiments (PCR)	Thermo Fisher Scientific
DNA loading dye, 6x	Thermo Fisher Scientific
DNase II, type V (from bovine spleen)	Sigma-Aldrich
dNTP mix (2 mM each)	Thermo Fisher Scientific
Dorsomorphin	Abcam or Tocris
DreamTaq DNA Polymerase (5 U/µL) with 10X DreamTaq Green Buffer	Thermo Fisher Scientific
Dulbecco´s modified Eagle medium (DMEM)	Biochrom
EDTA	Roth
Emetine	Sigma-Aldrich
Ethanol, absolute	Chemsolute
Ethylenediamine-tetraacetic acid disodium salt dihydrate (Na_2EDTA x $2H_2O$)	Roth
Fetal Calf Serum superior (FCS)	Biochrom
FGF2 (human recombinant basic FGF)	Peprotech
Fibrinogen	Sigma-Aldrich
Formaldehyd	Merck Millipore
Geltrex™ LDEV-Free	Gibco
Gene Ruler™ 1 kb DNA Ladder	Thermo Fisher Scientific
Gene Ruler™ 100 bp DNA Ladder	Thermo Fisher Scientific
Glycerol	Merck
Glycine	Roth
HBSS minus Ca^{2+}/Mg^{2+}	Gibco
HEPES	Roth
Histofix®	Roth
Hoechst 33342, trihydrochloride trihydrate	Thermo Fisher Scientific
Horse serum	Life Technologies
Human serum albumin	Biological Industries
Hydrochloric acid 1 N	Roth
Hydrochloric acid, 37% fuming	Merck
IDTE (1x TE Solution)	IDT®

Insulin, human	Sigma-Aldrich
Isoprenaline	Sigma-Aldrich
Knockout serum replacement	Gibco
KY 02111	Tocris
L-Glutamine	Gibco
Lipid mix	Sigma-Aldrich
Magnesium chloride hexahydrate ($MgCl_2 \times 6H_2O$)	Sigma-Aldrich
Matrigel® Basement Membrane Matrix (for EHT generation)	Corning
Matrigel® Growth Factor Reduced (GFR) Basement Membrane Matrix (for hiPSC culture)	Corning
Methanol	J. Baker
$MgCl_2$	Fuka
Midori Green Advance DNA Stain	Nippon Genetics Europe GmbH
Milk powder	Roth
N,N,N',N'-Tetramethyl ethylenediamine (TEMED)	Bio-Rad
Nitrogen, liquid (N2)	TMG
Non essential amino acids (NEAA)	Gibco
Nuclease Free Duplex Buffer	IDT®
Nuclease-free water	Thermo Fisher Scientific
P3 solution	IDT®
P3 supplement	IDT®
PAGE Ultramer DNA Oligo: Repair Template and Mutation Template (PAGE Purification)	IDT®
Paraformaldehyde	Merck
PBS	Gibco
Penicillin/streptomycin	Gibco
Ponceau S	Merck
Potassium chloride (KCl)	Merck
Precision Plus Protein™ Dual Color Standard	Bio-Rad
PrimeSTAR® HS DNA Polymerase with 5x PrimeSTAR® buffer and dNTPs	Takara
Puromycine	Invitrogen
RPMI 1640	Gibco
Saponin	Sigma-Aldrich or Merck
SDS Pellets	Roth
Sodium azide	Sigma-Aldrich
Sodium chloride (NaCl)	JT Baker
Sodium chloride (NaCl) solution (0.9%)	B. Braun
Sodium di-hydrogen phosphate monohydrate ($NaH_2PO_4 \times H_2O$)	Merck
Sodium hydrogen carbonate ($NaHCO_3$)	Merck
Sodium hydroxide solution 0.1 N/1 N	Roth
Sodium selenite	Sigma-Aldrich
StemPro®-34 SFM Complete Medium with Nutrient Supplement	Life Technologies
SuperScript™ III First-Strand Synthesis System for RT-PCR	Invitrogen
T4 DNA Ligase (5 U/µL)	Thermo Fisher Scientific
TBS	Sigma-Aldrich
TGFβ1	Peprotech
Thrombin	Sigma-Aldrich or Biopur
Titriplex® III for analysis (ethylenedinitrilote-traacetic acid, disodium salt dihydrate)	Merck

Transferrin	Sigma-Aldrich
TRIS-hydrochloride	Roth
Trishydroxymethylaminomethane (Tris) base	Sigma
Triton™ X-100	Sigma-Aldrich
Trizma® base	Sigma-Aldrich
TRIzol™ Reagent	Life Technologies
Trypan blue	Biochrom
Tween 20	Sigma-Aldrich
XAV 939	Tocris
Y-27632	Biaffin
Y-27632 * 2 HCl	Biorbyt

10.3.5 Consumable materials

Consumable materials	**Manufacturer**
250 ml Vacuum Filtration "rapid"-Filtermax	TPP
500 ml Vacuum Filtration "rapid"-Filtermax	TPP
96-well micro-clear bottom	Greiner
Amersham™ Protan™ 0.45-µm Nitrocellulose transfer membrane	Whatman™ GE Healthcare
Aspiration pipette, 2 mL	Sarstedt
Cell culture plates (6-well, 12-well, 24-well, 48-well)	Nunc
Cell culture tube, round bottom (for EHT generation)	Greiner Bio-One
Cell scraper	Sarstedt
Cell strainer, 100 µm	Falcon
Cellstar® tubes (15 and 50 mL)	Greiner Bio-One
Comb 10 well 1.0 mm	Bio-Rad
Cryovial CryoPure tube 1.6 mL	Sarstedt
EHT electrode	EHT technologies GmbH
EHT pacing adapter/cable	EHT technologies GmbH
EHT PDMS rack (24-well format)	EHT technologies GmbH
EHT PTFE spacer	EHT technologies GmbH
Falcon tube, graduated, 15 mL	Sarstedt
Falcon tube, graduated, 50 mL	Sarstedt
Flow Cytometry tubes	Sarstedt
Glassware	Schott Duran
Isopropanol container (Mr. Frosty)	Thermo Fisher Scientific
Neubauer chamber	Karl-Hecht KG
Nitrile gloves	Ansell
Nitrocellulose Blotting Membrane	GE Healthcare
Parafilm	Bmis
PCR tubes	Sarstedt
Pipette tips with filter Biosphere® (0.5-1000 µL)	Sarstedt
Pipette tips without filter (0.5-1000 µL)	Biosphere®
QIAcube® HT Plasticware	Qiagen
Reaction tubes Safe Lock 0.2 – 2 mL	Eppendorf
Reagent Trough (with Lid) 170 ml	Qiagen
Serological pipettes 1 mL, 2 mL, 5 mL, 10 mL, 25 mL, 50 mL; wide tip pipette 10 mL	Sarstedt
Short Plates	Bio-Rad
Spacer Plates 0.75 mm	Bio-Rad
Spacer Plates 1.0 mm	Bio-Rad

Sterile filter Filtropur S 0.2 µm	Sarstedt
T75 cell culture flask	Sarstedt
TC dish 100, cell+	Sarstedt
Western blot paper	Whatman™

10.3.6 Kits

Kit	**Manufacturer**
Amaxa™ P3 Primary Cell 4D-Nucleofector X Kit L	Lonza
CloneJET PCR Cloning Kit	Thermo Fisher Scientific
DNeasy® Blood & Tissue Kit	Qiagen
nCounter® Human Karyotype Panel Assay	Nanostring
NucleoSpin® Plasmid Kit	Macherey-Nagel
QIAamp® 96 DNA QIAcube® HT Kit	Qiagen
QIAquick® Gel Extraction Kit	Qiagen
QIAquick® PCR Purification Kit	Qiagen
Qubit™ RNA BR Assay Kit	Invitrogen
Qubit™ RNA HS Assay Kit	Invitrogen
Qubit™ Protein Assay Kit	Invitrogen

10.3.7 Laboratory equipment

Laboratory equipment	**Manufacturer**
4D-Nucleofector™ Core Unit Lonza	Lonza
4D-Nucleofector™ X Unit Lonza	Lonza
Accu-jet pipetting aid	Brand
Agarose GEL Electrophoresis System GT	Bio-Rad
Analytical balance (Genius)	Sartorius
Axioskop 2 with AxioCam color camera	Zeiss
Axiovert 25 with Jenoptik ProgRes Speed XT core 5 camera	Zeiss, Jenoptik (camera)
Blotting-System (Mini Trans-Blot® cell)	Bio-Rad
CASY Cell Counter & Analyzer	OLS®
CB 220	Binder
Centrifuge 5415R	Eppendorf
Centrifuge 5810 R	Eppendorf
Centrifuge J-6B	Beckmann
Centrifuge Rotanta/RP	Hettich
Centrifuge Universal 30 RF	Hettich
Centrifuge, MC6	Sarstedt
ChemiDoc™Touch Imaging System	Bio-Rad
Combispin FVL-2400N with vortex function	PeqLab
Electrophoresis system (Mini PROTEAN® 3 electrophoresis cell	Bio-Rad
EVOS FL Cell Imaging System	Advanced Microscopy Group
FACSCanto II Flow Cytometer	BD Biosciences
Glass equipment	W. Hassa Laborbedarf
HERAcell 150i	Thermo Fisher Scientific

HERAcell 240	Thermo Fisher Scientific
HeraSafe	Heraeus
Ice machine	Scotsman
Incubator shaker C25	New Brunswick Scientific
Kelvitron® t warming cabinett	Heraeus
LSM 800 Airyscan	Zeiss
Magnet plate Variomag/ Cimarec Biosystem	Thermo Scientific
Magnet/heating plate IKA Combimag RET	Janke & Kunkel GmbH& Co KG
Magnetic stirrer (IKAMAG® RET)	IKA® Labortechnik
Mars 1200 GS	Scanlaf
MCO-19M	Sanyo
MCO-20AIC	Sanyo
Microscope	AMG
Microwave	Sharp
Mini Trans-Blot Electrophoretic Transfer Cell	Bio-Rad Laboratories
Mini Trans-Blot® Cell	Bio-Rad
Mini-Protean Tetra Cell	Bio-Rad Laboratories
nCounter SPRINT™ Profiler	NanoString
Neubauer chamber	Karl-Hecht KG
PCR cycler vapo.protect	Eppendorf
PCR cylcer (GeneAmp® PCR system 9700)	Applied Biosystems
pH meter, digital	Mettler Toledo
Pipettes (10, 100, 200 and 1000 mL)	Eppendorf
Pipetus	Hirschmann
PowerPac Bacic Power Supply	Bio-Rad Laboratories
QIAcube® HT	Qiagen
Qubit® 3.0 Fluorometer	Life technologies
S2020 1.8	Thermo Fisher Scientific
S88x Dual Output Square Pulse Stimulator	Grass
Safe2020	Thermo Fisher Scientific
Scale Ohaus Precision Advanced	Ohaus
Security working hood HERAsafeR	Thermo Fisher Scientific
Spectrophotometer (NanoDrop™ ND-1000)	Thermo Fisher Scientific
Sub-cell® GT gel electrophorese tank	Bio-Rad Laboratories
T1-SM Nikon Eclipse TS100	Nikon
Thermomixer 5436	Eppendorf
Thermomixer comfort	Eppendorf
TubeRoller	Benchmark Scientific
Ultra-pure water system Milli-Q	Merck Millipore
Video-optical force analysis system	EHT technologies GmbH
Vortex-genie® 2	Scientific Industries
Water bath	GFL
Water bath 2590	Medax

10.3.8 Primers

All primers were designed using the Primer-BLAST designing tool provided by the National Center for Biotechnology Information (NCBI). The respective sequences are listed in each chapter of the Material and methods (cf. 2.2.3, 2.2.4 and 2.4.4). Primers were ordered from Eurofins genomics.

10.3.9 Buffers, solutions etc.

Buffers, solutions etc.	**Mixture**
10x DMEM	134 mg/mL DMEM powder (stored at 4 °C) dissolved in 5 mL of sterile water, sterile filtered (0.2 µm) and stored at 4 °C for up to 2 months
Agar plates	LB medium with 15 g/L Bacto™ Agar, autoclaved and filled into TC dish 100
Agarose for EHT generation	2% agarose dissolved in 300 mL 1 x PBS, autoclaved and stored at 60 °C
Aprotinin	33 mg/mL Aprotinin dissolved in sterile water, stored at -20 °C for 1 year
Blotting buffer (1x)	20% 5x Blotting buffer, 20% Methanol, 60% Aqua dest.
Blotting buffer (5x)	125 mM Trizma® base and 950 mM Glycine in Aqua dest.
BTS solution	BTS dissolved in DMSO, stored at -20 °C for max. 1 year
Collagenase II solution	HBSS minus calcium/magnesium, collagenase II, 200 units/mL, 1 mM HEPES, 10 µM Y-27632, 30 µM BTS; sterile filtered (0.2 µm)
DNase solution	100 mg DNase II, type V, dissolved in 50 mL 1 x PBS, stored at -20 °C for max. 1 year
EDTA	0.5 mM EDTA in 1 x PBS, sterile filtered and stored at RT or 4 °C
FACS buffer (for cTnT staining)	1 x PBS with 5% FCS, 0.05% Sodium azide and 0.5% Saponin (for intracellular staining)
FACS buffer (for SSEA3 staining)	1 x PBS with 5% FCS
Fibrinogen	200 g/L fibrinogen dissolved in pre-warmed (37 °C) 0.9%-NaCl solution, addition of 33 g/L Aprotinin to a final concentration of 100 µg/mL; stored at -20 °C for short-term and at -80 °C for long-term storage
HEPES stock solution	1 M HEPES dissolved in 1 x PBS, pH adjusted to 7.4 with potassium hydroxide; sterile filtered (0.2 µm filter) and stored at 4 °C for max. 1 year
Kranias buffer	30 mM Tris (pH 8.8), 5 mM EDTA, 30 mM NaF, 3% SDS, 10% Glycerol
Laemmli buffer (1x)	0.2 g SDS, 1 mg Bromphenol blue, 1 g Glycerol, 0.2 mL 0.5 M Tris (pH 6.8), 0.155 g DTT in Aqua dest.
LB medium	10 g Bacto™ Tryptone, 5 g Bacto™ Yeast Extract and 10 g NaCl in 1 L Aqua dest.; pH 7.4, autoclaved
Permeabilisation buffer for immunofluorescence	1 x PBS, 3% milk powder, 0.1% Triton™ X-100
SDS-PAGE electrophoresis buffer (10x)	250 mM Trizma® base, 1.92 M Glycine and 1% or 50% SDS in Aqua dest.
Separating gel SDS-Page	10% acrylamide/bis solution (29:1), 375 mM Tris-base pH 8.8, 0.1% SDS, 0.1% APS, 0.04% TEMED in Aqua dest. up to 10 mL.
SOC medium	20 g Bacto™ Tryptone, 5 g Bacto™ Yeast Extract, 0.5 g NaCl, 400 mL 1 M KCl (pH 7.0), autoclaved; afterwards addition of 1 M MgCl2 (sterile) and 20 mL 1 M Glucose (sterile)
Stacking gel SDS-Page	5.1% acrylamide/bis solution (29:1), 125 mM Tris-base pH 6.8, 0.1% SDS, 0.1% ammonium persulfate (APS), 0.1% tetramethylethylenediamine (TEMED) in Aqua dest. to 10 mL

TAE buffer (50x) for agarose gel electrophoresis	242 g Trizma® base, 37.2 g Titriplex III (EDTA), 57.1 mL concentrated acetic acid in 1 L aqua dest.; pH 8.5, used as 1x diluted in Aqua dest.
TBS (10x)	1 M Trizma® base or Tris-HCl and 1.5 M NaCl in Aqua dest.; pH adjusted to 7.5 with 37% HCl
Thrombin	10 U/mL thrombin dissolved in 60% PBS and 40% sterile water; stored at -20 °C for max. 1 year
Tris 0.5 M (pH 6.8)	60.6 g Trizma® base in 1 L Aqua dest.
Tris 1.5 M (pH 8.8)	181.7 g Trizma® base in 1 L Aqua dest.
Tyrode's solution	120 mM NaCl, 5.4 mM KCl, 1 mM $MgCl_2$ x 6 H_2O, 0.3 - 10 mM $CaCl_2$, 0.4 mM NaH_2PO_4, 22.6 mM $NaHCO_3$, 5 mM Glucose, 0.05 mM Na_2EDTA, and 25 mM HEPES (pH 7.4 in PBS), Aqua ad iniectabilia

10.3.10 Software

Software	**Manufacturer**
CTMV	custom made
FACSDiva	BD Biosciences
Fiji	Image J
Image Lab Version 5.2.1	Bio-Rad Laboratories
Prism 6.0	GraphPad Software
SnapGene® 3.3.4	GSL Biotech LLC
Zen Lite	Zeiss

11 Acknowledgements

In this special part I would like to take opportunity to thank everyone involved in the development of this thesis, without whom this work would not have been realised. I am grateful that the Cardiovascular Research Center (CVRC) supported this thesis. If I could choose again, I would do my dissertation in the same way in the Institute of Experimental Pharmacology and Toxicology and about the same topic.

First of all, I would like to thank Prof. Dr. Lucie Carrier and Prof. Dr. Thomas Eschenhagen for giving me the opportunity to be part of the Institute of Experimental Pharmacology and Toxicology and perform the experiments. It was an honour for me to learn from their experience and huge scientific knowledge, and especially to participate in interesting and fruitful discussions during Monday Morning Meetings in the working group of Prof. Dr. Lucie Carrier. I am pleased that I was part of the team and I enjoyed my time in the laboratory where I learned many new things which I had not done before.

Next, and not less important to me was Dr. Giulia Mearini. She supervised me and taught me all laboratory skills. I especially want to mention her patience with a medical student, who had no experience in laboratory work. In all aspects, she was a helping hand, no matter if there were technical, scientific, experimental or organisational issues. From all persons involved she had the most direct impact on this project.

Furthermore, I would like to pronounce my special thanks to the whole AG Carrier, meaning Dr. Saskia Schlossarek, PD. Dr. Felix Friedrich, Dr. Frederik Flenner, Dr. Maksymilian Prondzynski, Elisabeth Krämer, Antonia Zech, Anna Rinas and Josefine Busch. I would like to outline Elisabeth Krämer for her technical assistance, but also for creating a nice atmosphere. The same was true for Dr. Maksymilian Prondzynski, my seatmate, with his humorous point of view on many things. This was always enlightening. I also thank Annabel Ottenberg for starting this project one year before. I was pleased to take it over from her and proceed in achieving the aim.

Many other people from the institute were involved, for example all people dealing with CRISPR/Cas9, hiPSCs and EHTs, namely Prof. Dr. Arne Hansen, Dr. Bärbel Ulmer, Dr. Christiane Neuber, Dr. Aya Shibamiya, Dr. Mirja Schulze, Dr. Annika Knaust, Thomas Schulze and also Dr. Ingke Braren from the HEXT Vector Facility. Besides, I would like to thank my two external evaluators during this one year medical scholarship of the CVRC program, which were Dr. Justus Stenzig and Prof. Dr. Fehse. They always had supporting ideas to make this project work.

Last, I would especially like to thank Leonard Oelze, Charlotta Behrens and Malte Loos. I enjoyed spending time with them in the laboratory work. They helped me, it was nice to know that I could always rely on them when support was needed.

Finally, I am very happy to have such a great family who always supported me. They participated in mind and their thoughts were with me and my experiments. They stood beside me through this experimental year and the development of this thesis as a major step in my life.

12 Curriculum vitae

„Lebenslauf wurde aus datenschutzrechtlichen Gründen entfernt.“

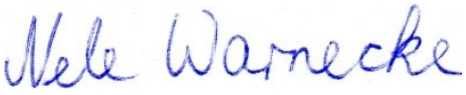

13 Eidesstattliche Versicherung

Ich versichere ausdrücklich, dass ich die Arbeit selbständig und ohne fremde Hilfe verfasst, andere als die von mir angegebenen Quellen und Hilfsmittel nicht benutzt und die aus den benutzten Werken wörtlich oder inhaltlich entnommenen Stellen einzeln nach Ausgabe (Auflage und Jahr des Erscheinens), Band und Seite des benutzten Werkes kenntlich gemacht habe.
Ferner versichere ich, dass ich die Dissertation bisher nicht einem Fachvertreter an einer anderen Hochschule zur Überprüfung vorgelegt oder mich anderweitig um Zulassung zur Promotion beworben habe.
Ich erkläre mich einverstanden, dass meine Dissertation vom Dekanat der Medizinischen Fakultät mit einer gängigen Software zur Erkennung von Plagiaten überprüft werden kann.

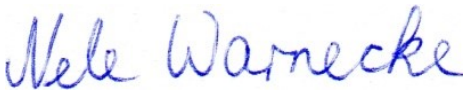

Unterschrift: .....